

Master thesis and internship[BR]- Master's thesis : Development of a methodology for VLEO intake performance testing in a low density facility[BR]- Integration internship

Auteur : Brabants, Coralie

Promoteur(s) : Hillewaert, Koen

Faculté : Faculté des Sciences appliquées

Diplôme : Master en ingénieur civil en aérospatiale, à finalité spécialisée en "aerospace engineering"

Année académique : 2020-2021

URI/URL : <http://hdl.handle.net/2268.2/11557>

Avertissement à l'attention des usagers :

Tous les documents placés en accès ouvert sur le site le site MatheO sont protégés par le droit d'auteur. Conformément aux principes énoncés par la "Budapest Open Access Initiative"(BOAI, 2002), l'utilisateur du site peut lire, télécharger, copier, transmettre, imprimer, chercher ou faire un lien vers le texte intégral de ces documents, les disséquer pour les indexer, s'en servir de données pour un logiciel, ou s'en servir à toute autre fin légale (ou prévue par la réglementation relative au droit d'auteur). Toute utilisation du document à des fins commerciales est strictement interdite.

Par ailleurs, l'utilisateur s'engage à respecter les droits moraux de l'auteur, principalement le droit à l'intégrité de l'oeuvre et le droit de paternité et ce dans toute utilisation que l'utilisateur entreprend. Ainsi, à titre d'exemple, lorsqu'il reproduira un document par extrait ou dans son intégralité, l'utilisateur citera de manière complète les sources telles que mentionnées ci-dessus. Toute utilisation non explicitement autorisée ci-avant (telle que par exemple, la modification du document ou son résumé) nécessite l'autorisation préalable et expresse des auteurs ou de leurs ayants droit.



Development of a methodology for VLEO intake performance testing in a low density facility

Supervisors:

Professor Koen Hillewaert
University of Liège

Professor Thierry Magin
von Karman Institute for Fluid Dynamics

Author:

Coralie Brabants

University of Liège - School of Engineering and Computer Science
Master's thesis carried out to obtain the degree of Master of Science
in Aerospace Engineering
Academic year 2020-2021

Abstract

The Air-Breathing Electric Propulsion (ABEP) is a novel propulsion system composed of a passive intake that collects the atmospheric gas and feeds an electric thruster. This new concept could potentially compensate for the drag force experienced by spacecraft flying in Very Low Earth Orbit (VLEO).

The objective of this thesis is to design a test procedure within a high vacuum installation with the aim of providing the transmissivity to a fast flux of particles. This parameter is of paramount importance to the evaluation of the intake performance.

First, the pressure evolution within the two chambers of the installation is simulated based on a 0-D model implemented in MATLAB. The model is based on kinetic theory and determines an expression for all the flows circulating in the vacuum facility. It allows defining the various factors impacting the facility operation and the relevant intake performance parameters.

Then, a series of tests is proposed. These are required to determine all facility operational parameters which are not measurable directly or within a single test. Two assumptions are considered to determine the intake performance. We will show that one can provide slightly more precise measurements than the other.

Finally, an analysis of the error propagation is realized to estimate the uncertainty of the test results. The large uncertainties associated with some of the tests increase the uncertainty associated to the fast flux transmissivity estimative. This uncertainty depends not only on the analytical reasoning chosen but also on the configuration. The developed 0-D model and uncertainty propagation will be used in the future to assist in the configuration definition of the VKI low density facility. Moreover, the 0-D model will be valuable to retrieve the relevant transmissivities from interpretation of each chamber pressure.

Acknowledgements

I would like to thank Professor Magin and Professor Hillewaert for being available to supervise this work and for giving me the chance to work in the Aeronautics and Aerospace Department at the Von Karman Institute.

I am really grateful to my advisors Damien Le Quang, Pietro Parodi and Pedro Jorge for all the precious time they spent guiding and reviewing my work.

I would like to thank all my family, in particular my parents and my grandparents, who were real support during this internship but also during all my studies.

Contents

List of Figures	v
List of Tables	vii
List of Symbols	viii
1 Introduction	1
1.1 Motivation and RAM-EP concept	1
1.1.1 Motivation	1
1.1.2 RAM-EP concept	2
1.2 VKI facility	2
1.3 Objectives	3
1.4 Outline	3
2 Physical models for rarefied gases	5
2.1 Dilute gas	5
2.2 Molecular models	7
2.3 Kinetic theory	8
2.3.1 The distribution function	8
2.3.2 The Boltzmann equation	10
2.3.3 The Equilibrium state	11
2.4 Conclusion	13
3 VKI vacuum facility	14
3.1 Contamination	14
3.1.1 Desorption	14
3.1.2 Diffusion with desorption	15
3.1.3 Permeation and leaks	15
3.1.4 Impact on the pressure	15
3.2 Pumping system	16
3.2.1 Types of vacuum	17
3.2.2 Rotary vane pump	17
3.2.3 Turbomolecular pump	18
3.3 Particle flow generator	20
3.4 Conclusion	21
4 Development of the 0-D model	22
4.1 Transmission probabilities of ducts	22
4.2 Analytical model	23

4.2.1	Description of the model	23
4.2.2	Ion fraction reaching the duct inlet	27
4.3	Verification of the model	32
4.3.1	Steady-state verification	34
4.3.2	Temporal verification	38
4.4	Conclusion	40
5	Test scenarios	42
5.1	Measurable parameters and probes	42
5.2	Measurement procedure	46
5.2.1	Main chamber leak flux	46
5.2.2	Secondary chamber leak flux	49
5.2.3	First turbopump pumping speed	51
5.2.4	Second turbopump pumping speed	53
5.2.5	Charge exchange ions impact	55
5.2.6	Slow flux transmission probabilities	57
5.2.7	Fast flux transmission probability	60
5.3	Conclusion	62
6	Error propagation analysis	64
6.1	Error analysis theory	64
6.1.1	Statistics reminder	64
6.1.2	Error propagation theory	65
6.2	Error propagation analysis	66
6.2.1	Measurement uncertainties	67
6.2.2	Leak flux uncertainties	67
6.2.3	First pump pumping speed	69
6.2.4	Second pump pumping speed	69
6.2.5	Slow flux transmissivities	70
6.2.6	Fast flux transmissivity	71
6.3	Conclusion	72
7	Conclusion	74
7.1	Future work	75
A	Expression Analytic used for the slow flux transmissivities	78
A.1	Case 1: $\bar{A}_{intake} \geq A_1$	80
A.2	Case 2: $A_1 > \bar{A}_{intake} \geq A_2$	81
A.3	Case 3: $\bar{A}_{intake} < A_2$	82
B	Partial derivatives of the Error Propagation Analysis	83
B.1	Slow flux transmission probabilities	83
B.1.1	First hypothesis	83
B.1.2	Second hypothesis hypothesis	83
B.2	Fast flux transmission probability	84

List of Figures

1.1	The RAM-EP system concept by SITAEI, Italy	2
1.2	VKI facility is composed of two vacuum chambers and two turbopumps. The PFG is placed in the main chamber and an ABEP system is comprised in a duct linking both chambers.	3
2.1	Collision in the Hard-Sphere model	6
2.2	Electrostatic interaction force between molecules as a function of the distance between them	6
2.3	Limits of the different mathematical models from [3]	8
2.4	Volume containing the molecules that will cross dA in the time interval dt	10
2.5	Normalized distribution function of the absolute values of particle velocity \mathbf{c} for the Maxwell-Boltzmann equilibrium distribution function.	12
3.1	Pressure evolution of an isolated vacuum chamber exposed to different contamination rate from [10]	16
3.2	Representation of flow range dependant on pressure and characteristic length scale.	17
3.3	Operating principle of a rotary vane pump.	18
3.4	Principle of the molecular pump	19
3.5	Schematic of a turbomolecular pump	19
3.6	Pumping speed S as a function of the relative molecular mass M_r	20
3.7	Pumping speed as a function of the pressure for various gases.	20
3.8	Principle of a gridded ion thruster from [23]	21
4.1	Representation of the fluxes defining the duct transmission probability.	22
4.2	Representation of the VKI's facility variable used in the model	23
4.4	Scheme of an infinitesimal surface dA_i emitting a radiation towards the infinitesimal surface dA_j at a distance r	28
4.5	Scheme of the infinitesimal PFG surface dA_i emitting a radiation towards the infinitesimal duct entrance surface dA_j at a distance r	29
4.6	Profile view of the duct entrance.	30
4.7	Evolution of the ion fraction in function of PFG-valve distance	31
4.8	Evolution of the Relative difference between the View factor method and TPMC method in function of the PFG-valve distance	33
4.9	Comparison of the pressure evolution between the theory and the model with an initial pressure of 0.1 mbar	40
4.10	Comparison of the pressure evolution between the theory and the model with an initial pressure of 0.01 mbar	40

5.1	Diagram representing a Faraday probe. A collecting conducting surface surrounded by a guard ring is attached on a ceramic insulator which prevents ions going in the opposite direction from touching the probe (from [9])	45
5.2	Schematic of an RPA probe. Four grids are arranged in front of a collector plate. The four grids are biased to different potentials in order to repel electrons and filter incoming ions from the gas plume. .	46
5.3	Pressures evolution in both chamber during the first test	48
5.4	Pressures evolution in both chamber during the second test	50
5.5	Pressures evolution in both chamber during the third test	52
5.6	First part of the pressures evolution in both chamber during the fourth test	54
5.7	Second part of pressures evolution in both chamber during the fourth test	54
5.8	Pressures evolution in both chamber during the Faraday Probe Calibration	56
5.9	Pressures evolution in both chamber during the sixth test	58
5.10	Pressures evolution in both chamber during the seventh test	61
6.1	A visual representation of the Empirical (68-95-99.7) Rule based on the normal distribution (from [16])	65
A.1	Analytical model used to model the connection between both chambers	79

List of Tables

3.1	Overview of types of flow regimes.	17
4.1	Nominal conditions imposed during the code verification	33
4.2	Flux parameters used during the code verification	34
5.1	Pressures and times of the intermediate situations of the first test . .	48
5.2	Pressures and times of the intermediate situations of the second test .	50
5.3	Pressures and times of the intermediate situations of the third test . .	51
5.4	Pressures and times of the intermediate situations of the second test .	55
5.5	Pressures and times of the intermediate situations of the Faraday Probe Calibration	57
5.6	Pressures and times of the intermediate situations of the sixth test . .	58
5.7	Pressures and times of the intermediate situations of the seventh test	61
5.8	Values and relative difference of the results provided by the tests . . .	63
6.1	Uncertainty(95% confidence interval) and standard deviation of all Measurement probe used during test procedure	67
6.2	Values and standard deviations of the results provided by the tests .	73

List of Symbols

Acronyms

ABEP	Air-Breathing Electric Propulsion
CEX	Charge EXchange
ESA	European Space Agency
GOCE	Gravity field and steady-state Ocean Circulation Explorer
HS	Hard-Sphere
LEO	Low Earth Orbit
NS	Navier-Stokes
PFG	Particle Flow Generator
RAM-EP	RAM-Electric Propulsion
RPA	Retarding Potential Analyzer
RTD	Resistance Thermometer Detector
TPMC	Test Particle Monte Carlo Method
VKI	Von Karman Institute
VLEO	Very Low Earth Orbit

Roman symbols

a	accommodation coefficient	[-]
A	area	[m ²]
\mathbf{c} or \mathbf{v}	velocity vector	[m/s]
c_{mp}	most probable speed	[m/s]
c_q	root mean square speed	[m/s]
d	particle diameter in Hard Sphere model	[m]
d_{PFG}	PFG-duct distance	[m]
f	velocity distribution function	[s ³ .m ⁻⁶]
f_{ion}	ion proportion reaching the duct inlet	[-]
F_{ij}	view factor	[-]
k	Boltzmann's constant	[J/K]
Kn	Knudsen number	[-]
L	characteristic length	[m]
m	mass	[kg]
n	number density	[m ⁻³]
\dot{N}	particle flow per unit time	[particle/s]
N_a	Avogadro number	[particle/mol]
p	pressure	[Pa]
P	pressure	[mbar]
P_u	ultimate pressure	[mbar]
Q	gas flow	[mbar/L.s]
\mathbf{r}	position vector	[m]
R	universal ideal gas constant	[J/(mol.K)]
S	pumping speed	[L/s]
S_p	speed ratio	[-]
$SCCM$	PFG flux	[SCCM]
t	time	[s]
T	Temperature	[K]
V	Volume	[m ³]

Greeks symbols

δ	mean molecular spacing	[m]
η_m	mass utilization	[-]
λ	mean free path	[m]
ξ	Slow flux divided by the pressure	[L/s]
ρ_0	standard condition density	[kg/m ³]
σ	standard deviation	[-]
Φ	flux (per unit area)	[m ⁻² .s ⁻¹]
τ	transmission probability	[-]

Sub- and Superscripts

<i>c1</i>	value relative to the main chamber
<i>c2</i>	value relative to the secondary chamber
<i>i</i>	value relative to the chamber $i = 1$ or 2
<i>des</i>	value relative to the desorption phenomenon
<i>diff</i>	value relative to the diffusion phenomenon
<i>perm</i>	value relative to the permeation phenomenon
<i>leak</i>	value relative to the leak phenomena
<i>1, fast</i>	value relative to the fast flux
<i>1, slow</i>	value relative to the slow flux going to the secondary chamber
<i>2, slow</i>	value relative to the fast flux going to the main chamber
<i>PFG</i>	value relative to the fast flux going to the PFG
<i>w1</i>	value relative to the main chamber wall
<i>w2</i>	value relative to the secondary chamber wall
<i>n</i>	standard condition
<i>P</i>	value relative to the turbopump

Chapter 1

Introduction

Today, many observation and telecommunication satellites are placed in Low Earth Orbit (LEO). This type of orbit is generally located between 300 and 2000 km altitude. However, some missions requiring very high precision measurements must place their satellites at lower altitudes. It is the case of the “Gravity field and steady-state Ocean Circulation Explorer” (GOCE) spacecraft launched in 2009 by the European Space Agency (ESA). The objective of this mission was to collect data from the gravitational fields of the Earth and the upper layer of the atmosphere with significantly higher accuracy with respect to its predecessors. Consequently, the satellite orbited at an average altitude of 250 km and could descend at 224 km altitude. Orbits with an altitude below 300 km are defined as Very Low Earth Orbits (VLEO).

1.1 Motivation and RAM-EP concept

1.1.1 Motivation

As proved by the GOCE mission, there are many advantages to operating in VLEO. As exposed in [1], some of these advantages are:

- The optical equipment of the satellite obtains better ground resolution.
- The radiometric performances are also improved.
- The satellite needs less propellant to reach its orbit.
- No end-of-life maneuver is required.
- There is less risk of collision with space debris.

However, the satellites are more exposed to atmospheric drag and must compensate for it using propulsion. In the case of the GOCE mission, its lifespan was limited by the quantity of propellant (xenon) on board. Therefore, this mission had a short lifespan (two years) compared to other missions with more conventional orbits. Recently, a concept called RAM-Electric Propulsion (RAM-EP) or Air-Breathing Electric Propulsion (ABEP) has emerged in an attempt to solve this problem. This means of propulsion generates thrust by collecting atmospheric particles as propellant.

1.1.2 RAM-EP concept

ABEP systems development is, currently, a topic of intensive research. ESA's RAM-EP, designed and developed by SITAEL in Italy, was first tested in a laboratory in May 2017.

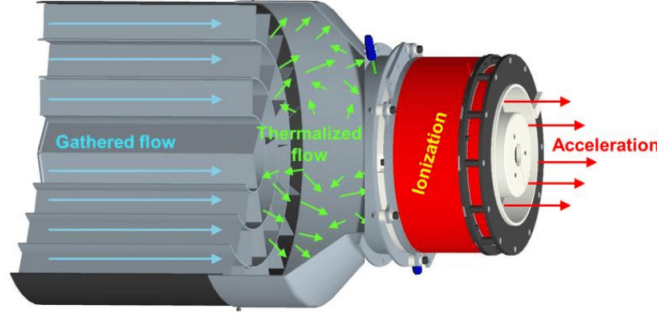


Figure 1.1: The RAM-EP system concept by SITAEL, Italy

As depicted in Figure 1.1, the system consists of three parts (see [18] and [2]). First, a passive air inlet collects atmospheric gas. Next, it is thermalized by the collector. Finally, the gas enters in a two-stage Hall effect thruster. The first stage is the ionization stage and allows the gas particles to be ionized. The second stage is the particle acceleration stage that provides thrust to the spacecraft. An ABEP could potentially extend the lifetime of satellites in LEO and VLEO up to 10 years or theoretically even more. The optimal altitude for an Earth-orbiting ABEP is between 120 - 250 km.

1.2 VKI facility

A facility will be built at Von Karman Institute (VKI) for the ground testing of RAM-EP systems. Its purpose is to determine the intake performance of such systems. The tests carried out within this installation must meet three conditions.

First, the pressure in the installation containing the intake must be very low. This condition aims to obtain a medium resembling the atmospheric medium as much as possible. To decrease the pressure inside a chamber, the installation vacuum chambers are connected to a particular pumping system. It allows it to reach pressures of the order of 10^{-8} mbar.

Then, a flow similar to the atmospheric flow must be able to reach the intake. Atmospheric flow is not simple gas and is different for different orbital altitudes. It is a very fast ionized gas or plasma, composed of neutral particles and a small fraction of charged particles (ions and electrons). To replicate such flow on ground, it is required to use a Particle Flow Generator (PFG).

Finally, the flow characteristics of each intake side must be measured independently. The intake is therefore placed at the level of a duct connecting two vacuum chambers.

The VKI installation is represented in Figure 1.2. Its structure makes it possible to respect the three conditions mentioned above. It comprises two vacuum chambers, each associated with a pumping system. The PFG is located in the main chamber. It is aligned with the chamber connection and sends a particle flow directed towards the intake entrance.

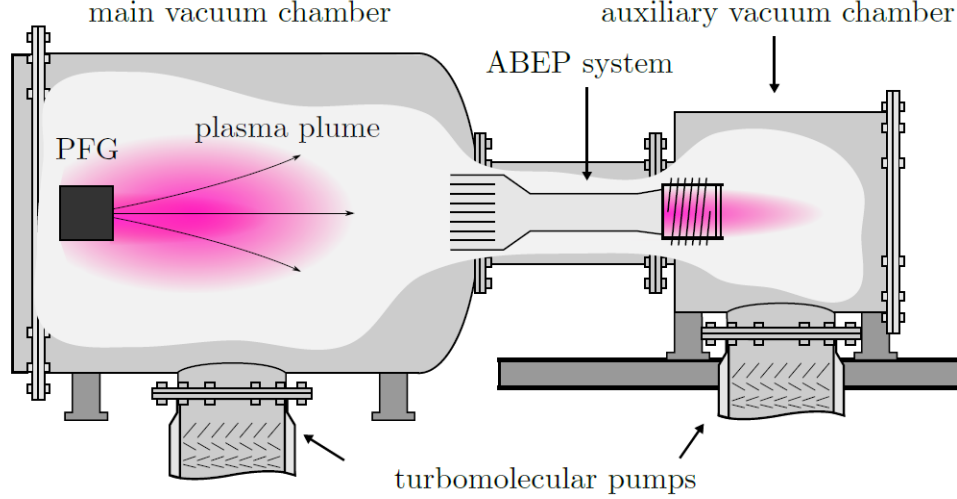


Figure 1.2: VKI facility is composed of two vacuum chambers and two turbopumps. The PFG is placed in the main chamber and an ABEP system is comprised in a duct linking both chambers.

The different installation systems are dealt with in more depth in Chapter 3.

1.3 Objectives

By considering the configuration described previously, the objective of this study is to determine if it is possible to devise a series of tests to determine the performance of the intake placed between the two chambers. The investigation analyzes first the evolution of each chamber pressure through a simple 0-D model. The relevant parameters that influence the facility operation are established and estimates of the steady-state pressure for a given configuration are computed. A series of tests is then proposed to estimate the parameters characterizing the intake. Finally, an error propagation analysis analyzes the accuracy of the results based on the measurements realized in the installation.

1.4 Outline

The thesis is structured as follows:

- Chapter 2 introduces the fundamental concepts of rarefied gases. These concepts will be used for the model development of Chapter 4.
- Chapter 3 describes in detail the theory of vacuum facilities and some of their equipment namely the pumping system and the Particle Flow Generator (PFG).
- In Chapter 4, the installation is analyzed by a 0-D model. Within this model the transmission probability of the intake is defined.
- Chapter 5 presents a series of tests that can be carried out within the installation to determine the value of this transmission probability.

- Chapter 6 performs an error propagation analysis. This study studies the level of reliability of the tests carried out as well as the results obtained.
- Finally, Chapter 7 concludes the thesis work and proposes some possible future developments.

Chapter 2

Physical models for rarefied gases

This chapter provides the fundamental theory required to define a rarefied gas. Some expression based on the Boltzmann equation are derived in this chapter. They will be used for the installation model.

2.1 Dilute gas

Depending on the scale used, a gas can be represented in two ways. On a macroscopic scale, a gas is a continuous medium. It is defined by a set of macroscopic properties, such as pressure, temperature, speed, etc. On a microscopic scale, a gas corresponds to a large number of small molecules or particles. Each is characterized by a position, a velocity, a size, a mass, and an internal state. For simplicity reasons, the discussion in this section studies a gas composed of a single chemical species. The particles are therefore identical.

The number density n is the number of molecules in a given volume of gas divided by that volume. It allows to determine the average volume available per molecule, $\frac{1}{n}$, and the mean molecular spacing

$$\delta = n^{-\frac{1}{3}}. \quad (2.1)$$

A simplified model analyzing the particle collision is the Hard-Sphere (HS) model. This model considers that each particle corresponds to a hard-sphere of diameter d . When at least two of these spheres approach at a distance equal to d , they collide. Collisions are considered purely elastic.

Although this model is a little too simplistic to explain the interactions between particles, it allows obtaining a simple expression of a useful parameter for the study of rarefied gas. The mean distance traveled by molecules between two collisions, also called the mean free path λ . It is possible to show that the mean free path for a simple gas at equilibrium is

$$\lambda = \frac{1}{\sqrt{2}n\pi d^2}.$$

In reality, each molecule includes electrons and nuclei. These charged components are the interaction force sources between particles. So even if the molecules do not touch each other, they can be influenced by one another. To take this aspect into account, a more realistic interaction potential like the Lennard-Jones potential is needed. According to this model, the interaction force between particles is

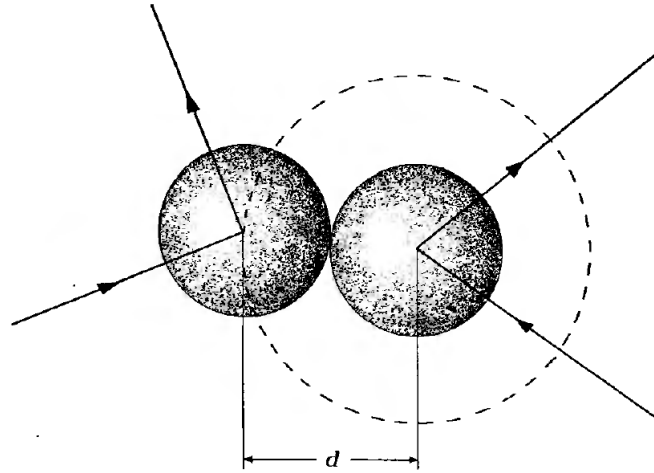


Figure 2.1: Collision in the Hard-Sphere model

isotropic and depends only on the distance between them. Its amplitude is represented by Figure 2.2. It appears that this force tends towards zero when the inter-particle distance tends towards infinity. As the particles get closer, it becomes slightly attractive. But when the particles get too close, the force suddenly becomes repulsive.

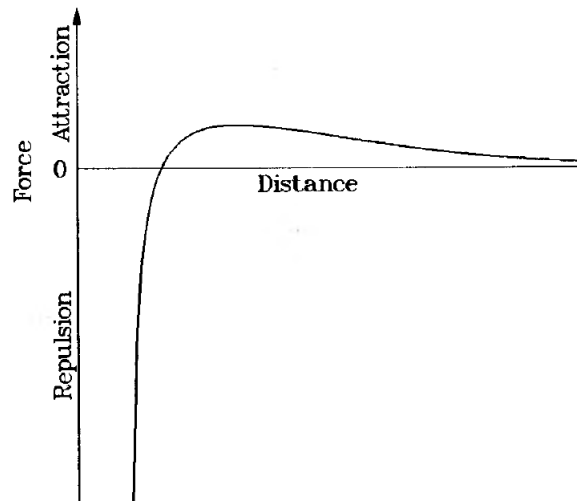


Figure 2.2: Electrostatic interaction force between molecules as a function of the distance between them

Thanks to all these aspects, it is now possible to define a dilute gas. Equation 2.1 shows that the lower the density, the larger the space between molecules. The proportion of the gas volume actually containing a particle is of the order of $\left(\frac{d}{\delta}\right)^3$. For the same type of particle (same diameter d), the lower the density, the lower this volume proportion. Thus, when the density is very low, the volume proportion occupied by a particle is also small and implies

$$\delta \gg d.$$

This condition defines a criteria to considering a gas dilute. The inter-particle distance is so large compared to their dimension that each particle is beyond the

reach of the influence of others. When a collision occurs, it is almost always binary. Interactions involving more than two particles are highly unlikely in this situation.

2.2 Molecular models

Two different gas descriptions were given in the previous Section. Depending on the chosen representation, the different models are applied. When the gas is a continuum medium (macroscopic scale), it follows the Navier Stokes(NS) equations. When the gas is a particle set (microscopic point of view), the mathematical model is based on the Boltzmann equation. These two models are complementary because the NS equations are simpler but not always applicable. The properties used at the macroscopic scale (pressure, temperature, etc.) are comparable to the average values of the particle quantities. As long as the number of particles per unit volume is sufficient, collisions are very numerous, and the mean free path is very low. The molecules almost constantly exchange their energy with each other and guarantee uniform properties within the gas. When the density decreases strongly, these collisions become very rare, and the mean free path increases. The properties are no longer uniform. When their gradients are of the same order of magnitude as the mean free path, the equations of NS are no longer applicable.

To express this more precisely, the Knudsen number Kn is introduced. This parameter corresponds to the degree of rarefaction of the gas and is given by

$$Kn = \frac{\lambda}{L}, \quad (2.2)$$

with L the scale length of the macroscopic gradients. When $Kn > 0.1$, the error in NS results becomes significant.

Another limit can be defined. The macroscopic properties of the continuous model are associated with a “point”. This “point” corresponds to a set of N particles contained in an elementary volume V which includes the “point”. The particle number in each volume varies around an average value nV . It is possible to prove that the standard deviation of the fluctuation is given by $\frac{1}{\sqrt{nV}}$ (see [3]). Thanks to relation 2.1, this deviation can be written $\frac{1}{\sqrt{V/\delta^3}}$ with δ the average distance between the particles. So the fluctuations are negligible and the macroscopic quantities have a meaning, if

$$V^{\frac{1}{3}} \gg \delta, \quad (2.3)$$

with $V^{1/3}$ the typical dimension of an elementary volume. The macroscopic properties are based on the molecules of the element. They depend on the elementary volume size. For a three-dimensional system, $V^{1/3}$ is less than L . And the condition 2.3 is equivalent saying that the statistical fluctuations are negligible, if $L \gg \delta$.

All the concepts seen previously are summarized on the graph 2.3. This graph shows clearly the limits of validity of the approximation of the dilute gas and the different gas modelling approaches. The gas density is normalized by the standard condition density ρ_0 .

The diluted gas assumption requires that $\frac{\delta}{d} \ll 1$, the author of the document [3] selected the limit $\frac{\delta}{d} = 7$. This line is purely vertical because δ and d are independent of L . The continuous model is considered valid as long as the Navier Stokes equations are applicable. When $Kn = 0.1$, the molecular model substitutes

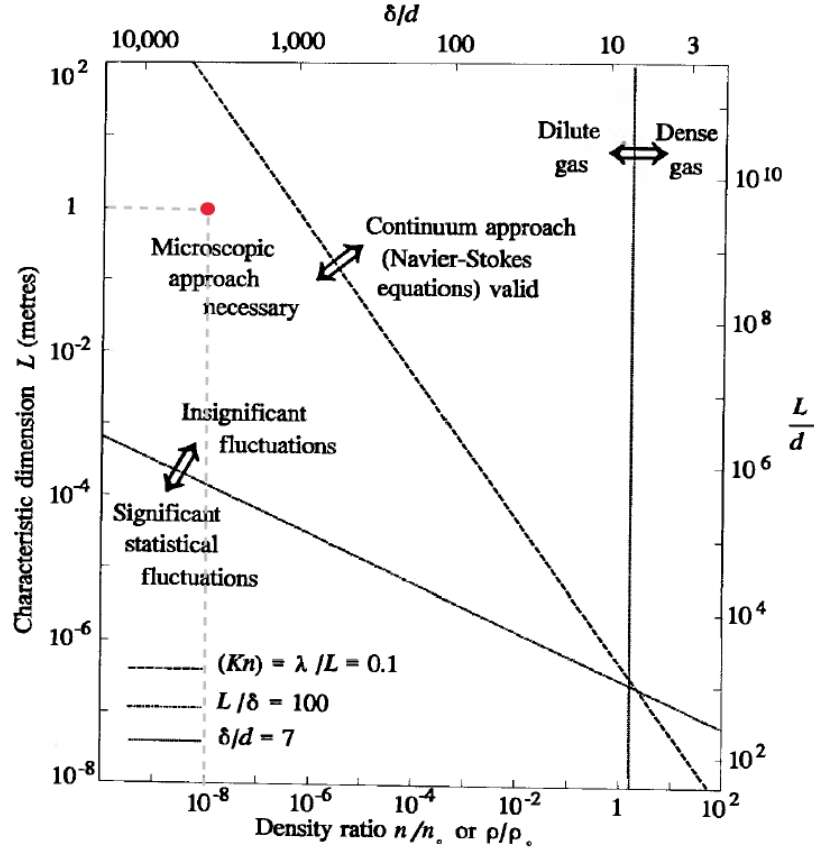


Figure 2.3: Limits of the different mathematical models from [3]

for the continuous model. Finally, the macroscopic properties are subject to statistical fluctuations. These become consequent when $\frac{L}{\delta} \leq 100$. This criterion states that for the fluctuations to be negligible, L must be greater than the dimension of ten elementary volumes, each possessing 1000 molecules.

In the case of the VKI installation, the nominal pressure is approximately 10^{-5} mbar, and the characteristic length scale L is 1 m. The red point on the graph represents these conditions. It shows that the microscopic approach must be used, but the statistical variations being negligible. The medium can be defined by a series of macroscopic variables.

2.3 Kinetic theory

The molecular model describes a diluted gas by using kinetic theory. This theory characterizes each particle by a position, a velocity, and an internal state. A gas is fully defined, only when all the particle parameters for each time step are known. The number of particle in a real gas is so large that this approach is impossible to implement. Instead, probability distributions are used.

2.3.1 The distribution function

The macroscopic flow properties depend on the characteristics of the particles. A typical molecule has a position $\mathbf{r} = (x, y, z)$ and a velocity $\mathbf{c} = (u, v, w)$. The x , y , and z components define a physical space. An elementary volume is given by the

product $dx dy dz$ written $d^3\mathbf{r}$. A particle belongs to such a volume, if its position components are between $[x; x + dx]$, $[y; y + dy]$ and $[z; z + dz]$.

Likewise, u , v , and w define a velocity space. In this space, a particle can also be represented by a point. Its location depends on the value of its velocity vector. An elementary volume in this coordinate system is given by $du dv dw$, also written $d^3\mathbf{c}$. A particle belonging to this volume has velocity components in the intervals $[u; u + du]$, $[v; v + dv]$ and $[w; w + dw]$.

These two spaces can be combined to form the six-dimensional phase space. An elementary volume in this space is $d^3\mathbf{r}d^3\mathbf{c}$. Knowing this, the velocity distribution function in phase space $f(\mathbf{r}, \mathbf{c}, t)$ is given by

$$dN(\mathbf{r}, \mathbf{c}, t) = f(\mathbf{r}, \mathbf{c}, t)d^3\mathbf{r}d^3\mathbf{c}, \quad (2.4)$$

with dN the particle number in the elementary space $d^3\mathbf{r}d^3\mathbf{c} = dx dy dz \times du dv dw$ in the neighbourhood of the position \mathbf{r} , with velocity around \mathbf{c} . The particles therefore have position components included in $[x; x + dx]$, $[y; y + dy]$ and $[z; z + dz]$ and speed components in $[u; u + du]$, $[v; v + dv]$ and $[w; w + dw]$.

Given the definition of the distribution function, it is possible to calculate the macroscopic properties by integrating over the velocity coordinates. The first of these is the number density $n(\mathbf{r}, t)$. In the phase space, it corresponds to the number of particle in the elementary volume $d\mathbf{r}$ at the instant t . It is independent of the velocity. It is related to the distribution function by the relation

$$n(\mathbf{r}, t) = \int_{-\infty}^{\infty} \int_{-\infty}^{\infty} \int_{-\infty}^{\infty} f(\mathbf{r}, \mathbf{c}, t)d^3\mathbf{c}. \quad (2.5)$$

As the macroscopic quantities $\langle \Omega \rangle$ corresponds to the average value of the molecular properties. They are linked to the molecular quantity Ω by

$$\langle \Omega(\mathbf{r}, t) \rangle = \frac{\int_{-\infty}^{\infty} \int_{-\infty}^{\infty} \int_{-\infty}^{\infty} \Omega f(\mathbf{r}, \mathbf{c}, t)d^3\mathbf{c}}{\int_{-\infty}^{\infty} \int_{-\infty}^{\infty} \int_{-\infty}^{\infty} f(\mathbf{r}, \mathbf{c}, t)d^3\mathbf{c}}.$$

As the denominator corresponds to the number density, a more convenient expression relating the macroscopic property to the distribution function is

$$\langle \Omega(\mathbf{r}, t) \rangle = \frac{1}{n(\mathbf{r}, t)} \int_{-\infty}^{\infty} \Omega f(\mathbf{r}, \mathbf{c}, t)d^3\mathbf{c}.$$

The distribution function can also be used to calculate the flux of a macroscopic property $\langle \Omega \rangle$. Considering a surface dA immersed in a gas. A particle with a velocity between \mathbf{c} and $\mathbf{c} + d\mathbf{c}$ crosses this surface between t and $t + dt$, if and only if its initial position belongs to the volume adjacent to dA of length $\mathbf{c}dt$. The volume shown on Fig. 2.4 is given by

$$d\mathbf{r} = \mathbf{c} \cdot \mathbf{n} dA dt,$$

with \mathbf{n} is the unit vector normal of dA .

The particle number with a velocity between \mathbf{c} and $\mathbf{c} + d\mathbf{c}$ in this volume is therefore

$$f d\mathbf{r} d\mathbf{c} = f \mathbf{c} \cdot \mathbf{n} dA dt d^3\mathbf{c}. \quad (2.6)$$

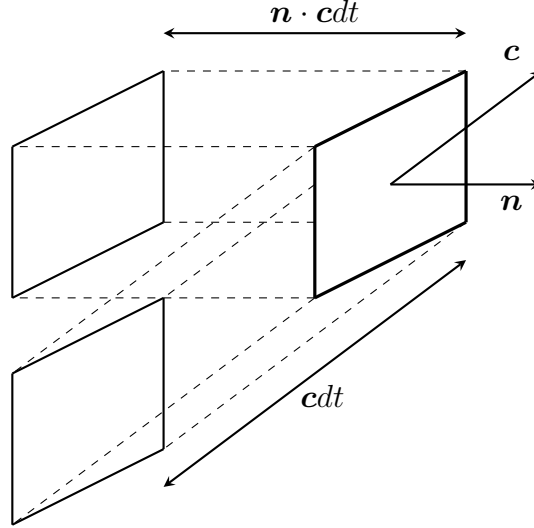


Figure 2.4: Volume containing the molecules that will cross dA in the time interval dt

The total flux Φ of the property Ω crossing the surface dA is given by the integral of this number over all the velocity directions and multiplied by Ω . This flow represents the quantity of the property Ω transported per unit of time and per unit of area. The flux is given by

$$\Phi(\Omega) = \int_{\mathbf{c} \cdot \mathbf{n} > 0} \Omega f \mathbf{c} \cdot \mathbf{n} d^3 \mathbf{c}. \quad (2.7)$$

Only the particles for which respect $\mathbf{c} \cdot \mathbf{n} > 0$ are considered. Otherwise the particle was not initially in the volume and crossed the surface to enter it.

2.3.2 The Boltzmann equation

The time evolution of the distribution function f follows Boltzmann's equation

$$\frac{\partial f}{\partial t} + \mathbf{c} \cdot \nabla_r f + \frac{\mathbf{F}}{m} \cdot \nabla_c f = \left. \frac{\partial f}{\partial t} \right|_{coll},$$

where m is the particle mass, \mathbf{F} is the external force acting on particle, ∇_r is the traditional nabla operator and ∇_c is the nabla operator in the velocity space

$$\nabla_c = \left(\hat{x} \frac{\partial}{\partial u} + \hat{y} \frac{\partial}{\partial v} + \hat{z} \frac{\partial}{\partial w} \right).$$

It has the form of a continuity equation, and considers the effect of three phenomena:

- The scattering of molecules into and out of $d^3 \mathbf{r} d^3 \mathbf{c}$ is taken into account by the term $\frac{\partial f}{\partial t}$.
- The molecule convection across the face dA which corresponds to the term $\mathbf{c} \cdot \nabla_r f$.
- The convection of molecules caused by external force represented by $\frac{\mathbf{F}}{m} \cdot \nabla_c f$.

The term $\left. \frac{\partial f}{\partial t} \right|_{coll}$ is the collision term. As the gas is assumed rarefied, only binary collisions are considered.

2.3.3 The Equilibrium state

At the equilibrium state, molecule interactions do not affect the distribution function over time, and there is no spatial gradient in the number density. Therefore, the equilibrium distribution function is the stationary Boltzmann's equation solution when no external force acts on the system. If no external forces are present, the force term is canceled ($\mathbf{F} = 0$). As the particles are uniformly distributed in space, the spatial derivative of the distribution function cancels ($\nabla_r f = 0$). Finally, the solution does not depend on time ($\frac{\partial f}{\partial t} = 0$). The Boltzmann's equation for the equilibrium state is therefore

$$\left. \frac{\partial f}{\partial t} \right|_{coll} = 0. \quad (2.8)$$

Many authors have proved that the Maxwell-Boltzmann velocity distribution satisfies the equation 2.8 (in [20]). The particle distribution function of the gas at equilibrium is

$$f(\mathbf{c}) = n \left(\frac{m}{2\pi kT} \right)^{\frac{3}{2}} \exp \left(-\frac{m|\mathbf{c} - \mathbf{v}|^2}{2kT} \right), \quad (2.9)$$

where k is the Boltzmann constant, \mathbf{v} is the bulk velocity of the gas and T the kinetic temperature. This latter is the temperature linked to the average kinetic energy by the relation

$$\frac{3}{2}nkT = \frac{1}{2}nm\langle c \rangle^2 = \frac{1}{2}m \int_{-\infty}^{\infty} F c^2 d\mathbf{c}, \quad (2.10)$$

Where $c = |\mathbf{c}|$ is the norm of the velocity vector.

Equations 2.9 and 2.10 allow defining the speed distribution function $F(c)$. Considering the bulk speed null and integrating 2.9 in all directions for the speed \mathbf{c} , the speed distribution function corresponds to

$$F(c) = 4\pi n \left(\frac{m}{2\pi kT} \right)^{\frac{3}{2}} c^2 \exp \left(-\frac{mc^2}{kT} \right).$$

Figure 2.5 represents the evolution of this function as a function of the norm of the velocity vector c .

As shown by Figure 2.5, this function makes it possible to distinguish three particular speeds namely: the most probable speed c_{mp} , the average speed $\langle c \rangle$, and the root mean square speed c_q . They are given by

$$c_{mp} = \sqrt{\frac{2kT}{m}}, \quad (2.11)$$

$$\langle c \rangle = \sqrt{\frac{8kT}{\pi m}}, \quad (2.12)$$

$$c_q = \sqrt{\langle c \rangle^2} = \sqrt{\frac{3kT}{m}}. \quad (2.13)$$

These speeds are used to determine the expression of the particle flow through an immersed surface in gas at equilibrium. With relation 2.7 and knowing that $\Omega = 1$, the flux is equal to

$$\Phi = \int_{w=-\infty}^{\infty} \int_{v=-\infty}^{\infty} \int_{u=0}^{\infty} f(u, v, w) u \, du \, dv \, dw, \quad (2.14)$$

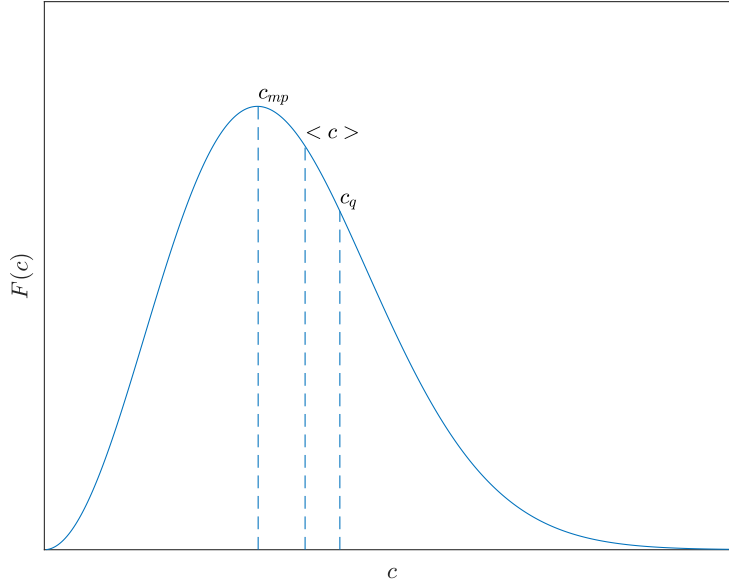


Figure 2.5: Normalized distribution function of the absolute values of particle velocity \mathbf{c} for the Maxwell-Boltzmann equilibrium distribution function.

where u is the gas speed component in the direction normal to the surface such that $\mathbf{c} \cdot \mathbf{n} = u$. As for the expression 2.7, only particles crossing the surface in the right direction are considered. The component u is either zero or positive.

The integration of 2.14 provides the expression

$$\Phi = \frac{1}{4}n\sqrt{\frac{8kT}{\pi m}} \left[e^{-S_p^2} + \sqrt{\pi}S_p(1 + S_p) \right],$$

with $S_p = \frac{u}{c_{mp}}$ the speed ratio of the gas in the direction normal to the surface.

Two extreme cases can be identified. When $S_p \rightarrow 0$, the gas has no bulk velocity component in the x-direction. The flow through the surface is only caused by the thermal movement of the particles. The thermal flux is equal to

$$\Phi = \frac{1}{4}n\sqrt{\frac{8kT}{\pi m}} = \frac{1}{4}n\langle c \rangle. \quad (2.15)$$

When $S_p \gg 1$, the random movement of particles is negligible compared to bulk speed. The gas velocity vector is nearly perpendicular to the surface. Moreover the speed ratio is linked to the Mach number Ma (see [11]) by

$$S_p = \sqrt{\frac{\gamma}{2}}\text{Ma},$$

where γ is the ratio of specific heats of the gas. Therefore the flow of this case is supersonic. Its value is determined by

$$\Phi = nu. \quad (2.16)$$

2.4 Conclusion

This section covers an overview of the diluted gas theory. First, parameters such as the mean free path λ , the Knudsen number Kn , and the average distance between the particles δ are introduced. They define criteria to consider a gas dilute and select the appropriate mathematical model for the installation. Then, based on the kinetic theory, some expressions essential to the 0-D model detailed in Chapter 4 are obtained. These are the average speed, thermal flux, and speed ratio.

Chapter 3

VKI vacuum facility

This chapter introduces the basic concepts for understanding the operation of the VKI installation and each of its components. These are based on the theory discussed in Chapter 2 and will be used to model the installation. The first section explains how molecules from the external environment or the facility itself can enter the vacuum medium and the consequences of such phenomena. The second part deals with the facility pumping system. Finally, the particle flow generator is discussed in more depth.

3.1 Contamination

In reality, creating a “vacuum” is a lengthy procedure. The time required to reach a certain pressure depends on the pumps used and the vessel’s properties. Some unwanted materials or substances enter the installation and degrade its operation. These components not only prevent the desired ultimate pressure to be reached, but also damage the facility. This phenomenon is called contamination. Typical sources of contamination are:

- residues of the vacuum system such as oil and grease on the surface, screws, and seals.
- particles generated by the experiments carried out in the chambers,
- contaminants from ambient air.

Among all the molecules present in the ambient air, water is one of the most contaminating components. Normal ambient air contains approximately 10 g of water vapor per m³. Condensed water vapor is therefore found on the entire surface of the installation. In addition, water molecules are polar, which facilitates their adsorption. As the installation must be as “clean” as possible, all of its components must be dry and grease-free. In addition to the adsorption of water, other components and other phenomena can contaminate the interior of the chamber.

3.1.1 Desorption

Before the pump-down operation begins, the pressure inside the chamber is equal to the ambient atmospheric pressure. The gas molecules contained in the vessel can

adhere to the internal surface. They can be absorbed by the surface, i.e. enter the wall depending on its permeability. But they can also be adsorbed. That means that they are simply fixed to the surface without migrating towards the interior of it. When the chamber is emptied using a pump, these particles bound to the walls are desorbed under the vacuum effect. As the number of particles at the surface decreases, the desorption rate Q_{des} from metal surfaces decreases over time. In general, this reduction is assumed proportional to the time during some duration. But as the installation runs and vacuum is present for a sufficient period, this rate becomes negligible and can be considered null.

3.1.2 Diffusion with desorption

When the installation includes polymer components (as seals), these can also impact the vessel medium even if they are not directly in contact with the interior of the chamber. Their impact can become significant when the pressure drops below 10^{-6} mbar. As explained in [19], polymers can dissolve and store gases depending on their permeability. As with the particles coming from the chamber surface, the gas molecules stored in the polymer seals desorb and diffuse through the facility walls. Although the plastic component surfaces are smaller, if the pumps run for a long enough time, then the plastic desorption can dominate the metal surface desorption. Indeed the polymer desorption rate Q_{diff} decreases less slowly than that of the metal surface. By way of comparison, the metal desorption decreases linearly as a function of time, while the polymer desorption decreases with \sqrt{t} .

Note that after some time, this flow rate also becomes negligible. Therefore, Q_{diff} is equal to zero after a while.

3.1.3 Permeation and leaks

When the pressure difference between the ambient environment and the chamber medium (of the order of 10^{-8} mbar) becomes sufficiently large, small particles such as helium can diffuse through the joints and the walls of the installation. This phenomenon also called permeation, is independent of time and increases pressure constantly. Its flow rate Q_{perm} varies according to the pressure gradient but also the thickness and the permeability of the wall.

Finally, if the installation has leaks, i.e. an “opening” in a wall or seal, then ambient gas can enter the installation. Like permeation, this source of contamination increases pressure steadily. Its rate Q_l depends on the pressure difference between the chamber and the external environment.

3.1.4 Impact on the pressure

After pump down of a chamber in the case of pump shutdown, the evolution of its pressure as a function of time is given by curve 3 of Figure 3.1. As shown by this graph, its increase is the result of two types of contribution. Curve 1 represents the increase in pressure caused by constant sources of contamination such as permeation and leaks. Curve 2 represents the pressure evolution caused by phenomena varying over time as desorption.

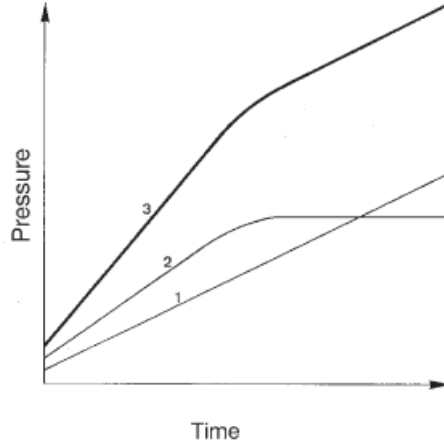


Figure 3.1: Pressure evolution of an isolated vacuum chamber exposed to different contamination rate from [10]

If a vessel is continuously pumped out at a volume flow rate S , its internal medium can reach an equilibrium pressure, the ultimate pressure P_u . It corresponds to the pressure reached when the sum of contamination flux and the flux exiting by the pump are the same. Its value depends on all the phenomena discussed above and on the pumping speed. Its expression as a function of time t is

$$P_u(t) = \frac{Q_{des}(t) + Q_{diff}(t) + Q_{perm} + Q_l}{S},$$

where Q_{des} , Q_{diff} , Q_{perm} and Q_l are expressed in [mbar.L/s], the pumping speed in [L/s] and the ultimate pressure in [mbar].

For practical reasons, the total leak rate Q_{leak} considering all the contamination phenomena is defined as

$$P_u(t) = \frac{Q_{leak}(t)}{S}.$$

If the installation has been operating for long enough, the total leak flux stabilizes at a constant value. According to this value, it is possible to classify the facility according to three categories:

- when $Q_{leak} < 10^{-6}$ mbar.L/s, the system is considered “very tight”,
- when $10^{-4} > Q_{leak} > 10^{-6}$ mbar.L/s, the system is “sufficiently tight”,
- when $Q_{leak} > 10^{-4}$ mbar.L/s, the system is “leaky”.

3.2 Pumping system

In the field of vacuum technology, there is a wide variety of vacuum pumps. Depending on the operating principle, they are not all used for the same applications and the same type of flow. As the installation of the VKI uses a wide pressure interval, two types of pump are used. This section only presents the types of pump used by the installation.

3.2.1 Types of vacuum

As a reminder of Section 2.2, the ratio of the mean free path to the macroscopic scale length, as flow channel diameter, is the Knudsen number Kn . This number characterizes the degree of rarefaction and for a given characteristic length assigns it to a pressure range. When $Kn < 0.01$, the flow is assumed viscous flow or continuous. The collisions between gas molecules are frequent. The mean free path of the gas molecules is significantly shorter than the dimensions of the flow channel. It is the Low Vacuum.

When $0.01 < Kn < 0.5$, the flow is called Knudsen flow. The vacuum associated with this Knudsen number is the medium vacuum.

Finally, when $Kn > 0.5$, the flow is molecular. The mean free path is much greater than the diameter of the flow channel. And the molecular interaction no longer happens. This situation corresponds to the High or Ultra-high vacuum.

Table 3.1 summarizes the classification of the different types of vacuum.

Vacuum type	Low Vacuum	Medium Vacuum	High/Ultra-High Vacuum
Flow type	Viscous flow	Knudsen flow	Molecular flow
Knudsen number	$Kn < 0.01$	$0.01 < Kn < 0.5$	$Kn > 0.5$

Table 3.1: Overview of types of flow regimes.

Figure 3.2 linked them to the pressure.

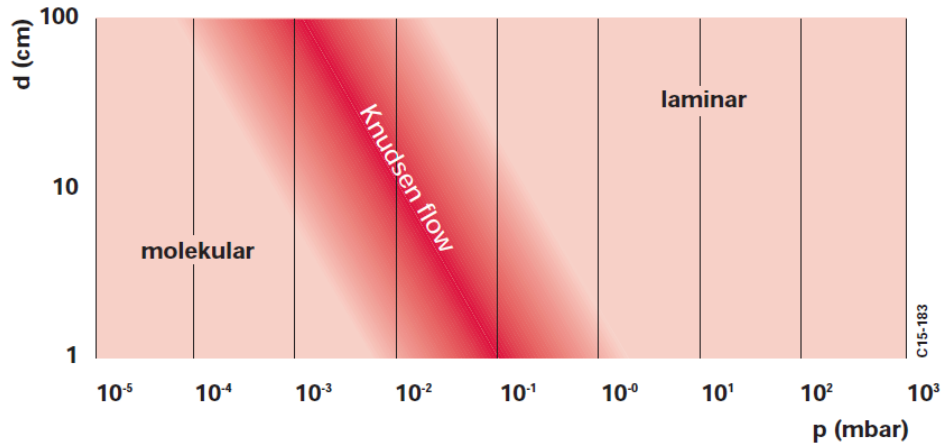


Figure 3.2: Representation of flow range dependant on pressure and characteristic length scale.

3.2.2 Rotary vane pump

Rotary vane vacuum pumps are usable for the entire low and medium vacuum ranges. As described in Figure 3.3, a rotary vane pump is composed of a housing (1), an eccentrically installed rotor (2), vanes (3) that move radially, the inlet and outlet (4). The working chamber (5) in the housing is restricted by the stator, rotor, and vanes. When the rotor rotates, gas enters the suction chamber until a second vane seals the passage. The gas is then confined in the vane and compressed until the outlet

valve opens against atmospheric pressure. The oil used by the pump lubricates the moving parts, fills unoccupied volumes, compresses the space between the blades, and allows an optimal thermal balance by heat transfer. But the outlet valve must stay oil-sealed.

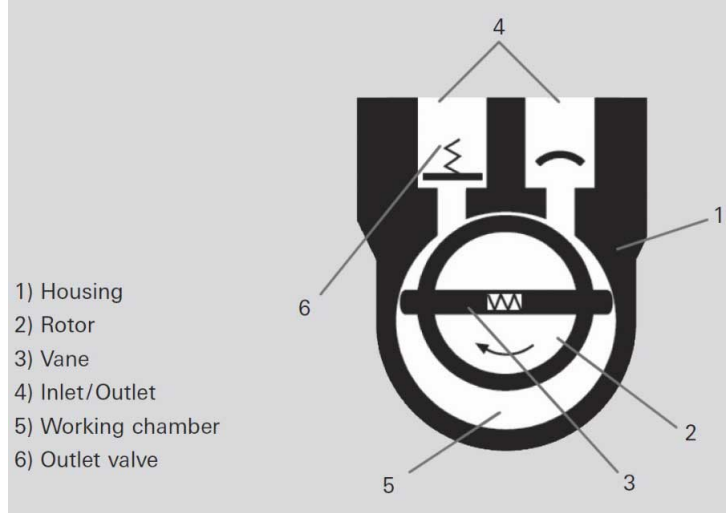


Figure 3.3: Operating principle of a rotary vane pump.

The pump used in the installation of the VKI has some additional features. First, it is fitted with a vacuum safety valve to isolate the pump when the installation standstill and prevents oil from entering the vacuum chamber. Then, the pump has two stages to reach lower ultimate pressures. Finally, it can perform a gas ballast operation. This procedure prevents some components from condensing during the compression. This condensation is dangerous for the pump operation because it can contaminate the oil and reduce the pumping performance. Furthermore, if there are corrosive species, it may damage the structure of the pump. During a gas ballast operation, gas from outside is injected into the sealed suction chamber. The pressure increases and the outlet valve opens more rapidly. Therefore, the compressed gas no longer has time to condense.

This type of pump is used in the installation as a backing pump. It allows reducing sufficiently the pressure (about 0.1 mbar) in order for the turbomolecular pumps to start. As shown in the next section, these are able to further decrease the pressure.

3.2.3 Turbomolecular pump

The principle

The principle of operation of a turbomolecular pump is illustrated in Figure 3.4. A particle moves according to its random thermal velocity. If this particle collides a moving orifice or opening, its velocity post-collision is composed of its thermal velocity and a component in the direction of the motion of the opening. In addition, if a second orifice faces the first one, then the process repeats. The new velocity components added to the initial thermal velocity yield a final directional velocity. If it is large enough, the particle can go according to the desired direction. It is

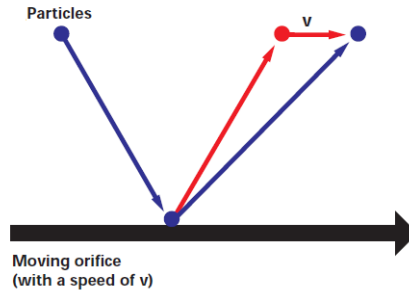


Figure 3.4: Principle of the molecular pump

this directional movement that allows pumping of the gas. In reality, the blades of the turbopump play the role of these ideal moving orifices. This process is only applicable when the mean free path is at least higher than the distance between the two moving orifices. In fact, if the pressure is too high, the mean free path may be small, such that the particle leaving the first orifice loses the new velocity component by collision with other particles. It never acquires sufficient speed to allow it to be evacuated from the room. Therefore, this process does not work for a Low Vacuum. But in a molecular flow, the mean free path becomes much higher than the distance between the blades. Each blade imposes a new velocity component to the vessel exit, and the particle releases efficiently. As this process only works for molecular flow, pumps using this principle are called molecular pumps.

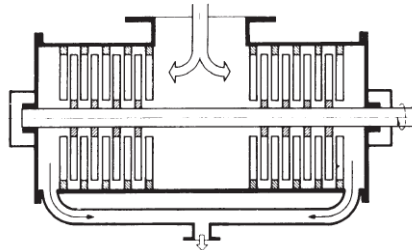


Figure 3.5: Schematic of a turbomolecular pump

A turbopump is a molecular pump composed of rotors similar to turbine rotors. Their blades rotate between corresponding stator blades as depicted in Figure 3.5.

Pumping speed

The most important parameter of a turbomolecular pump is its pumping speed S . It corresponds to the mean volumetric flow rate of the gas through the cross-section of the pump intake, and it is expressed in [L/s]. It depends on the pump entrance area and the blades' rotation speed. But it also varies in function of the used gas. The pumping speed dependence on the type of gas is represented in Figure 3.6. It appears that for a given pump, the speed decreases as the mass increases.

In a molecular flow corresponding to the High and Ultra-High Vacuum, the pumping speed is independent of the pressure. It decreases in the Medium Vacuum and tends to zero in the Low Vacuum. A typical pumping speed evolution following the intake pressure is shown by Figure 3.7.

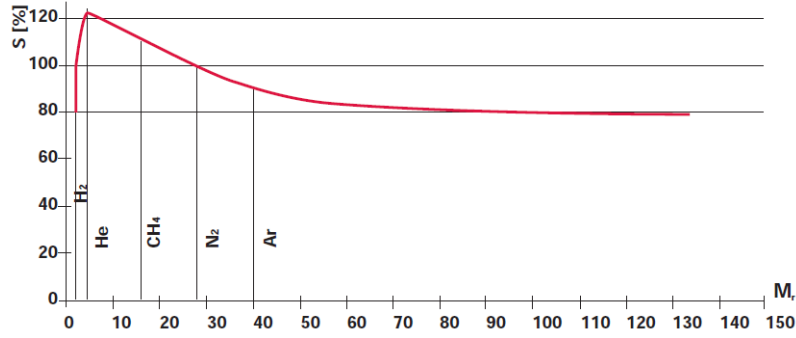


Figure 3.6: Pumping speed S as a function of the relative molecular mass M_r .

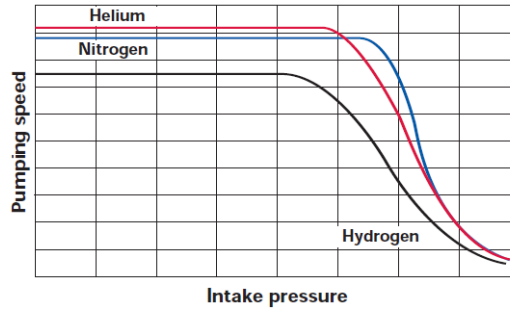


Figure 3.7: Pumping speed as a function of the pressure for various gases.

When the chamber pressures reach acceptable values (thanks to the backing pump), the installation's turbopumps switch on. As shown in Chapter 4, these will allow to reach pressures of the order of 10^{-8} mbar.

3.3 Particle flow generator

The Particle Flow Generator (PFG) used by the VKI facility is provided by the company ThrustMe and allows simulating the environment in Very Low Earth Orbit. The device is composed of a plasma source, where neutral gas is split into ions and electrons, and of a system to accelerate the ions produced. Its operation is similar to a gridded ion thruster. The principle of this thruster is presented by Figure 3.8.

This propulsion system uses a discharge chamber equipped with an electron gun. The feed gas is ejected into this cavity and is ionized by the electrons from the gun. The ions then released pass through two highly electrically charged grids and thus undergo an acceleration. Note that these same grids confine the electrons within the cavity. Thus they have a better chance of ionizing a gas molecule. At the output of the plasma generator, a charged grid set accelerate further the ions to generates the plume.

According to [25], the PFG it is not equipped with a cathode. An important parameter to characterize the plasma plume is the mass utilization η_m . It corresponds to the ratio of the number of ionized particles to the total number of particles emitted by the PFG. This parameter is particularly important as it dictates the ratio of fast to slow particles leaving the PFG exit.

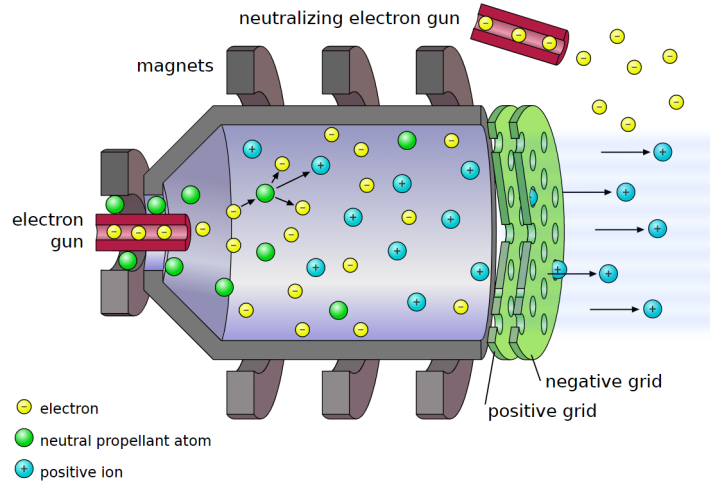


Figure 3.8: Principle of a gridded ion thruster from [23]

3.4 Conclusion

This chapter introduces the different contamination phenomena induced by the generation of a vacuum medium. These phenomena involve different sources of particles entering the installation. And for a given pumping system, they allow the pressure to stabilize at a certain value: the ultimate pressure.

Secondly, this chapter discusses the basic principle and the specifics of different equipment in the installation. The pumping system is composed of a backing pump and two turbopumps. The backing pump is a rotary vane pump and allows the pressure in the two chambers to reach values of around 0.1 mbar. At this moment, the turbopumps continue to decrease the pressure of the chambers that allow them to reach 1×10^{-8} mbar. Only the turbopumps are considered in the model of Chapter 4. At sufficiently low pressure, they evacuate a constant volumetric flow rate S .

The Particle Flow Generator (PFG) is also covered in this chapter. Its operating principle is similar to that of a gridded ion thruster. It simulates the flow of atmospheric gas encountered by the VLEO satellite. The ion proportion contained in the particle flow corresponds to the mass utilization η_m .

Chapter 4

Development of the 0-D model

The numerical model used to follow the evolution of the pressure in the installation is described in this chapter. The first section defines the parameter related to the performance of the intake which should be determined by the series of tests proposed in Chapter 5. The second part discusses the assumptions and equations used by the simulations. Finally, the last part is devoted to analytical verification.

4.1 Transmission probabilities of ducts

As explained in Section 3.2, the mean free path of a High or Ultra-High vacuum is large compared to the tube size. Collisions between particles are therefore negligible within the duct. If a particle passes through the tube, it only collides with the walls. According to [15], the number of particles is always high. And the duct crossing flow calculation requires a statistical approach.

If a gas particle passes through the entrance plane of the component possibly making wall collisions, the probability that this particle exits through the exit plane of the path is the transmission probability τ . By considering Figure 4.1, the particle flow in [particle/s] exiting through the duct outlet is

$$\dot{N}_{1,out} = \tau \dot{N}_{in},$$

with \dot{N}_{in} the total particle flux in [particle/s] entering the duct. And the particle flow in [particle/s] returning to the duct inlet is

$$\dot{N}_{2,out} = (1 - \tau) \dot{N}_{in}.$$

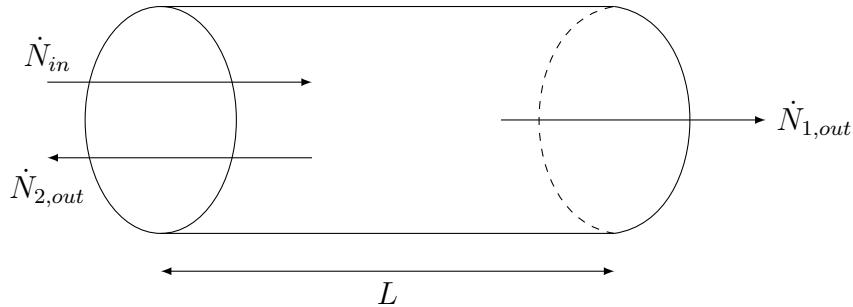


Figure 4.1: Representation of the fluxes defining the duct transmission probability.

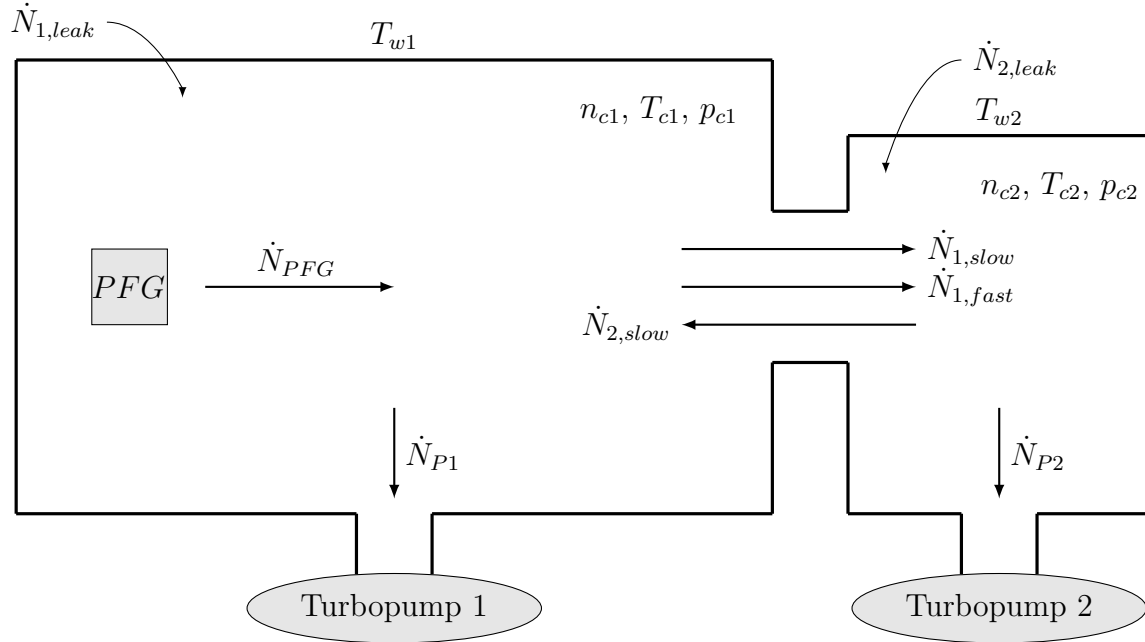


Figure 4.2: Representation of the VKI's facility variable used in the model

It is this parameter which will have to be determined following a series of tests in Chapter 5.

4.2 Analytical model

This section deals with a simple numerical model describing the pressure evolution for different possible installation configurations.

4.2.1 Description of the model

To simulate the VKI facility operation, the model presented in Figure 4.2 is used. This system is composed of two chambers, the main chamber on the left and the secondary chamber on the right. Both turbopumps are connected to a backing pump (not shown in the figure). This simply provides a sufficient vacuum for the operation of the turbopumps, and will not be considered in this work. The vessels are linked together by a duct equipped with a gate valve that can isolate one chamber from the other. Finally, the Particle Flow Generator (PFG) is placed in the first chamber perfectly aligned with the duct inlet.

To facilitate the analysis, a hypothesis set is imposed:

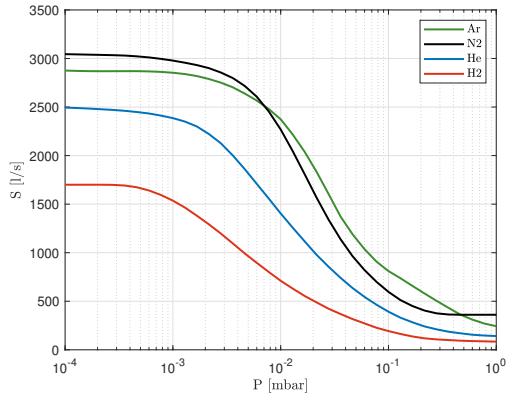
- The flow is free molecular everywhere, i.e. particles only collide with walls and not between themselves.
- All background particles in the main chamber have collided (at least one time) with the primary chamber wall.
- All background particles in the secondary chamber have collided (at least one time) with the secondary chamber wall.

- After collision with the facility walls, background particles get a Maxwellian distribution at the wall temperature, thus the temperature of the gas in the main chamber T_{c1} is considered equal to the temperature of the main chamber's wall T_{w1} . And the temperature of the gas in the secondary chamber T_{c2} is considered equal to the temperature of the secondary chamber's wall T_{w2} .
- The total PFG flux is imposed in SCCM (Standard Cubic Centimeters per Minute) and doesn't depend on the main chamber conditions. When it is expressed in [particle/s], it is written \dot{N}_{PFG} .
- The flux extracted by the turbopumps, in [particle/s], only depends on their adjacent chamber pressure, therefore $\dot{N}_{P1}(p_{c1})$ and $\dot{N}_{P2}(p_{c2})$.
- To consider the desorption, diffusion, permeation, and leaks phenomena, the chambers are subject to constant entering flows of particles $\dot{N}_{1,leak}$ and $\dot{N}_{2,leak}$ in [particle/s] or $Q_{1,leak}$ and $Q_{2,leak}$ in [mbar.L/s]. The leak gas is assumed of the same species as the working gas.
- The perfect gas law $p = nkT$ can be used. With p the pressure, n the number of particle per volume unit, k the Boltzmann constant and T the temperature.

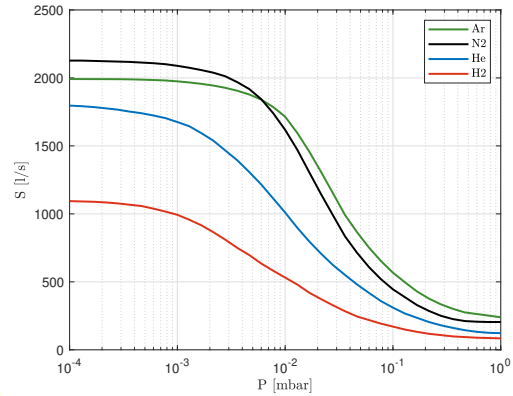
For clarity, each type of flow is treated separately.

Turbopumps flux \dot{N}_{p1} and \dot{N}_{p2}

The volumetric flow rate that a turbopump can extract depends on the pump geometry, operational characteristics, and state of the gas reservoir upstream. A procedure for the theoretical prediction of this performance can be found in [28]. In this work the performance curves provided by the manufacturer (4.3a and 4.3b) are used. They represent the realistic operation of the device.



(a) Pump capacity of the main chamber turbo-pump for different gas from [27]



(b) Pump capacity of the secondary chamber turbo-pump for different gas from [26]

As shown in these figures, the pump speeds also vary with the used gas. Note that these curves oblige to consider only one gas at a time. For the remainder of the report, argon is the main gas used.

As seen in Section 3.2, the turbopump pumping speed is independent of the pressure in the molecular flow range. Below the lowest graph pressures, the curves become a horizontal straight line, and the turbopump speeds stay constant.

By defining the molar volume of gas, from the perfect gas law ($pV = NRT$)

$$V_m = \frac{V}{N} = \frac{RT}{p},$$

where V is the volume in $[m^3]$, N is the number of moles, R in $[J/(mol.K)]$ is the universal ideal gas constant, T the gas temperature in $[K]$ and p the gas pressure in $[Pa]$.

The turbopumps pumping speed are converted in $[particle/s]$ by the expression

$$N_{pi} = S_i \times \left(\frac{N_a}{V_{m,i}} \right) \quad i = 1 \text{ or } 2,$$

where N_{pi} is the turbopump flux of the chamber i in $[particle/s]$, S_i is the turbopump flux of the chamber i in $[L/s]$, $V_{m,i}$ is the gas molar volume in the chamber i in $[L/mole]$ and N_a is the Avogadro constant.

PFG flux \dot{N}_{PFG}

The total PFG flux is imposed in SCCM (Standard Cubic Centimeters per Minute). This a flow unit gives the volume flux in cubic centimeters per minute in standard conditions for temperature and pressure. In the case of SCCM flux, these standard conditions are $T_n = 273.15$ K and $p_n = 101325$ Pa. By introducing the corresponding standard gas molar volume $V_{m,n}$ in $[m^3/mol]$

$$V_{m,n} = \frac{RT_n}{p_n}.$$

The units are used to find an expression of the PFG flux in $[particle/s]$

$$\frac{SCCM}{6 \times 10^7} \frac{1}{V_{m,n}} N_a \equiv \left[\frac{m^3}{s} \right] \left[\frac{mol}{m^3} \right] \left[\frac{particle}{mol} \right] \equiv \left[\frac{particle}{s} \right].$$

Therefore, it is given by

$$\dot{N}_{PFG} = \frac{SCCM}{6 \times 10^7} \times \frac{N_a}{V_{m,n}}.$$

Fluxes from the main chamber to the secondary chamber $\dot{N}_{1,fast}$ and $\dot{N}_{1,slow}$

There are two flux sources for the flux from chamber one to chamber two: the PFG and the background gas. The contribution from the PFG can be further split in two:

- fast and directional particles flux
- an isotropic slow particles flux

The first one is only composed of fast ions able to reach the duct connecting the two chambers. Among these ions, only a fraction f_{ion} reaches the valve. This fraction depends on the distance between the PFG and the duct inlet diameter d_{PFG} , and the fast-flux speed ratio S_p defined in the Section 2.3. More details about f_{ion} are available in the next subsection 4.2.2.

Once entered in the valve, not all the ions go to the second chamber. As explained in section 4.1, the probability that they reach the other side is $\tau_{1,fast}$. Note that the speed vector being quite aligned along the valve axis, this transmission probability is relatively high.

The fast flux in [particle/s] is then

$$\dot{N}_{1,fast} = f_{ion}\eta_m\dot{N}_{PFG}\tau_{1,fast},$$

with \dot{N}_{PFG} the total PFG flux in [particle/s], η_m the mass utilization defined in Section 3.3, $\tau_{1,fast}$ the transmission probability of the fast flux towards the secondary chamber.

The second PFG flux is isotropic, and composed of slow particles. It is assumed not directional enough to transmit to the second chamber, and it will simply supply the background gas of the main chamber.

The second flux source is the background gas. It also generates flux going from the main chamber to the other one. But as its speed ratio is null, it is a thermal flow. By considering the section 2.3, the flux of a thermalized gas expressed in [particle/s] through a surface is

$$\dot{N}_{1,slow} = \frac{n_{c1}}{4}\langle v_1 \rangle A_1 \tau_{1,slow},$$

where $\langle v_1 \rangle$ is the background particle mean velocity of the first chamber in [m/s], A_1 is the duct area in [m²] and $\tau_{1,slow}$ is the transmission probability of the slow flux towards the secondary chamber.

As this flow does not have a speed vector aligned with the valve, $\tau_{1,slow}$ is smaller than $\tau_{1,fast}$. Again thanks to the reasoning of the section 2.3, the mean speed is equal to

$$\langle v \rangle = \sqrt{\frac{8kT}{\pi m}},$$

where m is the mass of one particle in [kg]. And by using the perfect gas law, the slow flux becomes

$$\dot{N}_{1,slow} = \frac{p_{c1}}{4kT_{c1}} \sqrt{\frac{8kT_{c1}}{\pi m}} A_1 \tau_{1,slow} = p_{c1} A_1 \tau_{1,slow} \sqrt{\frac{1}{2\pi m k T_{c1}}},$$

where p_{c1} is the main chamber pressures in [Pa].

Finally the fluxes from the main chamber to the secondary chamber are given by

$$\begin{aligned} \dot{N}_{1,fast} &= f_{ion}\dot{N}_{PFG}\eta_m\tau_{1,fast} \\ \dot{N}_{1,slow}(p_{c1}) &= p_{c1}A_1\tau_{1,slow}\sqrt{\frac{1}{2\pi m k T_{c1}}}. \end{aligned}$$

Flux from the secondary chamber to the main chamber $\dot{N}_{2,slow}$

In the secondary chamber, there is no flow generator, but there is a background gas. As in the main chamber, this gas is also a flux source. It creates a thermal flow going to the first vessel. The expression of the total flow going to the first chamber is therefore

$$\dot{N}_{2,slow}(p_{c2}) = p_{c2} A_2 \tau_{2,slow} \sqrt{\frac{1}{2\pi m k T_{c2}}},$$

with $\tau_{2,slow}$ the transmission probability of the slow flux towards the main chamber, p_{c2} the secondary chamber pressures in [Pa], and A_2 the area of the connecting duct at the second chamber wall level in [m²].

Model equation

To study the pressure evolution of each chamber, the model uses the continuity equation. It considers the different particle fluxes defined previously. The mass conservation principle gives for each chambers the relations

$$\begin{aligned} \dot{N}_{PFG} + \dot{N}_{2,slow}(p_{c2}) + \dot{N}_{1,leak} - \dot{N}_{P1}(p_{c1}) - \dot{N}_{1,fast} - \dot{N}_{1,slow}(p_{c1}) &= V_1 \frac{d}{dt}(n_{c1}), \\ \dot{N}_{1,fast} + \dot{N}_{1,slow}(p_{c1}) + \dot{N}_{2,leak} - \dot{N}_{P2}(p_{c2}) - \dot{N}_{2,slow}(p_{c2}) &= V_2 \frac{d}{dt}(n_{c2}). \end{aligned}$$

The flux are expressed in [particle/s], the volume chambers V_1 and V_2 in [m³] and the chambers number densities n_{c1} and n_{c2} in [particle.m⁻³].

Since the temperatures are assumed constant, manipulation of the perfect gas law yields

$$\begin{aligned} \frac{d}{dt}(n_{c1}) &= \frac{1}{kT_{c1}} \frac{d}{dt}(p_{c1}), \\ \frac{d}{dt}(n_{c2}) &= \frac{1}{kT_{c2}} \frac{d}{dt}(p_{c2}). \end{aligned}$$

where p_{c1} , and p_{c2} are the chamber pressures in [Pa].

By inserting these latter in the first two equations, the final system corresponds to a set of first order differential equations.

$$\frac{d}{dt}(p_{c1}) = \frac{kT_{c1}}{V_1} \left(\dot{N}_{PFG} + \dot{N}_{2,slow}(p_{c2}) + \dot{N}_{1,leak} - \dot{N}_{P1}(p_{c1}) - \dot{N}_{1,fast} - \dot{N}_{1,slow}(p_{c1}) \right) \quad (4.1)$$

$$\frac{d}{dt}(p_{c2}) = \frac{kT_{c2}}{V_2} \left(\dot{N}_{1,fast} + \dot{N}_{1,slow}(p_{c1}) + \dot{N}_{2,leak} - \dot{N}_{P2}(p_{c2}) - \dot{N}_{2,slow}(p_{c2}) \right)$$

4.2.2 Ion fraction reaching the duct inlet

To calculate the fraction of PFG ions that reach the inlet of the valve, two methods were used: the View factor method and the Test Particle Monte Carlo method (TPMC).

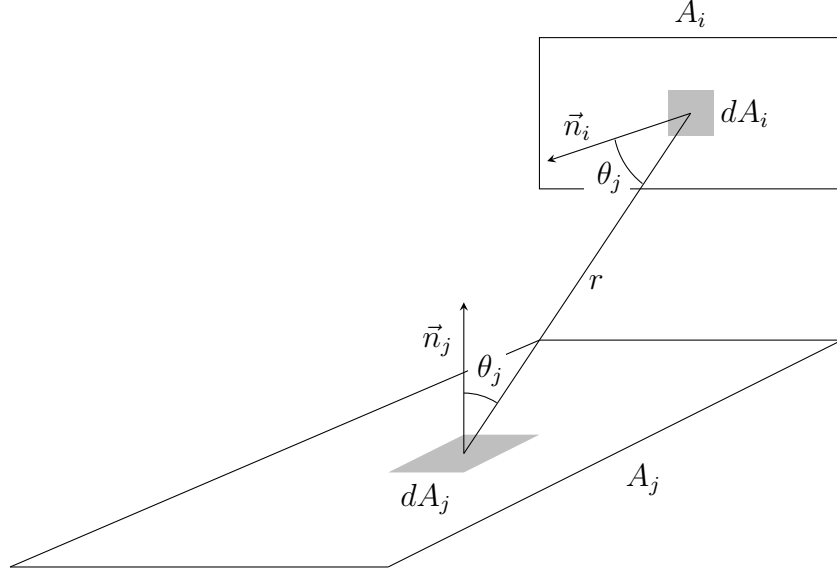


Figure 4.4: Scheme of an infinitesimal surface dA_i emitting a radiation towards the infinitesimal surface dA_j at a distance r .

View-factor method

The View Factor method is often used to calculate the radiation heat transfer. But in the case of this study, this method can provide the ion fraction reaching the valve inlet. It is based on two assumptions. The gas is free molecular, and the surface collisions are diffuse. This last condition implies that the scattered particle velocities are distributed according to a Maxwellian distribution at the wall temperature, independently of incident ones.

The method is to use the view factor F_{ij} . It represents the radiation fraction emitted from the surface A_i and received by the other surface A_j (as illustrated in Figure 4.4).

According to [17], the general expression of the view factor is

$$F_{ij} = \frac{1}{A_i} \int_{A_i} \int_{A_j} \frac{\cos(\theta_i) \cos(\theta_j)}{\pi r^2} dA_i dA_j,$$

where r represents the distance between the surfaces centers and the cosines θ_i and θ_j denote the angles between r and the normal vectors of A_i and A_j respectively.

As shown in [22], the particles flux Φ_{ij} is related to the view factor by the relation

$$\Phi_{ij} = \Gamma_i F_{ij} M_{ij},$$

with Γ_i the thermal mass flux through a surface and M_{ij} a parameters considering the flux alteration caused by the non-zero streaming velocity of the gas. The two last expression provide the flux relation

$$\Phi_{ij} = \Gamma_i \frac{1}{A_i} \int_{A_i} \int_{A_j} \frac{\cos(\theta_i) \cos(\theta_j)}{\pi r^2} M_{ij} dA_j dA_i. \quad (4.2)$$

In the case of the VKI facility:

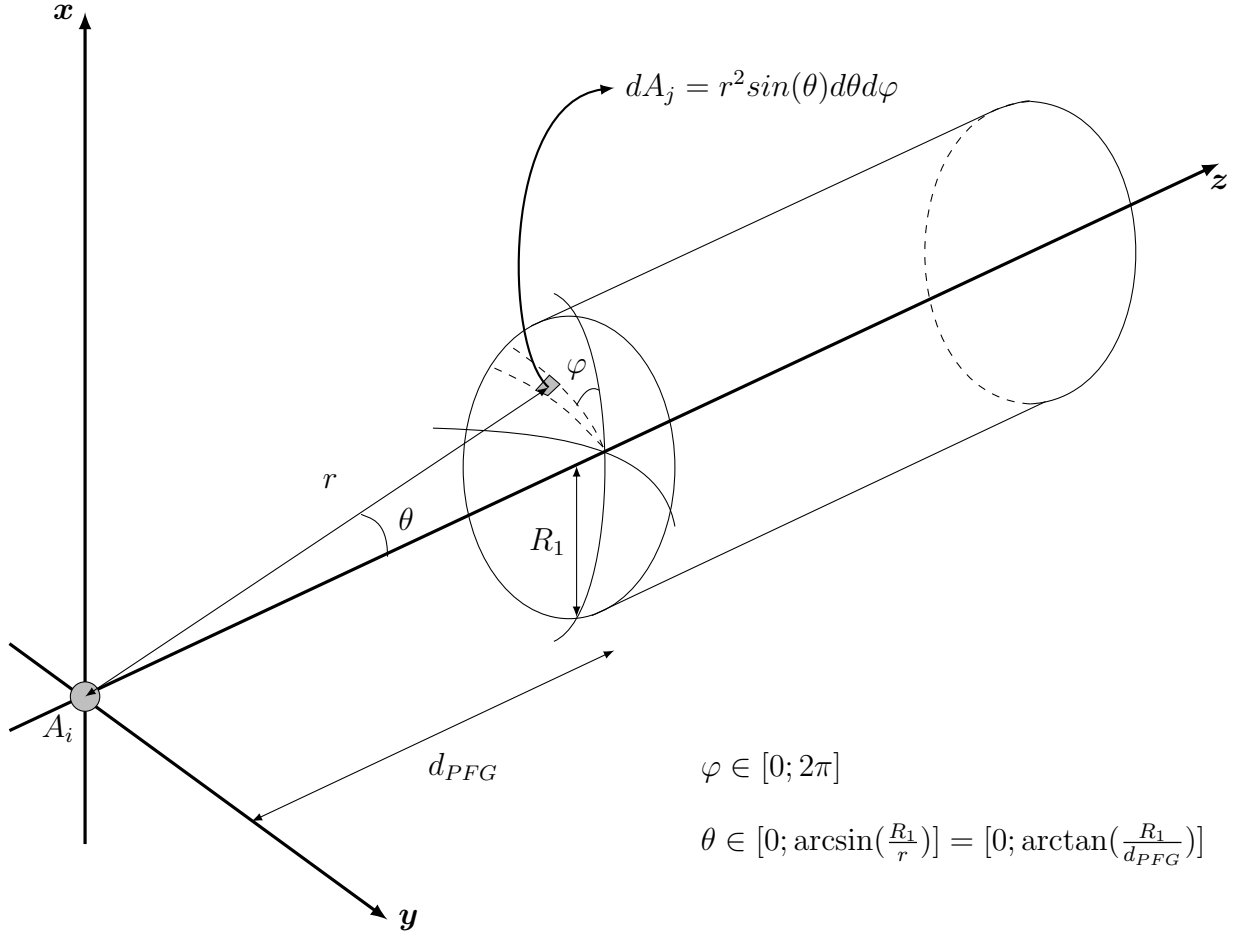


Figure 4.5: Scheme of the infinitesimal PFG surface dA_i emitting a radiation towards the infinitesimal duct entrance surface dA_j at a distance r .

- A_i corresponds to the PFG area. As the dimension of the PFG is small compared to the distance separating it from the duct d_{PFG} , this surface is considered infinitesimal.
- $\Gamma_i = \frac{1}{4}n\sqrt{\frac{8kT}{\pi m}}$ is the thermal mass flux through the PFG surface.
- r is the radius of the sphere passing through the edge of the connecting duct centered at the PFG.
- $A_j = \pi r^2$ is the sphere portion at the valve entrance area.
- M_{ij} takes into account the alteration of the PFG flux. It depends on the gas speed ratio S_p and the angle between the velocity vector and the line-of-sight between surfaces dA_i and dA_j .

As shown in Figure 4.5, the PFG is aligned with the valve and the the gas velocity vector is parallel to the normal vector of the PFG surface. It is possible to assume

$$\theta_i = \theta \quad \theta_j = 0 \quad \sigma = S \cos(\theta).$$

And the last term becomes

$$M_{ij} = e^{-S^2} [\sqrt{\pi} \sigma e^{\sigma^2} (\sigma^2 + \frac{3}{2}) (1 + \text{erf}(\sigma)) + \sigma^2 + 1].$$

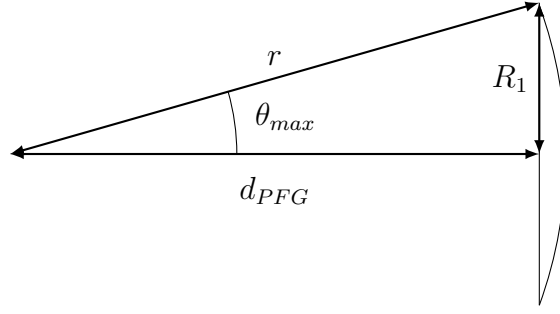


Figure 4.6: Profile view of the duct entrance.

Note that the ion flux can be fast and the resulting distribution anisotropic.

As represented in Figure 4.6, two distances can be used to express the maximum value of θ .

For practical reasons, the distance between the PFG and the valve center d_{PFG} is chosen and the integral upper limit is $\theta_{max} = \arctan(\frac{R_1}{d_{PFG}})$. As $\dot{N}_{1,fast}$ is the fast ion flux actually entering the second chamber, the fast ion flux at the inlet of the duct is equal to $\frac{\dot{N}_{1,fast}}{\tau_{1,fast}}$. By considering the expression 4.2, it is given by

$$\begin{aligned}
 \frac{\dot{N}_{1,fast}}{\tau_{1,fast}} &= \Gamma_i \frac{1}{A_i} A_i \int_{A_j} \frac{\cos(\theta) \cdot 1}{\pi r^2} M_{ij} dA_j \\
 &= \Gamma_i \int_0^{2\pi} \int_0^{\theta_{max}} \frac{\cos(\theta)}{\pi r^2} M_{ij} r^2 \sin(\theta) d\theta d\varphi \\
 &= \Gamma_i \int_0^{2\pi} \int_0^{\theta_{max}} \frac{\cos(\theta)}{\pi} M_{ij} \sin(\theta) d\theta d\varphi \\
 &= \frac{\Gamma_i}{\pi} 2\pi \int_0^{\theta_{max}} \cos(\theta) \sin(\theta) M_{ij} d\theta \\
 &= 2\Gamma_i \int_0^{\theta_{max}} \cos(\theta) \sin(\theta) M_{ij} d\theta
 \end{aligned}$$

Considering that the fast ionised particle flow emit by the PFG is given by

$$\dot{N}_{PFG,fast} = 2\Gamma_i \int_0^{\frac{\pi}{2}} \cos(\theta) \sin(\theta) M_{ij} d\theta.$$

The fraction of fast ionised particle emitted by the PFG which reach the valve entrance is equal to

$$\begin{aligned}
 f_{ion} &= \frac{\dot{N}_{1,fast}/\tau_{1,fast}}{\dot{N}_{PFG,fast}} \\
 &= \frac{\int_0^{\theta_{max}} \cos(\theta) \sin(\theta) M_{ij} d\theta}{\int_0^{\frac{\pi}{2}} \cos(\theta) \sin(\theta) M_{ij} d\theta}
 \end{aligned}$$

Figure 4.7 shows the evolution of this parameter as a function of the speed ratio and the PFG-valve inlet distance. It appears that the higher the speed ratio, the

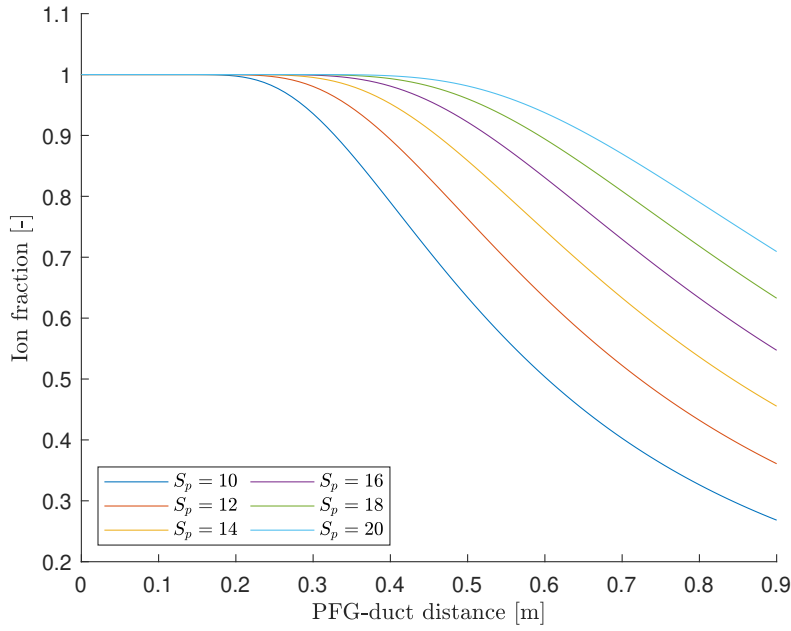


Figure 4.7: Evolution of the ion fraction in function of PFG-valve distance

higher the ion proportion reaching the inlet of the valve. Conversely, the greater the distance, the more this fraction decreases.

Test Particle Monte Carlo method

The fraction of particles reaching the connecting duct can also be computed using the TPMC method. It consists of tracking the trajectories of particles in 3D space, where each particle is independent of the others. The initial velocities of the particles are randomly sampled from appropriate distributions, in this case a drifting maxwellian with appropriate speed ratio. The initial position is randomly generated on the real PFG emitting surface (contrary to the single point assumption employed for the view-factor method). Once arrived at the chamber wall, it is possible to test whether it enters the duct or remains in the main chamber. By repeating this process many times, the ion fraction can be computed to the desired precision. This method is also able to determine specify. The fast flux transmission probability. Indeed, some thermal flow transmission probabilities are easily found from data present in numerous resources (see [8]). But when the particles have a non-zero speed at the valve entry as in this case, it becomes tricky to find appropriate data in literature corresponding to this specific case.

The method can determine this transmission probability. For that, it continues to follow the particle once it has entered the pipe. To know the side where the particle leaves, the algorithm can consider different collision models. In the case of this study, only the Maxwell model is used. This model considers the parameter a called accommodation coefficient, which corresponds to the diffuse collision rate. It means that $100 \times a\%$ of the time the collision is a diffuse collision and $100 \times (1 - a)\%$ of the time the collision corresponds to a specular collision.

This parameter depends on the surface characteristics and determines the particle behavior following a surface collision. If the particle experiences a diffuse

collision, it is re-emitted from the surface with a Maxwellian velocity distribution corresponding to the wall temperature. If the collision is specular, then the momentum exchange occurs just along the normal direction. The reflected particle leaves along the specular direction.

Again, a large number of simulations can provide the particle percentage reaching the other side. In the case of this study, all the simulations consider an accommodation coefficient equal to 1. Therefore all surface collisions are diffuse collisions.

Comparison of both methods

Both methods have advantages and disadvantages.

The first is fast, easily implemented on MATLAB, and provides an accurate value of the ionic fraction. However, it is required to find another model determining the transmission probability of the fast stream, as little data is available for this specific case.

The second provides the fraction of the ions and the transmission probabilities $\tau_{1,fast}$, $\tau_{1,slow}$, and $\tau_{2,slow}$. As this method needs a lot of simulation, the values are determined by interpolating a data series calculated by this program. The results may lose some of their precision although not compromising the validity of the presented analysis and its qualitative conclusions.

The decisive argument for the choice is the validity of the point source assumption. As shown in Figure 4.8, this difference impacts the ion fraction. The greater the distance separating the PFG from the valve and the speed ratio, the smaller the model error of the view factor. In the case of the installation, the distance cannot exceed the length of the main chamber (0.9 m), and the speed ratio is about 10. According to the graph, the error of the view factor method can become significant. Given the availability of the data, the model of this study is therefore based on the values obtained by the TPMC method.

4.3 Verification of the model

This section is devoted to model checking. First, its results are compared with exact theoretical values of the steady-state pressures of both chambers. Following the valve and PFG states, four cases are studied:

- the valve at the duct entrance is closed and the PFG is not fed with gas.
- the valve is closed but the PFG is fed with gas
- the valve is open but the PFG flux is null.
- the valve open and PFG turned on.

Then, the pressure evolution of the model is compared to the theoretical temporal function. As this step requires solving the differential equation, only the simplest case (valve and PFG closed) is analyzed.

A nominal configuration is defined in Table 4.1. These different values have been chosen to remain consistent with reality. But the installation being not yet complete, they represent the current best estimates.

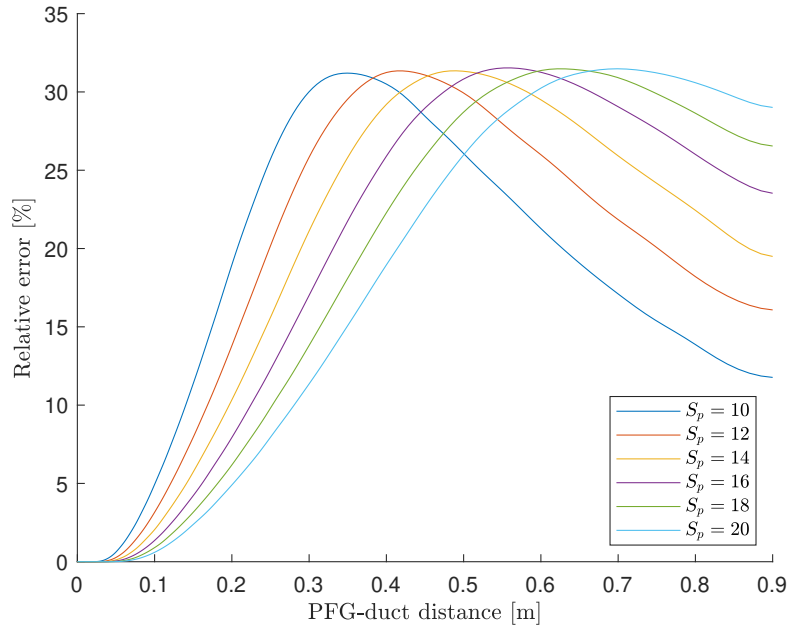


Figure 4.8: Evolution of the Relative difference between the View factor method and TPMC method in function of the PFG-valve distance

PFG	Gas	Argon	[-]
	PFG flux $SCCM$	3	[SCCM]
	Mass utilization η_m	0.05	[-]
	Speed ratio S_p	10	[-]
	PFG-valve distance d_{PFG}	0.6	[m]
Main chamber	Temperature T_{c1}	300	[K]
	Volume V_1	0.2545	[m ³]
	Leak flux $Q_{1,leak}$	10^{-4}	[mbar.L/s]
	Initial pressure $p_{c1}(t = 0)$	10	[Pa]
Secondary chamber	Temperature T_{c2}	300	[K]
	Volume V_2	0.0177	[m ³]
	Leak flux $Q_{1,leak}$	10^{-4}	[mbar.L/s]
	Initial pressure $p_{c2}(t = 0)$	10	[Pa]
Theoretical pumping speed	First turbopump S_1	2900	[L/s]
	Second turbopump S_2	2000	[L/s]
Duct	Inlet area A_1	0.0079	[m ²]
	Outlet area A_2	0.0011	[m ²]
	Length L	0.3	[m]
	Accommodation coefficient a	1	[-]

Table 4.1: Nominal conditions imposed during the code verification

As explained in Section 4.2, the ion fraction and the transmission probabilities are determined from the installation parameters. By considering the nominal conditions listed on 4.1, their nominal values are displayed in Table 4.2.

Ion proportion reaching the duct f_{ion}	0.4230	[-]
Transmission probability $\tau_{1,fast}$	0.2350	[-]
Transmission probability $\tau_{1,slow}$	0.0602	[-]
Transmission probability $\tau_{2,slow}$	0.5154	[-]

Table 4.2: Flux parameters used during the code verification

4.3.1 Steady-state verification

Case 1: PFG off and valve closed

In the case where the PFG and the valve stay closed, the first equation of the system 4.1 becomes

$$\frac{d}{dt}(p_{c1}) = \frac{kT_{c1}}{V_1} \left(\dot{N}_{1,leak} - \dot{N}_{P1}(p_{c1}) \right).$$

At the steady state $\frac{d}{dt}(p_{c1}) = 0$, the turbopump flux \dot{N}_{P1} and the leak flux $\dot{N}_{1,leak}$ respect the relation

$$\dot{N}_{P1}(p_{c1}) = \dot{N}_{1,leak}.$$

According to [28], the main chamber pressure and the turbopump gas flow are linked by

$$P_{c1} = \frac{Q_{P1}}{S_1}, \quad (4.3)$$

with P_{c1} the main chamber pressure in [mbar], S_1 is the turbopump pumping speed of the main chamber in [L/s] and Q_{P1} is the turbopump gas flow in [mbar.L/s]. Note p_{c1} and P_{c1} represent the same parameter. But the first one is expressed in [Pa], whereas the other is in [mbar]. By playing with the units of different parameters

$$k = \frac{R}{Na} \equiv \left[\frac{\text{m}^3 \text{ Pa}}{\text{particle K}} \right] \equiv \frac{1}{10} \left[\frac{\text{L.mbar}}{\text{particle K}} \right],$$

it is possible to convert a particle flow into a gas flow in [mbar.L/s]

$$Q = 10\dot{N}kT \equiv \left[\frac{\text{particle}}{\text{s}} \right] \left[\frac{\text{L.mbar}}{\text{particle.K}} \right] [K] \equiv \left[\frac{\text{mbar.L}}{\text{s}} \right]. \quad (4.4)$$

Finally, Equations 4.3 and 4.4 provide

$$P_{c1} = \frac{10\dot{N}_{P1}kT_{c1}}{S_1} = 10\frac{\dot{N}_{1,leak}kT_{c1}}{S_1} = \frac{Q_{1,leak}}{S_1}, \quad (4.5)$$

where $Q_{1,leak}$ is the leak flux of the main chamber expressed in [mbar.L/s].

Using the data listed in the previous tables, the theoretical value is estimated at $P_{c1} = 3.4483 \times 10^{-8}$ mbar. The model providing the very similar value of $P_{c1} = 3.4483 \times 10^{-8}$ mbar because the relative difference is about $6.98 \times 10^{-6}\%$.

Case 2: PFG on and valve closed

When the PFG is turned on and the valve is closed, the first relation of Equations 4.1 is simplified

$$\frac{d}{dt}(p_{c1}) = \frac{kT_{c1}}{V_1} \left(\dot{N}_{PFG} + \dot{N}_{1,leak} - \dot{N}_{P1}(p_{c1}) \right).$$

At the steady state, the equilibrium pressure is the solution of

$$\dot{N}_{P1}(p_{c1}) = \dot{N}_{PFG} + \dot{N}_{1,leak}.$$

As previously, equations 4.3 and 4.4 give

$$P_{c1} = \frac{10\dot{N}_{P1}kT_{c1}}{S_1} = \frac{10(\dot{N}_{PFG} + \dot{N}_{1,leak})kT_{c1}}{S_1} = \frac{Q_{PFG} + Q_{1,leak}}{S_1}, \quad (4.6)$$

white Q_{PFG} and $Q_{1,leak}$ the PFG flux and the leak flux expressed in [mbar.L/s].

The theoretical pressure is therefore $P_{c1} = 1.9222 \times 10^{-5}$ mbar. The simulation provides a pressure of $P_{c1} = 1.9226 \times 10^{-5}$ mbar. And the relative error stays acceptable, because it is equal to 0.024%.

Case 3: PFG off and valve open

In the case where the PFG is turned off and the valve is open, the system 4.1 at the steady-state becomes

$$0 = \dot{N}_{2,slow}(p_{c2}) + \dot{N}_{1,leak} - \dot{N}_{P1}(p_{c1}) - \dot{N}_{1,slow}(p_{c1}), \quad (4.7)$$

$$0 = \dot{N}_{1,slow}(p_{c1}) + \dot{N}_{2,leak} - \dot{N}_{P2}(p_{c2}) - \dot{N}_{2,slow}(p_{c2}). \quad (4.8)$$

The sum 4.7 + 4.8 provides

$$\dot{N}_{P1}(p_{c1}) + \dot{N}_{P2}(p_{c2}) = \dot{N}_{1,leak} + \dot{N}_{2,leak}. \quad (4.9)$$

And the subtraction 4.7 - 4.8 gives

$$\dot{N}_{P1}(p_{c1}) - \dot{N}_{P2}(p_{c2}) = 2\dot{N}_{2,slow}(p_{c2}) - 2\dot{N}_{1,slow}(p_{c1}) + \dot{N}_{1,leak} - \dot{N}_{2,leak}. \quad (4.10)$$

To remind the thermal flow of the chamber i is given by

$$\dot{N}_{i,slow} = p_{ci}A_i\tau_{i,slow}\sqrt{\frac{1}{2\pi mkT_{ci}}} \quad \text{with } i = 1 \text{ or } 2,$$

where $\dot{N}_{i,slow}$ in [particle/s] and p_{ci} in [Pa].

By using the relation 4.4, this flux can be expressed in [mbar.L/s]

$$Q_{i,slow} = 10\dot{N}_{i,slow}kT_{ci} = 10kT_{ci} \times p_{ci}A_i\tau_{i,slow}\sqrt{\frac{1}{2\pi mkT_{ci}}} \quad \text{with } i = 1 \text{ or } 2.$$

To lighten the notations, ξ_i is introduced as

$$Q_{i,slow} = P_{ci}\xi_i \quad \text{with } i = 1 \text{ or } 2, \quad (4.11)$$

where $P_{ci} = \frac{p_{ci}}{100}$ is the pressure of the chamber i in [mbar].

This new symbol corresponds to the slow flux expression divided by the corresponding chamber pressure in [mbar]. It is equal to

$$\xi_i = 10kT_{ci}\frac{p_{ci}}{P_{ci}}A_i\tau_{i,slow}\sqrt{\frac{1}{2\pi mkT_{ci}}} = 1000A_i\tau_{i,slow}\sqrt{\frac{kT_{ci}}{2\pi m}}.$$

Thus, the equations 4.9 and 4.10 form a system of two equations with two unknowns P_{c1} and P_{c2} .

$$\begin{aligned} Q_{P1} + Q_{P2} &= Q_{1,leak} + Q_{2,leak}, \\ Q_{P1} - Q_{P2} &= 2Q_{2,slow} - 2Q_{1,slow} + Q_{1,leak} - Q_{2,leak}. \end{aligned}$$

Considering 4.3, 4.4 and 4.11, it can be replaced by

$$S_1 P_{c1} + S_2 P_{c2} = Q_{1,leak} + Q_{2,leak}, \quad (4.12)$$

$$S_1 P_{c1} - S_2 P_{c2} = 2P_{c2}\xi_2 - 2P_{c1}\xi_1 + Q_{1,leak} - Q_{2,leak}. \quad (4.13)$$

The first equation of this system provides

$$P_{c1} = \frac{1}{S_1}(Q_{1,leak} + Q_{2,leak} - S_2 P_{c2}).$$

And the second one becomes

$$\begin{aligned} Q_{1,leak} + Q_{2,leak} - S_2 P_{c2} - S_2 P_{c2} &= 2P_{c2}\xi_2 - \frac{2\xi_1}{S_1}(Q_{1,leak} + Q_{2,leak} - S_2 P_{c2}) + Q_{1,leak} - Q_{2,leak} \\ 2Q_{2,leak} - 2S_2 P_{c2} &= 2P_{c2}\xi_2 - \frac{2\xi_1}{S_1}(Q_{1,leak} + Q_{2,leak} - S_2 P_{c2}) \\ Q_{2,leak} + \frac{\xi_1}{S_1}(Q_{1,leak} + Q_{2,leak}) &= P_{c2}\xi_2 + \frac{\xi_1}{S_1}S_2 P_{c2} + S_2 P_{c2} \end{aligned}$$

Finally, the pressure expressions are

$$\begin{aligned} P_{c1} &= \frac{1}{S_1}(Q_{1,leak} + Q_{2,leak} - S_2 P_{c2}), \\ P_{c2} &= \frac{Q_{2,leak} + \frac{\xi_1}{S_1}(Q_{1,leak} + Q_{2,leak})}{\xi_2 + \frac{\xi_1}{S_1}S_2 + S_2}. \end{aligned}$$

Again the two tables at the beginning of this section allow us to obtain $P_{c1} = 3.4878 \times 10^{-8}$ mbar and $P_{c2} = 4.9426 \times 10^{-8}$ mbar as a theoretical value. The model obtains the values $P_{c1} = 3.4878 \times 10^{-8}$ mbar and $P_{c2} = 4.9426 \times 10^{-8}$ mbar. And the relative errors are $3.6 \times 10^{-6}\%$ and $4.1 \times 10^{-7}\%$ for the main chamber and the secondary chamber respectively.

Case 4: PFG on and valve open

Finally, when the PFG is turned on and the valve is open, the system 4.1 at steady-state becomes

$$\begin{aligned} 0 &= \dot{N}_{PFG} + \dot{N}_{2,slow}(p_{c2}) + \dot{N}_{1,leak} - \dot{N}_{P1}(p_{c1}) - \dot{N}_{1,fast} - \dot{N}_{1,slow}(p_{c1}), \\ 0 &= \dot{N}_{1,fast} + \dot{N}_{1,slow}(p_{c1}) + \dot{N}_{2,leak} - \dot{N}_{P2}(p_{c2}) - \dot{N}_{2,slow}(p_{c2}). \end{aligned}$$

The sum of these two relations is

$$\dot{N}_{P1}(p_{c1}) + \dot{N}_{P2}(p_{c2}) = \dot{N}_{PFG} + \dot{N}_{1,leak} + \dot{N}_{2,leak}.$$

And their subtraction is

$$\dot{N}_{P_1}(p_{c1}) - \dot{N}_{P_2}(p_{c2}) = \dot{N}_{PFG} + 2\dot{N}_{2,slow}(p_{c2}) - 2\dot{N}_{1,slow}(p_{c1}) - 2\dot{N}_{1,fast}(p_{c1}) + \dot{N}_{1,leak} - \dot{N}_{2,leak}.$$

As for the third case, they form a new system allowing to find P_{c1} and P_{c2} . If the different flux are converted into [mbar.L/s], these equations become

$$\begin{aligned} Q_{P_1} + Q_{P_2} &= Q_{PFG} + Q_{1,leak} + Q_{2,leak}, \\ Q_{P_1} - Q_{P_2} &= Q_{PFG} + 2Q_{2,slow} - 2Q_{1,slow} - 2Q_{1,fast} + Q_{1,leak} - Q_{2,leak}. \end{aligned}$$

As $\dot{N}_{1,fast} = f_{ion}\dot{N}_{PFG}\eta_m\tau_{1,fast}$, the corresponding gas flow is given by

$$Q_{1,fast} = f_{ion}Q_{PFG}\eta_m\tau_{1,fast}. \quad (4.14)$$

By using 4.14, 4.3 and 4.11 in the system, it is replaced by

$$\begin{aligned} S_1P_{c1} + S_2P_{c2} &= Q_{PFG} + Q_{1,leak} + Q_{2,leak}, \\ S_1P_{c1} - S_2P_{c2} &= Q_{PFG} + 2P_{c2}\xi_2 - 2P_{c1}\xi_1 - 2f_{ion}Q_{PFG}\eta_m\tau_{1,fast} + Q_{1,leak} - Q_{2,leak}. \end{aligned}$$

The main chamber pressure is therefore

$$P_{c1} = \frac{1}{S_1}(Q_{PFG} + Q_{1,leak} + Q_{2,leak} - S_2P_{c2}).$$

And the second chamber pressure P_{c2} is solution of

$$\begin{aligned} Q_{PFG} + Q_{1,leak} + Q_{2,leak} - 2S_2P_{c2} &= Q_{PFG} + 2P_{c2}\xi_2 - \frac{2\xi_1}{S_1}(Q_{PFG} + Q_{1,leak} + Q_{2,leak} - S_2P_{c2}) \\ &\quad - 2f_{ion}Q_{PFG}\eta_m\tau_{1,fast} + Q_{1,leak} - Q_{2,leak} \end{aligned}$$

By removing terms present at both sides, it becomes

$$\begin{aligned} 2Q_{2,leak} - 2S_2P_{c2} &= 2P_{c2}\xi_2 - \frac{2\xi_1}{S_1}(Q_{PFG} + Q_{1,leak} + Q_{2,leak} - S_2P_{c2}) - 2f_{ion}Q_{PFG}\eta_m\tau_{1,fast}, \\ Q_{2,leak} - S_2P_{c2} &= P_{c2}\xi_2 - \frac{\xi_1}{S_1}(Q_{PFG} + Q_{1,leak} + Q_{2,leak} - S_2P_{c2}) - f_{ion}Q_{PFG}\eta_m\tau_{1,fast}. \end{aligned}$$

The P_{c2} is isolated and an expression for both pressure is found

$$\begin{aligned} P_{c1} &= \frac{1}{S_1}(Q_{PFG} + Q_{1,leak} + Q_{2,leak} - S_2P_{c2}), \\ P_{c2} &= \frac{Q_{2,leak} + \frac{\xi_1}{S_1}(Q_{1,leak} + Q_{2,leak}) + Q_{PFG}(f_{ion}\eta_m\tau_{1,fast} + \frac{\xi_1}{S_1})}{\xi_2 + \frac{\xi_1}{S_1}S_2 + S_2}. \end{aligned}$$

Therefore, in the most general case, the theoretical steady-state pressure are $P_{c1} = 1.8832 \times 10^{-5}$ mbar and $P_{c2} = 6.1496 \times 10^{-7}$ mbar. The model gives the values $P_{c1} = 1.8836 \times 10^{-5}$ mbar and $P_{c2} = 6.1505 \times 10^{-7}$ mbar. Finally the relative difference are 0.022% and 0.015% .

4.3.2 Temporal verification

To complete the model verification, it is required to test the temporal evolution of the pressures. For that, the pressure evolution given by the model is compared to the curve of the theoretical pressure function. In this section, only the case where the PFG and the valve remain closed is analyzed.

In this case, the first equation of the system 4.1 becomes

$$\frac{d}{dt}(p_{c1}) = \frac{kT_{c1}}{V_1} \left(\dot{N}_{1,leak} - \dot{N}_{P1}(p_{c1}) \right).$$

Knowing that $\dot{N}_{1,leak}$ is constant and $\dot{N}_{P1}(p_{c1}) = \frac{S_1 p_{c1}}{kT_{c1}}$, a first order differential equation is obtained

$$\frac{V_1}{kT_{c1}} \frac{dp_{c1}}{dt} = \dot{N}_{1,leak} - \frac{S_1 p_{c1}}{kT_{c1}}. \quad (4.15)$$

The only unknown is p_{c1} and its expression is the sum of the homogeneous solution and a particular solution.

Homogeneous solution

By considering the homogeneous equation

$$\begin{aligned} \frac{V_1}{kT_{c1}} \frac{dp_{c1}}{dt} &= -\frac{S_1}{kT_{c1}} p_{c1} \\ \frac{dp_{c1}}{p_{c1}} &= -\frac{S_1}{V_1} dt \\ \ln(p_{c1,h}) &= -\frac{S_1}{V_1} t + c \end{aligned}$$

The homogeneous solution is given by

$$p_{c1,h}(t) = C e^{-\frac{S_1}{V_1} t}, \quad (4.16)$$

where C is an integration constant.

Particular solution

The relation 4.15 allows to impose the particular solution

$$p_{c1,p}(t) = p_{c1,p} = \dot{N}_{1,leak} \frac{kT_{c1}}{S_1}. \quad (4.17)$$

Because it satisfies the equation

$$\begin{aligned} \frac{V_1}{kT_{c1}} \frac{d}{dt}(p_{c1,p}) - \frac{S_1}{kT_{c1}} p_{c1,p} &= \frac{V_1}{kT_{c1}} \cdot 0 - \frac{S_1}{kT_{c1}} \left(\dot{N}_{1,leak} \frac{kT_{c1}}{S_1} \right) \\ &= \dot{N}_{1,leak} \end{aligned}$$

Final solution

Thanks to 4.16 and 4.17, the global solution of the equation 4.15 is given by

$$p_{c1}(t) = p_{c1,h}(t) + p_{c1,p} = C e^{\frac{-S_1}{V_1}t} + \dot{N}_{1,leak} \frac{kT_{c1}}{S_1}.$$

To find the integration constant C the boundary conditions must be used. The initial pressure $p_{c1,0}$ in [Pa] belonging to the nominal conditions, the relation at $t = 0$ is

$$p_{c1}(t = 0) = C + \dot{N}_{1,leak} \frac{kT_{c1}}{S_1} = p_{c1,0}.$$

And the constant is equals to

$$C = p_{c1,0} - \dot{N}_{1,leak} \frac{kT_{c1}}{S_1}.$$

But as the final pressure corresponds to the equilibrium state pressure of the first case, the equation at $t = \infty$ is

$$p_{c1}(t = \infty) = C \cdot 0 + \dot{N}_{1,leak} \frac{kT_{c1}}{S_1} = p_{c1,f},$$

with $p_{c1,f}$ the final pressure of the main chamber in [Pa]. The constant can be written in the form

$$p_{c1,f} = \dot{N}_{1,leak} \frac{kT_{c1}}{S_1} \quad \Rightarrow \quad C = p_{c1,0} - p_{c1,f}.$$

Finally the pressure in function of time can be expressed as

$$p = (p_{c1,0} - p_{c1,f}) e^{-\frac{t}{\kappa}} + p_{c1,f},$$

where t is the time in [s], $\kappa = \frac{V_1}{S_1}$ is the time constant and S_1 the turbopump pumping speed considered as constant.

The imposition of a constant pumping speed can induce a shift compared to the model if the initial pressure is not sufficiently low. Indeed the pumping speed is not constant above a certain pressure and the dependency on this parameter is strong. On 4.9, the turbopump is turned on when the main chamber pressure is about 0.1 [mbar]. The initial pumping speed of the model is about 803 [L/s] which is much lower than the final value about 2900 [L/s]. Thus the pressure of the model will decrease less quickly than the theoretical pressure formula.

But if a smaller initial pressure considered, the pumping speed of the turbopump remains almost constant. As shown on the figure 4.10, the two pressure evolution of the model and the theory are very similar.

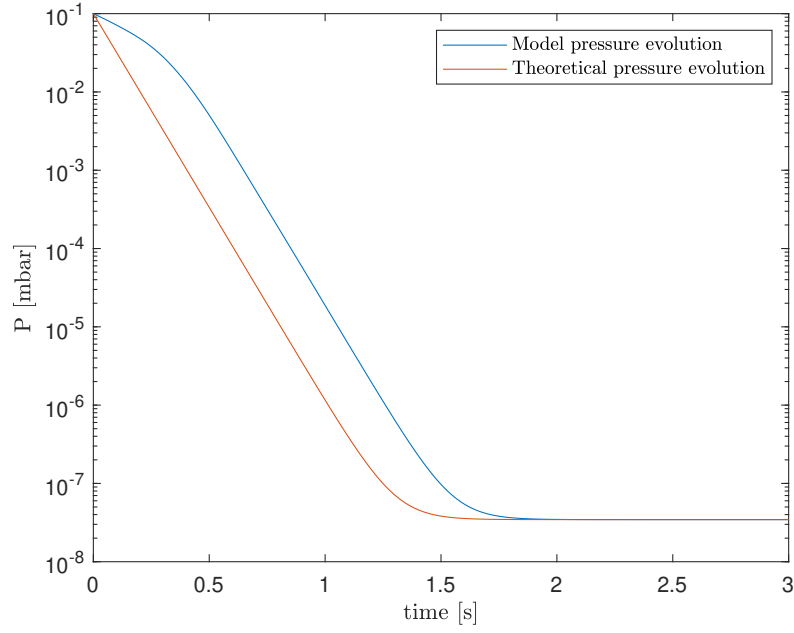


Figure 4.9: Comparison of the pressure evolution between the theory and the model with an initial pressure of 0.1 mbar

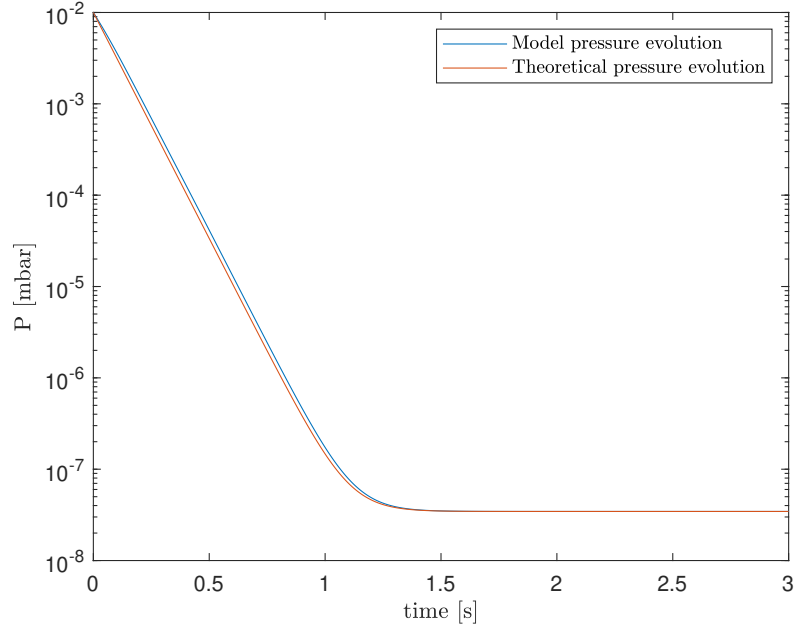


Figure 4.10: Comparison of the pressure evolution between the theory and the model with an initial pressure of 0.01 mbar

4.4 Conclusion

This chapter describes a 0-D model capable of calculating the change in pressure in the installation over time. It is based on the theory introduced in Chapters 2 and 3. Using it, we have obtained a theoretical expression for each particle flow circulating inside the chambers and determine the parameters influencing these flows. Based

on the continuity equation, these expressions form system of equations having both chamber pressures as the only unknowns.

Moreover, the implementation of the 0-D model is verified by comparison with analytical solutions of four different cases. These include the computation of steady state pressures of different facility configurations. The agreement between the analytical and numerical solutions is found to be very satisfactory. Finally, the transient behavior of the model is verified by comparison with a simplified case with constant coefficients for which an analytical solution is found. Both solutions agree. The verification results give us confidence in the correct implementation of the model and in its application as an analysis tool in the following chapters.

Chapter 5

Test scenarios

One of the facility's objectives is to determine the transmissivity of a device placed between its two chambers. More precisely, it consists of measuring the transmission probability of particles of the fast flux passing through models of particular geometries. As it is not possible to directly measure this parameter, it is obtained through other quantities which are measured through different probes or dedicated tests. This chapter consists of two sections: the first one deals with the measurable parameters and the sensors and probes used to provide them. The following deals with parameters not measured by probes. For each parameter, this section describes the corresponding test scenario and provides the analytical reasoning to find the parameter from the test. Moreover, each part provides the parameter expected numerical value verifying the scenario and expressions used.

5.1 Measurable parameters and probes

To know the parameters to be determined, it is convenient to start from the pressure expression at the steady-state. These relations contain all the parameters influencing the final installation state. In the most general case (which corresponds to the fourth verification case, Section 4.3), these expressions are

$$P_{c1} = \frac{1}{S_1}(Q_{PFG} + Q_{1,leak} + Q_{2,leak} - S_2 P_{c2}),$$

$$P_{c2} = \frac{Q_{2,leak} + \frac{\xi_1}{S_1}(Q_{1,leak} + Q_{2,leak}) + Q_{PFG}(f_{ion}\eta_m\tau_{1,fast} + \frac{\xi_1}{S_1})}{\xi_2 + \frac{\xi_1}{S_1}S_2 + S_2},$$

where ξ_i is a function of A_i , $\tau_{i,slow}$, T_{ci} and m

$$\xi_i = 1000A_i\tau_{i,slow}\sqrt{\frac{kT_{ci}}{2\pi m}}.$$

The mass utilization η_m and the ion fraction f_{ion} reaching the valve inlet are not easily measured. But there are some probes able to give the fast particle flux at the duct inlet: $Q_{1,fast}$. In this chapter, the following expressions are used instead

$$P_{c1} = \frac{1}{S_1}(Q_{PFG} + Q_{1,leak} + Q_{2,leak} - S_2 P_{c2}), \quad (5.1)$$

$$P_{c2} = \frac{Q_{2,leak} + \frac{\xi_1}{S_1}(Q_{1,leak} + Q_{2,leak} + Q_{PFG}) + \tau_{1,fast}Q_{1,fast}}{\xi_2 + \frac{\xi_1}{S_1}S_2 + S_2}, \quad (5.2)$$

where the product $f_{ion}\eta_m Q_{PFG}$ is replaced by $Q_{1,fast}$.

Among all parameters present in 5.1 and 5.2, some quantities are assumed to be known:

- k the Boltzmann constant [J/K]
- A_1 and A_2 the duct cross-sections at the main chamber side and at the secondary chamber side [m²]
- m the mass of one gas particle [kg]

Note that all the dimensions influencing the installation operation are assumed to be known. The vessel volumes V_1 and V_2 are therefore also known. All other parameters must be determined. Among them:

- P_{c1} and P_{c2} the pressures of both chambers in [mbar]
- S_1 and S_2 the effective pumping speed of both turbopumps in [L/s]
- Q_{PFG} the total PFG flux in [mbar .L/s]
- $Q_{1,leak}$ and $Q_{2,leak}$ the leak flux in both chambers in [mbar.L/s]
- $Q_{1,fast}$ the fast ion flux emitted by the PFG, reaching the duct inlet in [mbar.L/s]
- T_{c1} and T_{c2} the temperature of both chambers in [K]

As the PFG is equipped with a mass flow controller, the PFG flux (Q_{PFG}) is the only parameter directly provided by a facility device. The remaining quantities must either be measured by probes or be estimated by different detection methods. To select a probe or method, various constraints must be considered. There are the cost of the sensor, the time, the available space, and so on. Ideally a device or test should be easily adaptable to the installation, not too expensive and provides sufficiently accurate results.

Temperature measurements

There are two types of probes to measure the temperature of the chamber's walls, for which expected range is around room temperature: the Resistance Thermometers (RTD) and the thermocouples.

According to [12], the former uses a precise sensing resistor, generally made of platinum. Its use is based on the physical property that a metal resistance changes with temperature. In practice, an electric current passes through a piece of metal and allows measuring its resistance. Knowing the resistance characteristics of the RTD element, the measured resistance provides the temperature.

The second type is the thermocouple. This is composed of two wires of different metal alloys connected at one end. When the metal junction is heated or cooled, a voltage difference is produced and which can be converted to a temperature reading.

As explained in [6], thermocouples can withstand a large temperature range and are less expensive. Resistance Thermometers are more precise, more stable but also less affordable.

In the VKI facility, the temperature is not supposed to vary greatly. However, a high uncertainty on the temperature measurements deteriorates the transmission

probabilities estimation. In this analysis, we will consider that the installation is equipped with two Resistance Thermometers to provide the temperatures T_{c1} and T_{c2} .

Pressure measurements

The Pfeiffer vacuum company supplies a large part of facility components such as turbopumps, vacuum chambers, etc. This company was chosen not only for its deemed reliability for vacuum technology but also because choosing components from the same manufacturer facilitates assembly. The pressure probes are therefore also supplied by the company Pfeiffer vacuum.

It supplies four different pressure detector series: the DigiLine serie, the Active-Line serie, the CenterLine serie, and the ModulLine serie. The choice depends on different factors such as:

- Pressure range,
- Gas composition,
- Accuracy and repeatability,
- Plasma condition (ionization degree),
- Available space for installation,
- Compatibility with the probe controller,
- Cost,
- Installation complexity.

Considering the installation, each chamber must have a probe to measure P_{c1} and P_{c2} respectively. The pressure can range from 0.1 mbar down to 10^{-9} mbar, they must cover this entire range. As the turbopump controllers are sourced by Pfeiffer, an adaptable model for other manufacturer controllers is not required. Therefore, a PKR pressure probe of the ActiveLine is chosen(see [29]). Its uncertainty has a component associated to the reading and one associated to the full scale value.

Fast flux measurements

There are different probes capable of measuring the flux of fast particles impinging on their surface, but two of them stand out. These probes are affordable, easily adaptable to the installation, and provide good results. These are the Faraday Probe and the RPA (Retarding Potential Analyzer) probe.

In its most simple configuration, the Faraday Probe consists of a conductive surface immersed in an ion beam as depicted in Figure 5.1. The colliding ions capture electrons from the conductive sensor surface and return to a neutral state. This interaction generates a probe current which is a good approximation of the ion flux. However, the electrons contained in the ionic plume can influence the collected current as well. As they are collected by the conductive sensor. Therefore, the current drawn by the collector is not only a consequence of the ion interaction with the surface but also of the electron-surface. When electrons reach the collector, there

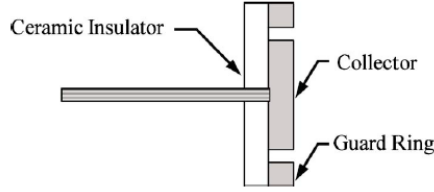


Figure 5.1: Diagram representing a Faraday probe. A collecting conducting surface surrounded by a guard ring is attached on a ceramic insulator which prevents ions going in the opposite direction from touching the probe (from [9])

are more electrons on the sensor, and the net current is diminished. Therefore, the estimated ion flux may be lower than the real one. The collector surface is therefore slightly negatively charged to repel electrons.

Another source of error is Charge EXchange (CEX) process. It occurs when a fast ion exchanges charge with a neutral, creating a slow ion and a fast neutral. This interaction creates ions in the background gas which are also detected by the probe. The probe is not able to discern these ions from the fast flux and must be calibrated. Calibration with regards to CEX effects has been performed in the literature (see document [7]) by measuring the current ions of four ion beams with different amounts of CEX ions production. As the exchange of charge is favored at higher background pressures, it is good practice to measure the ion current of the plasma at four different background pressures to correctly estimate the CEX effect on the drawn current. According the authors of the same document, the maximum background pressure is typically less than 5.0×10^{-5} Torr-Xe, and one of these pressures must be the lowest achievable facility pressure during thruster operation. To respect these conditions in the case of argon, the pressure stays in a range between 10^{-5} and 4×10^{-5} mbar.

The more complex RPA probe consists of a collector surface with differently biased grids in front (see Figure 5.2). As in the previous probe, this detector suppresses the electrons' effect. The first grid is polarised negatively to repel electrons traveling with an ion beam. Unlike the Faraday probe, it can select the minimum energy of the detected ions. This is because the second grid is biased to a varying positive voltage U . Only ions (charge q) with kinetic energy higher than qU , pass through the grid and collide with the collecting surface. Finally, the secondary electron emission from the other grid can also falsify the measurement. Another negatively biased grid is part of the assembly to suppress the impact of these electrons. This sensor does not only measure the flux, but it measures the ion energy distribution in the plasma beam. As seen in Chapter 2, knowing the distribution provides additional information such as: the ion flux, the CEX ion contribution, the speed ratio, etc. The probe does not need pressure calibration to estimate CEX effects, but it is more complex and expensive, and it is not easy to find its uncertainty. Therefore, the installation will initially use a Faraday probe.

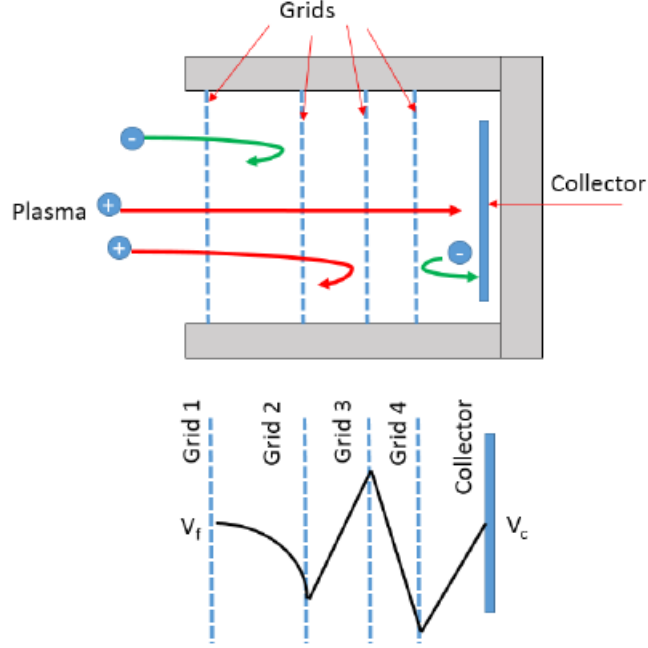


Figure 5.2: Schematic of an RPA probe. Four grids are arranged in front of a collector plate. The four grids are biased to different potentials in order to repel electrons and filter incoming ions from the gas plume.

5.2 Measurement procedure

In addition to the measurable parameters, some parameters are determined based on tests. These are the leakage rates $Q_{1,leak}$ and $Q_{2,leak}$, pumping speeds S_1 and S_2 , flux of fast ions reaching the duct $Q_{1,fast}$, and the transmission probabilities $\tau_{1,slow}$, $\tau_{2,slow}$, and $\tau_{1,fast}$. This section discusses the scenarios for each of these tests. For clarity, each test starts from the same initial situation:

- initial pressure of the two chambers is 0.1 mbar
- open valve
- turbopumps operating at their maximum speed
- PFG off

The tests are presented in the order which they should be performed. The 0-D model developed in Chapter 4 allows to visualize the behavior of the installation during the tests. It allows assessing the feasibility of the tests and provides the expected results.

5.2.1 Main chamber leak flux

Measurement test

Two methods can determine the leak rate $Q_{1,leak}$.

The first method measures the ultimate pressure when only the leak flux and the turbopump flux are present. The valve between the two chambers is closed. Thanks

to these measurements and the steady-state pressure relations, it is possible to find the leak rates.

In reality, this method has two flaws. First, the leakage rate is assumed constant. As explained in Section 3.1, this is not always the case. The flow can be considered constant after a while. This test cannot determine when the leak rate becomes constant and may provide incorrect results. Then, the pumping speed of the first turbopump S_1 is not yet known. As it depends on the leak rate, it must be determined after $Q_{1,leak}$. Therefore, this test requires an estimate of this speed, which causes some errors in the result.

The second method is the pressure rise test. This method is also easy to set up but takes more time. For this test, the chamber must have only one incoming flow: the leak flux. Therefore, the valve is closed, and the turbopump stopped. It is possible in the case of the VKI facility because each turbopump is independent and can be stopped by a controller device. Moreover, the installation includes valves downstream of each turbopump. They prevent some external components from returning to the chamber when the turbopump stops. When the leak flux enters the chamber, the pressure increases. By measuring the pressure increase rate, it is possible to determine the leak rate. This method is a good alternative because it only needs time and pressure measurements. And the fact of following the pressure evolution during a time interval makes it possible to determine when this flow becomes constant. Therefore, the first leak rate is determined through pressure rise test.

We note that a mass spectrometer is the most accurate and widely used equipment for leak detection in an installation. But this equipment being expensive, it will only be considered if the uncertainties of the leak rate have a significant impact.

Test scenario To determine the leak rate from the main chamber a series of steps must be followed. Except in cases where the configuration does not allow it, the installation must reach a steady state before starting the next step. At the beginning of this test and all the other, the chamber pressure has already reached 0.1 mbar thanks to the backing pump, the valve is open and the PFG is turned off.

- **Step 1:** The turbopumps switch on and reduce the chamber pressures.
- **Step 2:** When the pressures stabilize, the valve between both chambers is closed.
- **Step 3:** The turbopump of the first chamber is stopped and its downstream valve is closed. The main vessel is isolated from the rest of the installation.
- **Step 4:** The pressure sensor follows the evolution of the main chamber pressure. While the pressure increases is not stable, the leak flow is not constant.
- **Step 5:** When the pressure slope becomes constant, the stopwatch starts and provides the required time for the chamber to reach a threshold pressure. As the chamber has an incoming flux (the leak flow) but no outgoing flux, it cannot reach a steady-state, and the pressure can only increase.
- **Step 6:** Finally, the turbopump is on again, and the downstream valve is open. The main chamber regains its ultimate pressure.

The evolution of both chamber pressures during this procedure is given by Figure 5.3. Each curve corresponds to the pressure of one chamber. The crosses represent the intermediate situations between each step. The exact pressure and time values at these points are given in Table 5.1. Note that the model considers that the leakage rate is always constant. The pressure slope is already constant at the instant (2). Thus the fourth step does not appear. In the simulation, the turbopump is turned on again when the pressure reaches 1×10^{-5} mbar.

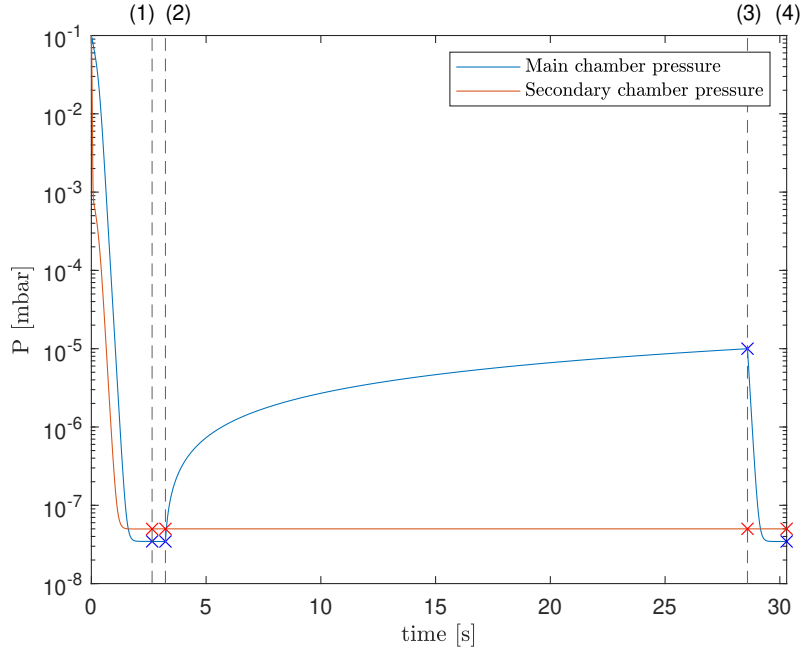


Figure 5.3: Pressures evolution in both chamber during the first test

Situations	Time [s]	Main Chamber Pressure [mbar]	Secondary Chamber Pressure [mbar]
(1)	2.6288	3.4879×10^{-8}	4.9426×10^{-8}
(2)	3.3586	3.4483×10^{-8}	5.000×10^{-8}
(3)	28.7240	1.0002×10^{-5}	5.000×10^{-8}
(4)	30.4302	3.4483×10^{-8}	5.000×10^{-8}

Table 5.1: Pressures and times of the intermediate situations of the first test

Notice that, if the vertical scale was linear, the pressure would rise line would have a slope $\frac{Q_{1,leak}}{V_1}$. However, in Figure 5.3, the y-scale is logarithmic. The pressure increase follows the logarithmic curve $\log \left(P_{c1,2} + \frac{Q_{1,leak}}{V_1} t \right)$, with $P_{c1,2}$ the main chamber pressure at the situation (2).

Conversely, the turbopump of the second chamber does not stop, and the pressure P_{c2} remains constant.

Analytical reasoning

According to [10], the pressure rise test method determines the leak rates of the chamber i by the relation

$$Q_{i,leak} = \frac{V_{i,l}\Delta P_{ci}}{\Delta t_i} \quad i = 1 \text{ or } 2, \quad (5.3)$$

where $Q_{i,leak}$ is the corresponding leak flux in [mbar.L/s], $V_{i,l}$ the chamber volume in [L], ΔP_{ci} is the pressure difference measurements in the chamber in [mbar], and Δt_i the time in [s] for the vessel to reach the threshold pressure. Knowing the volume ($\pi \times 0.3^2 \times 0.9 = 0.081\pi \text{ m}^3 = 81\pi \text{ L}$) and the data in Table 5.1, the leak rate of the first chamber is given by

$$Q_{1,leak} = \frac{81\pi(1.0002 \times 10^{-5} - 3.4483 \times 10^{-8})}{(28.7240 - 3.3586)} = 1.00 \times 10^{-4} \text{ mbar.L/s.}$$

This result is exactly equal to the leakage rate imposed as nominal condition. It verifies that the method employed is correct, and that the model recovers the theoretical result.

5.2.2 Secondary chamber leak flux

Measurement test

For the same reasons as the leak rate $Q_{1,leak}$, the test determining $Q_{2,leak}$ is also a pressure rise test. But now it is the second turbopump that must stop to allow the pressure to increase.

Test scenario The initial situation is the same for all the tests. The chambers have an initial pressure of 0.1 mbar, the valve is open, and the PFG is off. Before each new step, a steady state must be reached. The steps to follow are:

- **Step 1:** The turbopumps switches on and pump the gas into both vessels.
- **Step 2:** The valve separating the two chambers is closed.
- **Step 3:** Now, the turbopump of the second chamber is stopped, and the corresponding downstream valve is also closed.
- **Step 4:** The pressure sensor follows the secondary chamber pressure evolution. When its slope becomes constant, the leak rate is constant and the pressure rise test can start.
- **Step 5:** A stopwatch measures the time for the chamber pressure to reach a threshold value.
- **Step 6:** Finally, the turbopump regains its initial configuration. The chamber pressure drops to the ultimate pressure.

The evolution of the pressure during this test is described by Figure 5.4. Again, the model assumes that the leak rate is constant. So the fourth stage of the scenario does not appear in this graph. The limit pressure is also 1×10^{-5} mbar.

In the nominal conditions in Tables 4.1, both chambers have the same leak rate: $Q_{1,leak} = Q_{2,leak} = 1 \times 10^{-4}$ mbar.L/s. Since the secondary vessel is much smaller than the first, the test is much faster. The exact values in time and pressures are listed in Table 5.2.

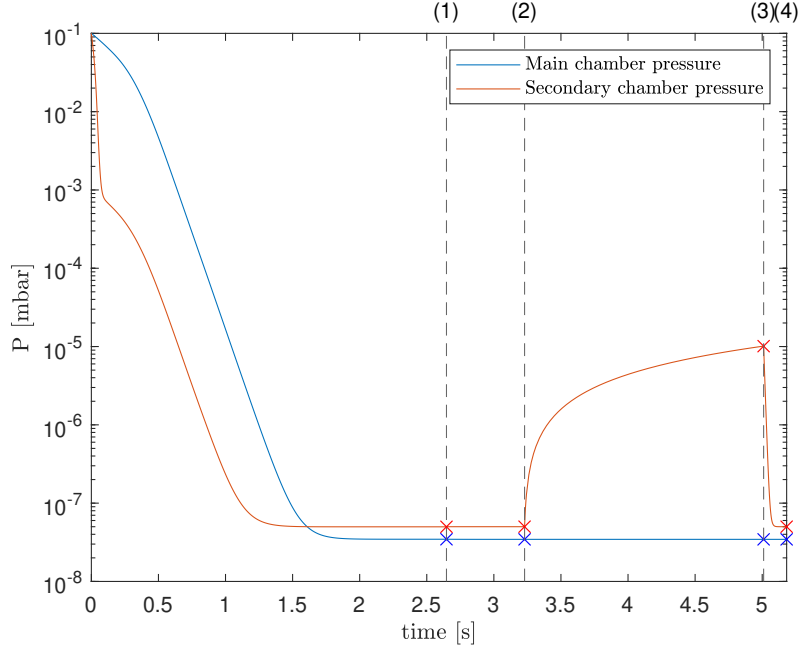


Figure 5.4: Pressures evolution in both chamber during the second test

Situations	Time [s]	Main Chamber Pressure [mbar]	Secondary Chamber Pressure [mbar]
(1)	2.6288	3.4879×10^{-8}	4.946×10^{-8}
(2)	3.3586	3.4483×10^{-8}	5.000×10^{-8}
(3)	5.1229	3.4483×10^{-8}	1.0034×10^{-5}
(4)	5.2968	3.4483×10^{-8}	5.000×10^{-8}

Table 5.2: Pressures and times of the intermediate situations of the second test

As for the previous test, the ordinate scale is logarithmic, and so is the evolution of P_{c2} is also.

Analytical reasoning

As for $Q_{1,leak}$, the expression 5.3 gives the leak rate from the measurements made during the test. The volume of the second vessel is $\pi \times 0.15^2 \times 0.25 = 0.0056\pi$ m³ = 5.6 π L. Based on the data in Table 5.2, the second leak flow is

$$Q_{2,leak} = \frac{5.6\pi(1.0034 \times 10^{-5} - 5.000 \times 10^{-8})}{(5.1229 - 3.3586)} = 1.00 \times 10^{-4} \text{ mbar.L/s.}$$

Once again, this result verifies the correct implementation of the 0-D model.

5.2.3 First turbopump pumping speed

Now that the leakage rates are known, it is possible to estimate the pumping speeds of the turbopumps.

Measurement test

There are two possible scenarios: either the previously determined leak rate is used to measure the pumping speed, by measuring the ultimate pressure in the chambers, or a known mass flow rate is injected using the PFG and the resulting steady state pressure is used to determine the pumping speed.

The leak flux $Q_{1,leak}$ must be known because both cases consider the expressions of the steady-state chamber pressure.

The leak rate was determined during the first test, while the PFG flow is a measurable quantity. The latter is a much more reliable value than the estimate of the leak rate. Unlike the first scenario, the second allows considering the two values. Its estimation is then more precise because it is not only based on a parameter itself estimated by a test. For this reason, the test scenario determining S_1 considers the second possibility.

Test scenario Again the test begins when the initial pressures are equal to 0.1 mbar, the valve is open, and the PFG flux is null. It is composed of the following step:

- **Step 1:** The chambers are emptied by the turbopumps until their ultimate pressure.
- **Step 2:** The valve of the duct between both chamber is closed.
- **Step 3:** A known mass flow rate is injected through the PFG and generates an additional inflow which increases the pressure of the main vessel. The mass usage does not matter here because the valve is closed.
- **Step 4:** At the steady-state, the pressure probe and the PFG provide the main chamber pressure and the PFG flux.
- **Step 5:** The PFG stops emitting gas. The main chamber retrieves its ultimate pressure.

Figure 5.5 presents the pressures evolution during the test and the intermediates pressures and times are listed in Table 5.3.

Situations	Time [s]	Main Chamber Pressure [mbar]	Secondary Chamber Pressure [mbar]
(1)	2.6288	3.4879×10^{-8}	4.9426×10^{-8}
(2)	3.3547	3.4483×10^{-8}	5.000×10^{-8}
(3)	5.1446	1.9226×10^{-5}	5.0000×10^{-5}
(4)	6.9284	3.4483×10^{-8}	5.000×10^{-8}

Table 5.3: Pressures and times of the intermediate situations of the third test

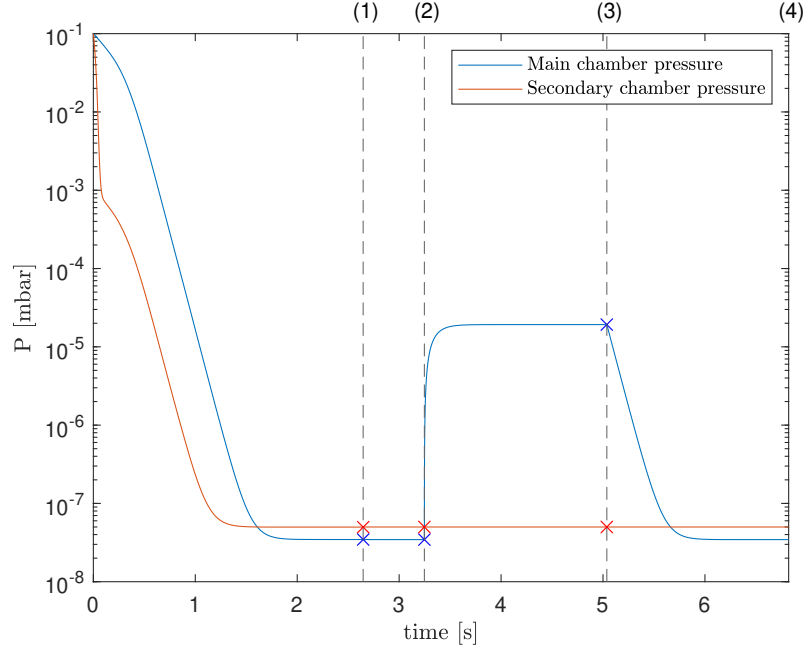


Figure 5.5: Pressures evolution in both chamber during the third test

Note that in the model equations, the turbopump start time is not taken into account. In reality, it takes several minutes before reaching its maximum speed. The times displayed in Figure 5.5 and Table 5.3 allow a better understanding of the tests but do not represent the actual duration of the test.

Analytical reasoning

As a reminder of the model analytical verification (second case of Section 4.3), when the valve is open and the PFG is turned on, the steady-state pressure of the first chamber is given by

$$P_{c1} = \frac{Q_{PFG} + Q_{1,leak}}{S_1}.$$

Therefore, the pumping speed of the first turbopump is

$$S_1 = \frac{Q_{PFG} + Q_{1,leak}}{P_{c1}}.$$

According to Section 4.2, the PFG particle flux is equal to

$$\dot{N}_{PFG} = \frac{SCCM}{6 \times 10^7} \times \frac{N_a}{V_{m,n}},$$

with $SCCM$ representing the PFG flux expressed in [SCCM] and $V_{m,n} = \frac{RT_n}{p_n} = \frac{N_a k T_n}{p_n}$ the standard gas molar volume in [m³/mol] also introduced in Section 4.2.

To convert it to flux expressed in [mbar.L/s], the equation 4.4 yields to

$$Q_{PFG} = 10 \dot{N}_{PFG} k T_{c1}.$$

Knowing that the nominal value of the PFG flux is set at 3 SCCM (see Table 4.1), the gas flow of the PFG is

$$\begin{aligned} Q_{PFG} &= 10 \frac{3}{6 \times 10^7} \times \frac{N_a}{V_{m,n}} kT_{c1} \\ &= \frac{1}{2 \times 10^6} \times \frac{N_a p_n}{N_a k T_n} kT_{c1} \\ &= \frac{1}{2 \times 10^6} \times \frac{p_n}{T_n} T_{c1}. \end{aligned}$$

If the probes provide the pressure of the situation (3), the pumping speed provided by the model is $S_1 = 2899.3$ L/s. As the parameter input to the simulation was 2900 L/s, the relative difference is 0.024 %. These results verify the test used as well as the values provided by the model.

5.2.4 Second turbopump pumping speed

Measurement test

The pumping speed of the second turbopump should be found with a test analogous to the first turbopump. As explained previously, the PFG flow must be integrated into the calculations to increase the precision of the results. Unfortunately, the different flows at the level of the valve are all unknown. To counter this difficulty, the turbopump of the first chamber is stopped. Therefore, all the flow entering the secondary chamber corresponds to the PFG flow.

Test scenario The initial condition remain the same. Before starting a new step, the system should reach a steady state. The steps of this scenario are:

- **Step 1:** The turbopumps empty the two chambers. During this step, the duct valve is already open.
- **Step 2:** PFG is turned on and its mass utilization is no null.
- **Step 3:** As in the first test (to determine $Q_{1,leak}$), the first turbopump is stopped, and its valve is closed to prevent the particles exiting the main chamber.
- **Step 4:** At the steady-state, the secondary chamber pressure and the PFG flux are measured.
- **Step 5:** The turbopump of the main chamber restarts and its downstream valve opens.
- **Step 6:** The PFG stops emitting gas.

As for the previous tests, the model follows the pressure evolution expected during the experiment. The result corresponds to Figures 5.6 and 5.7. The pressures of the two chambers at the level of the dotted line are listed in Table 5.4.

As the system takes a long time to reach a state, two graphs are necessary to represent the different stages distinctly. Note that the mass utilization slightly influences the convergence times of each step but has no impact on the pumping speed estimation (see analytical reasoning). The values and the graphs correspond to the case where η_m is not null.

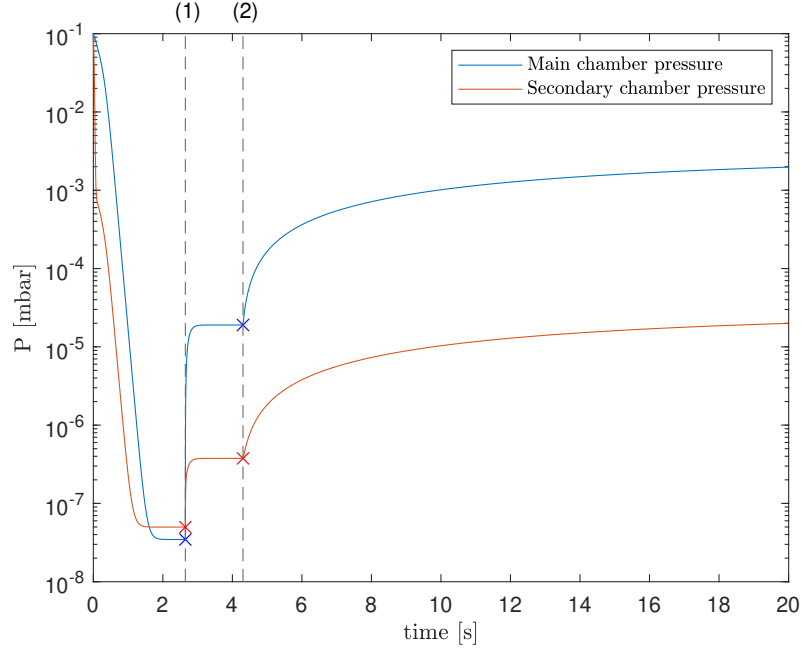


Figure 5.6: First part of the pressures evolution in both chamber during the fourth test

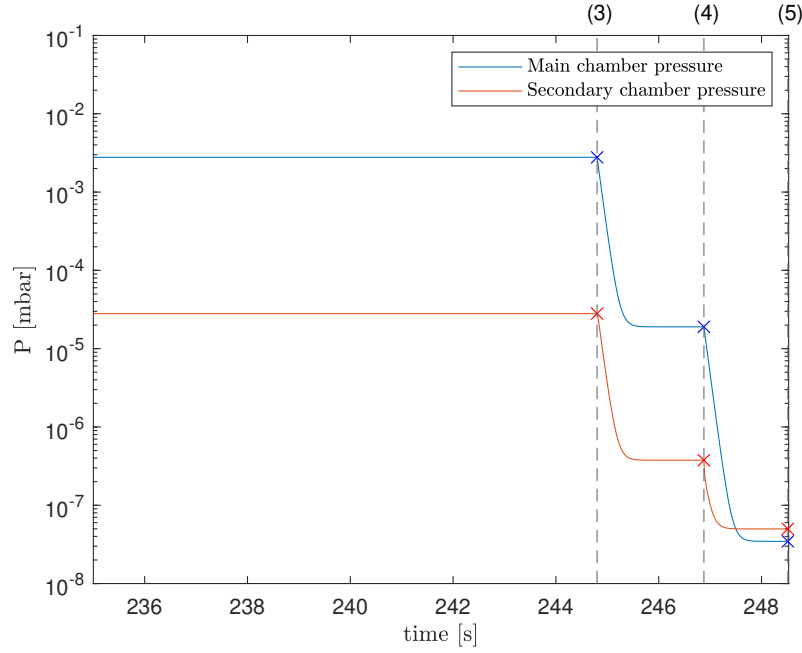


Figure 5.7: Second part of pressures evolution in both chamber during the fourth test

Analytical reasoning

To obtain the analytical expression of the pressure P_{c2} at the situation (3), it is required to consider Equations 4.1. At the steady-state (with first turbopump flow

Situations	Time [s]	Main Chamber Pressure [mbar]	Secondary Chamber Pressure [mbar]
(1)	2.6288	3.4879×10^{-8}	4.9426×10^{-8}
(2)	4.2545	1.8836×10^{-5}	6.1505×10^{-7}
(3)	108.7822	0.0012	2.8021×10^{-5}
(4)	110.7645	1.8836×10^{-5}	6.1505×10^{-7}
(5)	112.3786	3.4879×10^{-8}	4.9426×10^{-8}

Table 5.4: Pressures and times of the intermediate situations of the second test

null $\dot{N}_{P1} = 0$), they become

$$\begin{aligned} 0 &= \dot{N}_{PFG} + \dot{N}_{2,slow}(p_{c2}) + \dot{N}_{1,leak} - \dot{N}_{1,fast} - \dot{N}_{1,slow}(p_{c1}), \\ 0 &= \dot{N}_{1,fast} + \dot{N}_{1,slow}(p_{c1}) + \dot{N}_{2,leak} - \dot{N}_{P2}(p_{c2}) - \dot{N}_{2,slow}(p_{c2}). \end{aligned}$$

The sum of these two expression gives

$$\dot{N}_{P2}(p_{c2}) = \dot{N}_{PFG} + \dot{N}_{1,leak} + \dot{N}_{2,leak}.$$

As in Section 4.3, the terms can be replaced by the corresponding flux

$$Q_{P2} = S_2 P_{c2} = Q_{PFG} + Q_{1,leak} + Q_{2,leak}.$$

Therefore, the pumping speed of the secondary chamber is given by:

$$S_2 = \frac{1}{P_{c2}} (Q_{PFG} + Q_{1,leak} + Q_{2,leak}).$$

By using the values Q_{PFG} , $Q_{1,leak}$ and $Q_{2,leak}$ previously computed, the pumping speed given by the model is $S_2 = 1992.9$ L/s. For clarity, we reinstate that the theoretical values is 2000 L/s as given in Table 4.1.

The relative deviation is 0.3 %, so this test is satisfactory to determine the pumping speed of the second turbopump.

5.2.5 Charge exchange ions impact

Faraday probe calibration

This test calibrates the Faraday Probe to identify the CEX ion impact on the fast-flux $N_{1,fast}$. The calibration entails measuring the probe current at four background pressures. There are two ways to vary this pressure. Either the feed gas flux changes or the pumping speed changes. Indeed the lower the pumping speed, the higher the background pressure.

For the sake of simplicity, different pumping speeds are used to obtain the four background pressures. Four constraints have to be respected to ensure efficient calibration. First, the pressure must stay between 10^{-5} and 4×10^{-5} mbar. One of these pressure is the lowest achievable pressure when the PFG runs. It corresponds to the case where the pumping speed is maximum. Then, as ions rebound and interact with the vessel walls, the valve between both chambers stays open during the measurements. It prevents errors caused by particles bouncing off the closed

valve. Finally, the mass utilization must be different from zero to produce CEX ions in the background gas. Indeed, Charge EXchange ions come from an electron exchange from a fast ion to a slow neutral. It results in a fast neutral particle and a slow ion. But, if the mass utilization is null, no ion is produced, and no charge exchange interaction occurs.

Test scenario At the beginning of this test, the PFG flux is null, the valve is open, and the two turbopumps operate at their maximum speed. Again the system must stabilize before starting the next step.

- **Step 1:** The pressures of both chambers are initially at 0.1 mbar. The turbopumps switch on and decrease these pressures.
- **Step 2:** To start the calibration, The PFG switches on with a mass utilization different from zero.
- **Step 3, 5, 7, 9:** These four steps are similar but provide different results due to the different pumping speed S_1 . During these steps, the pumping speed of the main chamber turbopump decreases, and the equilibrium state changes.
- **Step 4, 6, 8, 10:** At the steady-state, the Faraday Probe measures the current, and the pressure sensor provides the main chamber pressure.
- **Step 11:** At the calibration end, the pumping speed of the first turbopump retrieves its initial velocity.
- **Step 12:** The PFG switches off.

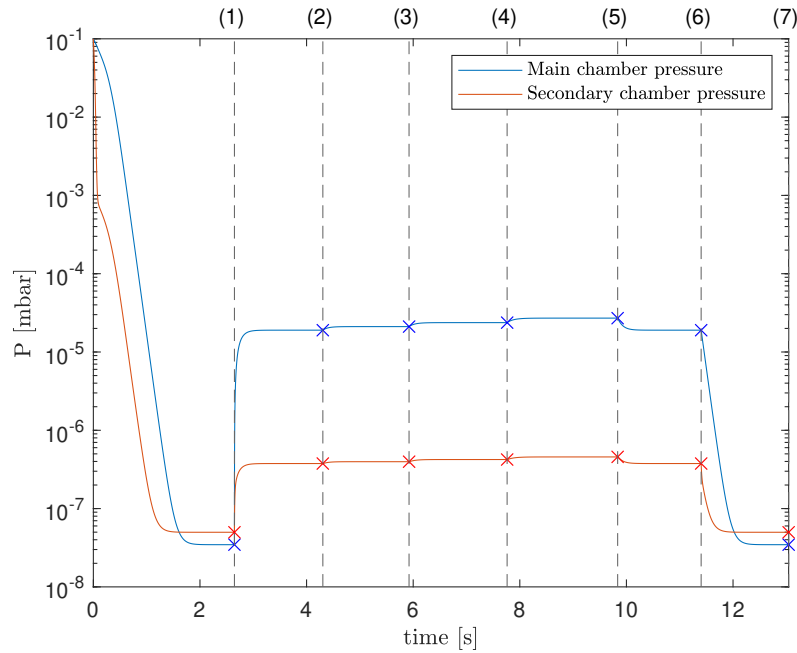


Figure 5.8: Pressures evolution in both chamber during the Faraday Probe Calibration

Situations	Time [s]	Main Chamber Pressure [mbar]	Secondary Chamber Pressure [mbar]
(1)	2.6288	3.4879×10^{-8}	4.9426×10^{-8}
(2)	4.2545	1.8836×10^{-5}	6.1505×10^{-7}
(3)	5.8412	2.0895×10^{-5}	6.6226×10^{-7}
(4)	7.6305	2.3460×10^{-5}	7.9637×10^{-7}
(5)	9.6852	2.6744×10^{-5}	7.9637×10^{-7}
(6)	11.2315	1.8836×10^{-5}	6.1505×10^{-7}
(7)	128712	3.4879×10^{-8}	4.9426×10^{-8}

Table 5.5: Pressures and times of the intermediate situations of the Faraday Probe Calibration

The evolution of the pressure obtained by the model is presented in Figure 5.8. The precise values of the different situations indicated in the figure are given in Table 5.5.

As predicted above, when the pumping speed decreases, the pressure increases. Note that the four pressures of the situation (2), (3), (4), and (5) are all included in the regulated interval.

5.2.6 Slow flux transmission probabilities

Using the values obtained in the previous tests, it is now possible to determine the two transmission probabilities of slow flows. Indeed, when the mass utilization is zero, that is means that PFG is used as feed of thermalized gas but it is not fired, only the slow fluxes $\dot{N}_{1,slow}$ and $\dot{N}_{2,slow}$ are present in the duct. The fast flow terms do not appear in the steady-state pressure expressions, and it is possible to find the slow transmissivities values without knowing $\tau_{1,fast}$.

Conversely, when the mass utilization is different from zero, both slow and fast fluxes are present. The pressures depend on the three transmissivities. Thus, it is not possible to find $\tau_{1,fast}$ without knowing $\tau_{1,slow}$, and $\tau_{2,slow}$.

These two last are determined by one manipulation. This section gives the test scenario and the analytical reasoning providing probabilities at the same time.

Measurement test

The test consists of measuring the pressures, the PFG flow, and the temperatures when the system is steady-state, the valve is open, and the PFG emits a gas flow. Thanks to the analytical expression of the steady-state pressures, it is possible to determine the slow flux transmissivities. To neglect the unknown fast flux in these expressions, the mass utilization η_m must remain zero.

Test scenario When the test starts, the valve is already open, but the PFG is still off. The different steps are:

- **Step 1:** The chambers are pumped by turbopumps.
- **Step 2:** The PFG is fed with gas but is not turned on (no production of ions and zero mass utilization).

- **Step 3:** When the two chambers have reached their equilibrium state, the parameters required for the steady-state equations are measured. Therefore, the two pressure probes provide the chamber pressure, the PFG gives the PFG flux, and the resistance thermometers measure the temperature of each chamber.
- **Step 4:** The PFG is turned off.

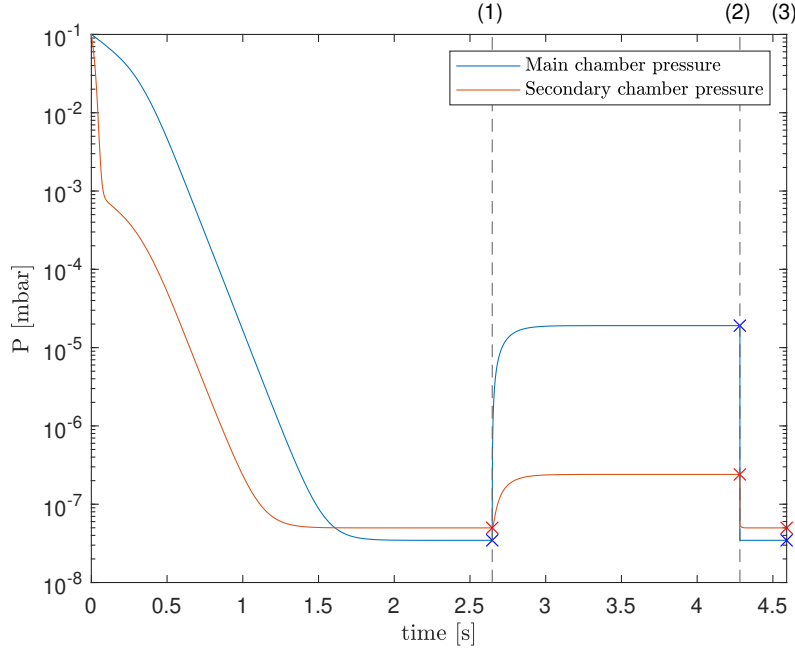


Figure 5.9: Pressures evolution in both chamber during the sixth test

Situations	Time [s]	Main Chamber Pressure [mbar]	Secondary Chamber Pressure [mbar]
(1)	2.6288	3.4879×10^{-8}	4.9426×10^{-8}
(2)	4.2558	1.8927×10^{-5}	4.8264×10^{-7}
(3)	4.6357	3.4879×10^{-8}	4.9426×10^{-8}

Table 5.6: Pressures and times of the intermediate situations of the sixth test

Figure 5.9 makes it possible to follow the evolution of the pressure during the test. For more precision, the values at the intermediate time instants are in Table 5.6.

Analytical reasoning

Contrary to the other experiments, the model equations are not sufficient to determine the transmissivities. Considering the steady-state continuity equation of the most general case

$$\begin{aligned}
 0 &= \dot{N}_{PFG} + \dot{N}_{2,slow}(p_{c2}) + \dot{N}_{1,leak} - \dot{N}_{P1}(p_{c1}) - \dot{N}_{1,fast} - \dot{N}_{1,slow}(p_{c1}), \\
 0 &= \dot{N}_{1,fast} + \dot{N}_{1,slow}(p_{c1}) + \dot{N}_{2,leak} - \dot{N}_{P2}(p_{c2}) - \dot{N}_{2,slow}(p_{c2}).
 \end{aligned}$$

The fast flux terms disappear thanks to the null mass utilization.

$$\begin{aligned} 0 &= \dot{N}_{PFG} + \dot{N}_{2,slow}(p_{c2}) + \dot{N}_{1,leak} - \dot{N}_{P1}(p_{c1}) - \dot{N}_{1,slow}(p_{c1}), \\ 0 &= \dot{N}_{1,slow}(p_{c1}) + \dot{N}_{2,leak} - \dot{N}_{P2}(p_{c2}) - \dot{N}_{2,slow}(p_{c2}). \end{aligned}$$

The particle flows are converted into gas flow. The system becomes

$$\begin{aligned} 0 &= Q_{PFG} + P_{c2}1000A_2\tau_{2,slow}\sqrt{\frac{kT_{c2}}{2\pi m}} + Q_{1,leak} - S_1P_{c1} - P_{c1}1000A_1\tau_{1,slow}\sqrt{\frac{kT_{c1}}{2\pi m}}, \\ 0 &= P_{c1}1000A_1\tau_{1,slow}\sqrt{\frac{kT_{c1}}{2\pi m}} + Q_{2,leak} - S_2P_{c2} - P_{c2}1000A_2\tau_{2,slow}\sqrt{\frac{kT_{c2}}{2\pi m}}. \end{aligned} \quad (5.4)$$

It is possible to prove that this system does not provide a solution. In matrix form the equations are

$$\begin{bmatrix} 1 & -1 \\ -1 & 1 \end{bmatrix} \begin{bmatrix} x \\ y \end{bmatrix} = \begin{bmatrix} Q_{PFG} + Q_{1,leak} - S_1P_{c1} \\ Q_{2,leak} - S_2P_{c2} \end{bmatrix},$$

$$\text{with } x = P_{c1}1000A_1\tau_{1,slow}\sqrt{\frac{kT_{c1}}{2\pi m}} \text{ and } y = P_{c2}1000A_2\tau_{2,slow}\sqrt{\frac{kT_{c2}}{2\pi m}}.$$

As the determinant of the first matrix is null ($1.1 - (-1)^2 = 0$), the system cannot provide a solution.

From now on, only Equation 5.4 is considered. It takes the form

$$P_{c1}1000A_1\tau_{1,slow}\sqrt{\frac{kT_{c1}}{2\pi m}} - P_{c2}1000A_2\tau_{2,slow}\sqrt{\frac{kT_{c2}}{2\pi m}} = S_2P_{c2} - Q_{2,leak}. \quad (5.5)$$

From here, it is required to make a simplification to obtain some results. Considering the case of the VKI's facility, two different simplifications are possible.

First simplification The first possibility is to consider that the secondary chamber pressure is much lower than the pressure of the first chamber. Consequently, the slow flux towards the secondary chamber is much higher than the other one. And the transmission probability $\tau_{2,slow}$ is assumed null. This assumption is not problematic because if $P_{c1} \gg P_{c2}$ at the situation (2), the influence of $\tau_{2,slow}$ on $\tau_{1,slow}$ becomes negligible. It can be observed by using the relation 5.5 to calculate

$$\left. \frac{\partial \tau_{1,slow}}{\partial \tau_{2,slow}} \right|_{\tau_{2,slow}=1} = \frac{P_{c2}A_2T_{c2}}{P_{c1}A_1T_{c1}}.$$

This observation is still valid even when $\tau_{2,slow}$ is maximal: $\tau_{2,slow} = 1$. The impact of this simplification is studied during the fast-flux transmissivity analysis. If the slow flow going to the main chamber becomes insignificant, the relation 5.5 becomes

$$P_{c1}1000A_1\tau_{1,slow}\sqrt{\frac{kT_{c1}}{2\pi m}} = S_2P_{c2} - Q_{2,leak}.$$

And the probability of transmission of the slow flow directed towards the second chamber is

$$\tau_{1,slow} = \frac{S_2P_{c2} - Q_{2,leak}}{P_{c1}1000A_1}\sqrt{\frac{2\pi m}{kT_{c1}}}.$$

Using this first method, the model provides $\tau_{1,slow} = 0.0582$. As shown by Table 4.2, the theoretical value is $\tau_{1,slow} = 0.0602$. The relative difference is therefore 3.4%.

Second simplification The other possible simplification is to assume that the temperature difference between the two chambers is negligible. This simplification allows to use the model described in [15]. Thanks to the reasoning described in Appendix A, this model allows to get the simple relation

$$A_1\tau_{1,slow} = A_2\tau_{2,slow}. \quad (5.6)$$

Equations 5.5 and 5.6 form therefore a system of two equations with two unknowns $\tau_{1,slow}$ and $\tau_{2,slow}$. They yield to

$$\tau_{1,slow} = \frac{\sqrt{2\pi m}}{1000A_1\sqrt{k}} \left(\frac{S_2P_{c2} - Q_{2,leak}}{P_{c1}\sqrt{T_{c1}} - P_{c2}\sqrt{T_{c2}}} \right), \quad (5.7)$$

$$\tau_{2,slow} = \frac{A_1}{A_2}\tau_{1,slow}. \quad (5.8)$$

By using the pressures at (2), the model provides the value $\tau_{1,slow} = 0.0597$ and $\tau_{2,slow} = 0.4263$. As their theoretical values are $\tau_{1,slow} = 0.0602$ and $\tau_{2,slow} = 0.5154$ (see Table 4.2). Their relative differences are 0.9 % and 17.3 %. This simplification is therefore more accurate for the estimation of $\tau_{1,slow}$ than the first one. The impact of this assumption on $\tau_{1,fast}$ is further discussed studied in the next section.

5.2.7 Fast flux transmission probability

Measurement test

To determine the fast-flux transmission probability, the test is the same as the previous one. For this test, the mass utilization of the PFG is not zero, and the fast flow in the duct must be measured by the Faraday Probe.

Test scenario The initial conditions are always the same: $P_{c1} = P_{c2} = 0.1$ mbar, the valve is open and the PFG does not emit gas.

- **Step 1:** The vessels are pumped down.
- **Step 2:** The PFG is turned on and its mass utilization is different from zero.
- **Step 3:** As for the previous test, a set of measurements are realized at the steady-state. Therefore, the pressure probes give the pressures of both chambers, the thermometers estimate the two temperatures, the PFG displays its flow, and the Faraday Probe provides the fast ions flux.
- **Step 4:** The PFG turns off, and the chamber returns to their ultimate pressure.

Figure 5.10 presents the pressure evolution during this last manipulation. Table 5.7 lists the pressure corresponding to the dotted lines of the figure.

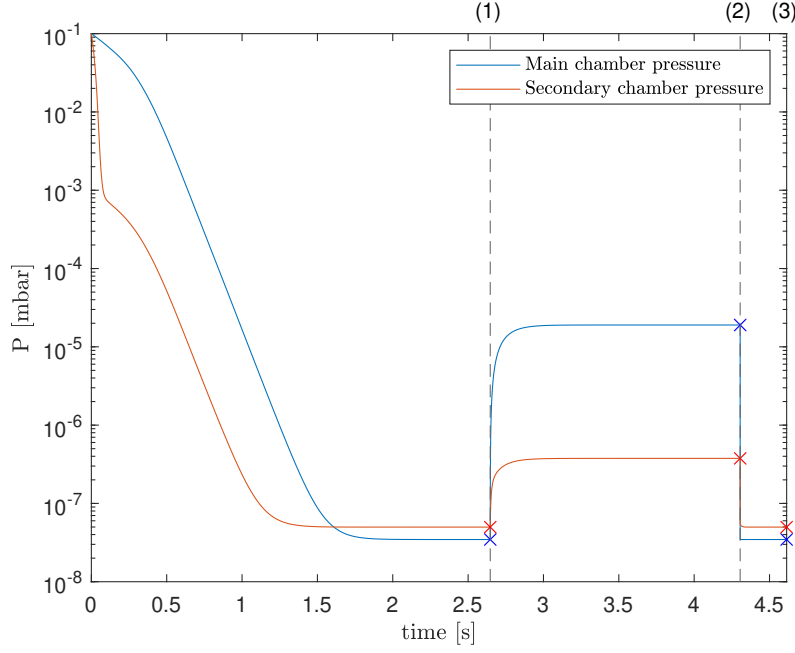


Figure 5.10: Pressures evolution in both chamber during the seventh test

Situations	Time [s]	Main Chamber Pressure [mbar]	Secondary Chamber Pressure [mbar]
(1)	2.6288	3.4879×10^{-8}	4.9426×10^{-8}
(2)	4.2545	1.8836×10^{-5}	6.1505×10^{-7}
(3)	4.6344	3.4879×10^{-8}	4.9426×10^{-8}

Table 5.7: Pressures and times of the intermediate situations of the seventh test

Analytical reasoning

The flow equations are sufficient to find the transmission probability of the fast flux. Converting,

$$0 = \dot{N}_{1,fast} + \dot{N}_{1,slow}(p_{c1}) + \dot{N}_{2,leak} - \dot{N}_{P2}(p_{c2}) - \dot{N}_{2,slow}(p_{c2}),$$

into,

$$0 = \tau_{1,fast}Q_{1,fast} + P_{c1}1000A_1\tau_{1,slow}\sqrt{\frac{kT_{c1}}{2\pi m}} + Q_{2,leak} - S_2P_{c2} - P_{c2}1000A_2\tau_{2,slow}\sqrt{\frac{kT_{c2}}{2\pi m}},$$

The transmissivity is therefore

$$\tau_{1,fast} = \frac{1}{Q_{1,fast}} \left(P_{c2}1000A_2\tau_{2,slow}\sqrt{\frac{kT_{c2}}{2\pi m}} + S_2P_{c2} - P_{c1}1000A_1\tau_{1,slow}\sqrt{\frac{kT_{c1}}{2\pi m}} - Q_{2,leak} \right).$$

Thanks to the values in Table 5.7, the model can give two value depending the used assumptions for the slow flux transmissivities. In the case of the first hypothesis, the model gives $\tau_{1,fast} = 0.2278$. And for the second one, the model obtain $\tau_{1,fast} = 0.2331$. The theoretical value being $\tau_{1,fast} = 0.2350$, the relative differences of these results are 3.1 % and 0.82 % respectively. First, these results

illustrate the procedure to determine the transmission probability of the fast stream based on a series of tests. Moreover, it shows that the second assumption for $\tau_{1,slow}$ and $\tau_{2,slow}$ is also more precise for the estimation of the transmission probability of the fast flow.

5.3 Conclusion

This chapter presents a series of tests designed to determine the transmission probability of a particle belonging to the rapid flow at the duct entrance. Only the chamber pressures, temperatures, and ionic flux at the tube inlet are directly measurable by a pressure probe, RTD and Faraday Probe respectively. The other parameters, such as the leak fluxes, the pumping speeds, and the transmission probabilities are calculated based on the model equations.

The designed procedure consists of seven tests. The first two are pressure rise tests and allow determining the leak rates of each chamber. The following two tests should determine the pumping speeds, but two scenarios are possible. The first only considers one estimate of the leakage flows while the other takes into account the PFG flow. The latter being a more precise value, it makes it possible to obtain a better estimate of the pumping speed. The PFG, therefore, emits a flow during the third and fourth tests. The fifth test is the Faraday probe calibration which measures the fast ion flux at the duct inlet and the charge exchange ion flux.

The sixth test makes it possible to estimate the transmission probability of slow flows at the duct level. Only for this test, the model equations are not sufficient, and an additional hypothesis is necessary. Two hypotheses are possible in the case of installation. The first assumes that the pressure of the secondary chamber is negligible compared to the pressure of the first chamber. The second is that the temperature difference between the two chambers is negligible. These two assumptions are used to calculate each transmissivity of the three flows of the duct. From the results provided by the model (see Table 5.8), it would seem that it is the second hypothesis that provides the best estimate of the fast flux transmission probability. However, these results are purely theoretical and considers that the probes measure the exact values. The influence of probe measurement uncertainties in these results is studied in Chapter 6.

Test	Facility condition	Measures	Results	Theoretical values	Relative difference
Test 1	Valve closed PFG flux null First pump stopped	ΔP_{c1} Δt_1	$Q_{1,leak} = 1.00 \times 10^{-4}$ mbar.L/s	$Q_{1,leak} = 1.00 \times 10^{-4}$ mbar.L/s	$1.6263 \times 10^{-13}\%$
Test 2	Valve closed PFG flux null Second pump stopped	ΔP_{c2} Δt_2	$Q_{2,leak} = 1.00 \times 10^{-4}$ mbar.L/s	$Q_{2,leak} = 1.00 \times 10^{-4}$ mbar.L/s	$1.3553 \times 10^{-14}\%$
Test 3	Valve closed PFG flux no null	Q_{PFG} P_{c1}	$S_1 = 2899.3$ L/s	$S_1 = 2900$ L/s	0.024%
Test 4	Valve open PFG flux no null First pump stopped	Q_{PFG} P_{c2}	$S_2 = 1992.9$ L/s	$S_2 = 2000$ L/s	0.3%
Test 5	Valve open PFG flux no null	$4 \times Q_{ion}$ $4 \times P_{c1}$	-	-	-
Test 6	Valve open PFG flux no null mass utilization null	P_{c1} P_{c2} T_{c1} T_{c2}	1 st assumption: $\tau_{1,slow} = 0.0582$ $\tau_{2,slow} = 0$ 2 nd assumption: $\tau_{1,slow} = 0.0597$ $\tau_{2,slow} = 0.4263$	$\tau_{1,slow} = 0.0602$ $\tau_{2,slow} = 0.5154$	3.4 % - 0.9 % 17.3 %
Test 7	Valve open PFG flux no null	P_{c1} P_{c2} T_{c1} T_{c2} $Q_{1,fast}$	1 st assumption: $\tau_{1,fast} = 0.2278$ 2 nd assumption: $\tau_{1,fast} = 0.2331$	$\tau_{1,fast} = 0.2350$	3.1 % 0.82 %

Table 5.8: Values and relative difference of the results provided by the tests

Chapter 6

Error propagation analysis

Chapter 5 describes the procedure obtaining the fast-flux transmission probability from a measurement set. In reality, an instrument measurement always has an error, i.e. a slight difference between the observed value and the true value. These errors can be random and difficult to estimate. Moreover, if a variable depends on one or more different measured variables, it will inherit the uncertainty in the measurements. The analysis of these uncertainties on derived quantities is called an error propagation analysis. This chapter has two sections. The first explains the basics of error propagation theory. The second one analyses the error propagation from the probe measurements to the final result $\tau_{1,fast}$.

6.1 Error analysis theory

This section introduces the basics of the uncertainty theory. It determines the uncertainty relation of a parameter depending on different measures.

6.1.1 Statistics reminder

As explained in [21], the error is supposed purely statistical, and all the results are assumed scattered around a mean value. If a diagnostic repeats a measurement N time, it obtains the set of measurements x_i , which has a mean value $\langle x \rangle$ given by

$$\langle x \rangle = \frac{1}{N} \sum_i x_i.$$

However, in the limit of infinite measurement number, they describe a distribution function. This function indicates the probability to obtain a particular observation in a single measurement. As the error is purely statistical, the mean of this distribution function is the correct parameter value. The mean deviation of one measurement with respect to this mean can be observed. It is called the standard deviation σ and it corresponds to the root square of the variance σ^2 , corresponding to

$$\sigma^2 = \lim_{N \rightarrow \infty} \left[\frac{1}{N} \sum_i (x_i - \langle x \rangle)^2 \right]. \quad (6.1)$$

For a given confidence interval around the mean value: $x \in (\langle x \rangle - k\sigma, \langle x \rangle + k\sigma)$ is associated a probability that a measurement falls into the interval. Considering a

Gaussian distribution as in Figure 6.1, this probabilities are roughly 68%, 95%, and 99.7% for $k = 1, 2, 3$ respectively.

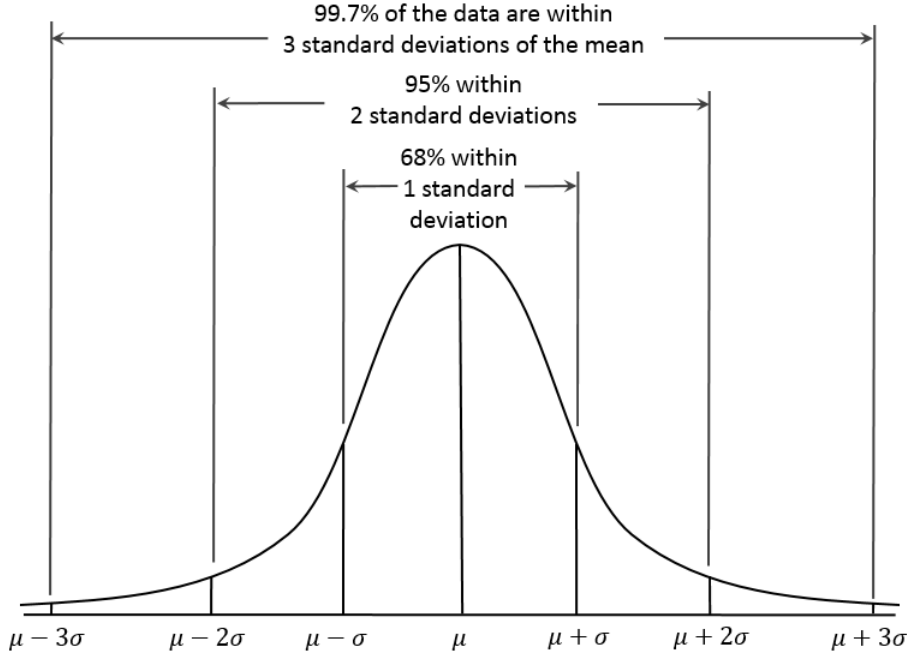


Figure 6.1: A visual representation of the Empirical (68-95-99.7) Rule based on the normal distribution (from [16])

6.1.2 Error propagation theory

Consider a dependent variable x that is a function of one or more different measured variables. This part explains the measurement uncertainties propagation to determine the uncertainty of the variable depending on these measurements.

For that, the quantity x is defined as a function of at least two measured variables, u and v

$$x = f(u, v, \dots), \quad (6.2)$$

and its mean is given by

$$\langle x \rangle = f(\langle u \rangle, \langle v \rangle, \dots),$$

where $\langle u \rangle$ and $\langle v \rangle$ are the mean of the measurement u and v , respectively. An individual result corresponds to

$$x_i = f(u_i, v_i, \dots) \quad i = 1, \dots, N.$$

By considering relation 6.3, the square of the standard deviation or variance is therefore

$$\sigma_x^2 = \lim_{N \rightarrow \infty} \left[\frac{1}{N} \sum_i (x_i - \langle x \rangle)^2 \right].$$

The Taylor series provides

$$x_i - \langle x \rangle \simeq (u_i - \langle u \rangle) \left(\frac{\partial x}{\partial u} \right) + (v_i - \langle v \rangle) \left(\frac{\partial x}{\partial v} \right) + \dots$$

where each partial derivative is evaluated with all the other variable fixed at their mean values.

Combining the two last relations, the variance σ_x^2 can be written according to the variances σ_u^2 , σ_v^2 , etc, as

$$\begin{aligned}\sigma_x^2 &\simeq \lim_{N \rightarrow \infty} \frac{1}{N} \sum_i \left[(u_i - \langle u \rangle) \left(\frac{\partial x}{\partial u} \right) + (v_i - \langle v \rangle) \left(\frac{\partial x}{\partial v} \right) + \dots \right]^2 \\ &\simeq \lim_{N \rightarrow \infty} \frac{1}{N} \sum_i \left[(u_i - \langle u \rangle)^2 \left(\frac{\partial x}{\partial u} \right)^2 + (v_i - \langle v \rangle)^2 \left(\frac{\partial x}{\partial v} \right)^2 + \right. \\ &\quad \left. 2(u_i - \langle u \rangle)(v_i - \langle v \rangle) \left(\frac{\partial x}{\partial u} \right) \left(\frac{\partial x}{\partial v} \right) + \dots \right].\end{aligned}\quad (6.3)$$

The first two terms correspond to the variances σ_u^2 and σ_v^2 given by

$$\sigma_u^2 = \lim_{N \rightarrow \infty} \left[\frac{1}{N} \sum_i (u_i - \langle u \rangle)^2 \right] \quad \sigma_v^2 = \lim_{N \rightarrow \infty} \left[\frac{1}{N} \sum_i (v_i - \langle v \rangle)^2 \right]$$

And the last terms is the covariance corresponding to

$$\sigma_{uv}^2 \equiv \lim_{N \rightarrow \infty} \left[\frac{1}{N} \sum_i [(u_i - \langle u \rangle)(v_i - \langle v \rangle)] \right]$$

Substituting in Equation 6.3, the new expression of the variance σ_x^2 is

$$\sigma_x^2 \simeq \sigma_u^2 \left(\frac{\partial x}{\partial u} \right)^2 + \sigma_v^2 \left(\frac{\partial x}{\partial v} \right)^2 + 2\sigma_{uv}^2 \left(\frac{\partial x}{\partial u} \right) \left(\frac{\partial x}{\partial v} \right) + \dots$$

The first two terms express how the uncertainties on u and v are propagated to x through its sensitivity, given by the partial derivative. The last term expresses the effect of the covariance (σ_{uv}) of the measurements u and v . But as the u and v fluctuations are assumed to be uncorrelated, their covariance is null. The previous relation is often reduced to

$$\sigma_x^2 \simeq \sigma_u^2 \left(\frac{\partial x}{\partial u} \right)^2 + \sigma_v^2 \left(\frac{\partial x}{\partial v} \right)^2 + \dots \quad (6.4)$$

As it is reasonable to consider all measurements uncorrelated, Equation 6.4 will be used to estimate the uncertainty.

6.2 Error propagation analysis

In the case of this thesis, the goal is to determine the uncertainty of the transmission probability $\tau_{1,fast}$ obtained from the measurements tests.

As stated in Chapter 5, the different dimensions of the vessel and of the duct are supposed known. So their uncertainties are assumed to be zero. The other parameters are unknown and must be measured or calculated based on measurements. There are two ways to get their uncertainties. Either it is a parameter directly measured by a probe, and its uncertainty corresponds to the measurement uncertainty. Or it is a parameter determined using a test detailed in Section 5.2 and its uncertainty is given by Relation 6.4

6.2.1 Measurement uncertainties

The parameters measured by the various instrument of the installation are:

- P_{c1} and P_{c2} the pressures of both chambers in [mbar].
- Q_{PFG} the total PFG flux in [mbar.L/s].
- $Q_{1,fast}$ the fast particle flux at the valve entrance in [mbar.L/s].
- T_{c1} and T_{c2} the temperature of both chambers in [K].

Their uncertainties correspond to the uncertainties of the probes use provided by the manufacturers. In the case of pressure probes, they have an uncertainty of 30% (see [29]). Therefore the pressure measurement of the chamber i has an uncertainty $0.3P_{ci}$. According to the documents [5] and [4], the uncertainty of the PFG flux also depends on the measured value in [SCCM] and is given by $(0.005SCCM + 0.001 \times \text{full scale})$. The full scale corresponds to the actual value of the maximum scale value. In the case of the PFG, it is equals to 400 sccm. The Faraday Probe uncertainty depends on a lot of factors and is difficult to estimate a priori. In the case of vacuum chambers simulating the atmospheric conditions, it is recommended to consider an uncertainty of 5% in far-field plumes measurements and 10% in near-field plume measurements (see [7]). These measurements types refer to the distance between the probe and the gas source. In [24], far-field plume measurements correspond to the case where the probe is located at least 10 times the dimension of its collecting surface. As this is of the order of 1 mm, the Faraday probe performs far-field plume measurements in the installation of the VKI. Consequently, the fast-flux uncertainty is assumed to be 5%. The PT100 probes measure the temperature with an accuracy of 0.01K according to[14].

All these uncertainties respect the standards imposed by ISO 2602: 1980 which stipulates that all these uncertainties have a confidence interval of 95 % (see ISO 2602: 1980 [13]). Therefore they are equal two standard deviations of a measurement. Table 6.1 summarizes the different uncertainties and standard deviation of these parameters.

Probe	Uncertainty	Standard deviation	Units
Pressure Probe	$0.3P_{ci}$	$0.15P_{ci}$	[mbar]
PFG	$0.005SCCM + 0.004$	$\frac{1}{2}(0.005SCCM + 0.004)$	[SCCM]
Faraday Probe	$0.05Q_{1,fast}$	$0.025Q_{1,fast}$	[mbarL/s]
Temperature Probe	0.01	0.005	[K]

Table 6.1: Uncertainty(95% confidence interval) and standard deviation of all Measurement probe used during test procedure

6.2.2 Leak flux uncertainties

During the two first tests, the leak rates are obtained using a Pressure rise test. From the section 5.2, these tests estimate the fluxes using the expression

$$Q_{i,leak} = \frac{V_i \Delta P_{ci}}{\Delta t_i} \quad i = 1, 2.$$

With V_i the chamber volume, ΔP_{ci} the pressure difference and Δt_i the required time to reach the pressure threshold in the chamber i .

The volumes are supposed known and their uncertainties null. Expression 6.4 provides the uncertainty on the leak rate

$$\sigma_{Q_{i,leak}}^2 = \sigma_{\Delta P_{ci}}^2 \left(\frac{\partial Q_{i,leak}}{\partial \Delta P_{ci}} \right)^2 + \sigma_{\Delta t_i}^2 \left(\frac{\partial Q_{i,leak}}{\partial \Delta t_i} \right)^2 \quad i = 1, 2. \quad (6.5)$$

For the time measurements uncertainties, the document [21] shows that if

$$\Delta t_i = t'_i - t_i,$$

its uncertainty, is given by

$$\begin{aligned} \sigma_{\Delta t_i}^2 &= \sigma_{t'_i}^2 \left(\frac{\partial \Delta t_i}{\partial t'_i} \right)^2 + \sigma_{t_i}^2 \left(\frac{\partial \Delta t_i}{\partial t_i} \right)^2 \\ &= \sigma_{t'_i}^2 (1)^2 + \sigma_{t_i}^2 (-1)^2 \\ &= \sigma_{t'_i}^2 + \sigma_{t_i}^2. \end{aligned}$$

As the two instants t_i and t'_i are measured by the same probe, their uncertainties are equal: $\sigma_{t_i} = \sigma_{t'_i}$. Therefore,

$$\sigma_{\Delta t_i}^2 = 2\sigma_{t_i}^2,$$

where σ_{t_i} is known. The same reasoning cannot be applied in the case of pressure probes because the uncertainties depend on the measured value. The pressure probes present uncertainty of 30% with an confidence interval of 95%. If P_{ci} is the pressure measured at the instant t and P'_{ci} the pressure measured at t' , their uncertainties are given by

$$\begin{aligned} \sigma_{P_{ci}}^2 &= (0.15P_{ci})^2, \\ \sigma_{P'_{ci}}^2 &= (0.15P'_{ci})^2. \end{aligned}$$

By considering the pressure difference

$$\Delta P_{ci} = P'_{ci} - P_{ci},$$

its error is

$$\begin{aligned} \sigma_{\Delta P_{ci}}^2 &= \sigma_{P'_{ci}}^2 \left(\frac{\partial \Delta P_{ci}}{\partial P'_{ci}} \right)^2 + \sigma_{P_{ci}}^2 \left(\frac{\partial \Delta P_{ci}}{\partial P_{ci}} \right)^2 \\ &= (0.15P'_{ci})^2 (1)^2 + (0.15P_{ci})^2 (-1)^2 \\ &= (0.15P'_{ci})^2 + (0.15P_{ci})^2 \\ &= 0.0225(P_{ci}'^2 + P_{ci}^2). \end{aligned}$$

The partial derivative of the relation 6.5 being

$$\begin{aligned} \left(\frac{\partial Q_{i,leak}}{\partial \Delta P_{ci}} \right) &= \frac{V_i}{\Delta t_i} \\ \left(\frac{\partial Q_{i,leak}}{\partial \Delta t_i} \right) &= \frac{-V_i \Delta P_{ci}}{(\Delta t_i)^2}, \end{aligned}$$

the leak flux uncertainties are given by

$$\sigma_{Q_{i,leak}}^2 = 0.0225(P_{ci}^2 + P_{ci}^2) \left(\frac{V_i}{\Delta t_i} \right)^2 + 2\sigma_{t_i}^2 \left(\frac{-V_i \Delta P_{ci}}{(\Delta t_i)^2} \right)^2. \quad (6.6)$$

This relation shows that the uncertainty of the leak flux diminishes with an increase of the test duration. Thanks to the values presented in Chapter 5, the model provides $\sigma_{Q_{1,leak}} = 1.5052 \times 10^{-8}$ and $\sigma_{Q_{2,leak}} = 1.5081 \times 10^{-8}$ mbar.L/s.

These values mean that 68% of the results provided by the test in the chamber i are within the range $[Q_{i,leak} - \sigma_{Q_{i,leak}}, Q_{i,leak} + \sigma_{Q_{i,leak}}]$. As these uncertainties are very low compared to the leak rates ($Q_{i,leak} = 1.00 \times 10^{-4}$ mbar L/s), these test are conclusive. All the values of the uncertainties are listed in Table 6.2 in the conclusion of this chapter.

6.2.3 First pump pumping speed

From Chapter 5, the first pumping speed is found by using

$$S_1 = \frac{Q_{1,leak} + Q_{PFG}}{P_{c1}}.$$

The corresponding uncertainty is therefore

$$\begin{aligned} \sigma_{S_1}^2 &= \sigma_{Q_{1,leak}}^2 \left(\frac{\partial S_1}{\partial Q_{1,leak}} \right)^2 + \sigma_{Q_{PFG}}^2 \left(\frac{\partial S_1}{\partial Q_{PFG}} \right)^2 + \sigma_{P_{c1}}^2 \left(\frac{\partial S_1}{\partial P_{c1}} \right)^2 \\ &= \sigma_{Q_{1,leak}}^2 \left(\frac{1}{P_{c1}} \right)^2 + \sigma_{Q_{PFG}}^2 \left(\frac{1}{P_{c1}} \right)^2 + 0.0225 P_{c1}^2 \left(\frac{-(Q_{1,leak} + Q_{PFG})}{P_{c1}^2} \right)^2 \\ &= \frac{1}{P_{c1}^2} \left(\sigma_{Q_{1,leak}}^2 + \sigma_{Q_{PFG}}^2 + 0.0225(Q_{1,leak} + Q_{PFG})^2 \right). \end{aligned}$$

According to this expression, the greater the pressure, the lower the uncertainty. It is logical because the greater the pressure, the lower the pumping speed. Note that this expression depends only on parameters already known since $Q_{1,leak}$ and $\sigma_{Q_{1,leak}}$ were determined during the first test.

The result obtained from the model is $\sigma_{S_1} = 478.7520$ L/s. The value is very high because the denominator of the σ_{S_1} is the main chamber pressure ($P_{c1} = 1.9226 \times 10^{-5}$ mbar). This calculation proves that the test provides 68 % of its data in the range $[2421.2; 3378.752]$ L/s. As this range is quite large the selected test is not optimal for determining the pumping speed initially at $S_1 = 2900$ L/s. But S_1 not being the final result, it is interesting to follow the propagation of this uncertainty and to estimate its impact on the uncertainty of $\tau_{1,fast}$.

6.2.4 Second pump pumping speed

Considering the condition of the test where the valve is open, the PFG turned on, and the first turbopump is stopped, the pumping speed is given by (see Section 5.2)

$$S_2 = \frac{1}{P_{c2}} (Q_{PFG} + Q_{1,leak} + Q_{2,leak}).$$

And its uncertainty

$$\begin{aligned}\sigma_{S_2}^2 &= \sigma_{Q_{1,leak}}^2 \left(\frac{\partial S_2}{\partial Q_{1,leak}} \right)^2 + \sigma_{Q_{2,leak}}^2 \left(\frac{\partial S_2}{\partial Q_{2,leak}} \right)^2 + \sigma_{Q_{PFG}}^2 \left(\frac{\partial S_2}{\partial Q_{PFG}} \right)^2 + \sigma_{P_{c2}}^2 \left(\frac{\partial S_2}{\partial P_{c2}} \right)^2 \\ &= \sigma_{Q_{1,leak}}^2 \left(\frac{1}{P_{c2}} \right)^2 + \sigma_{Q_{2,leak}}^2 \left(\frac{1}{P_{c2}} \right)^2 + \sigma_{Q_{PFG}}^2 \left(\frac{1}{P_{c2}} \right)^2 + \\ &\quad 0.0225 P_{c2}^2 \left(\frac{-(Q_{PFG} + Q_{1,leak} + Q_{2,leak})}{P_{c2}^2} \right)^2.\end{aligned}$$

As above, the higher the pressure, the lower the uncertainty of the pumping speed. The result provided by the model is $\sigma_{S_2} = 328.9765$ L/s. As $S_2 = 2000$ L/s, 68% of the results are comprised in $[1671.02; 2328]$ L/s. This interval is also quite large. Therefore this test is also not ideal to find the second pumping speed. The influence of this result is studied in the remainder of the section.

6.2.5 Slow flux transmissivities

As seen in Chapter 5, two hypotheses can be used to find the slow flux transmissivities. Either, the secondary chamber pressure is assumed much lower than the main chamber one. The corresponding transmission probabilities are given by Equation 6.7. Or the temperature difference between two chambers is supposed negligible, and the transmissivities become the relation 6.8.

$$\tau_{1,slow} = \sqrt{\frac{2\pi m}{kT_{c1}}} \frac{S_2 P_{c2} - Q_{2,leak}}{P_{c1} 1000 A_1} \quad \tau_{2,slow} = 0. \quad (6.7)$$

$$\tau_{1,slow} = \frac{\sqrt{2\pi m}}{1000 A_1 \sqrt{k}} \left(\frac{S_2 P_{c2} - Q_{2,leak}}{P_{c1} \sqrt{T_{c1}} - P_{c2} \sqrt{T_{c2}}} \right) \quad \tau_{2,slow} = \frac{A_1}{A_2} \tau_{1,slow}. \quad (6.8)$$

Although the second assumption provides slightly more accurate probabilities $\tau_{1,slow}$, $\tau_{2,slow}$ and $\tau_{1,fast}$, this does not eliminate the other assumption. Indeed, the goal of this tests set is to determine the most accurate fast-flux transmission probability $\tau_{1,fast}$ possible. The hypothesis to keep is therefore the one that minimizes the error on the final result and makes it possible to obtain the best estimate of $\tau_{1,fast}$. In this part, the uncertainties of $\tau_{1,slow}$ and $\tau_{2,slow}$ for both hypotheses are calculated. They are used to calculate the two resulting uncertainties of $\tau_{1,fast}$.

First hypothesis

By applying Equation 6.4, the expression the $\tau_{1,slow}$ uncertainty is given by

$$\begin{aligned}\sigma_{\tau_{1,slow}}^2 &= \sigma_{T_{c1}}^2 \left(\frac{\partial \tau_{1,slow}}{\partial T_{c1}} \right)^2 + \sigma_{S_2}^2 \left(\frac{\partial \tau_{1,slow}}{\partial S_2} \right)^2 + \sigma_{P_{c2}}^2 \left(\frac{\partial \tau_{1,slow}}{\partial P_{c2}} \right)^2 + \\ &\quad \sigma_{Q_{2,leak}}^2 \left(\frac{\partial \tau_{1,slow}}{\partial Q_{2,leak}} \right)^2 + \sigma_{P_{c1}}^2 \left(\frac{\partial \tau_{1,slow}}{\partial P_{c1}} \right)^2.\end{aligned}$$

Thanks to the previous test, all the uncertainties of this expression have already been determined. The partial derivatives are listed in Appendix B.1.

In the case of $\tau_{2,slow}$, its value is imposed at 0. There is therefore no uncertainty associated with the measurements.

Second hypothesis

The same reasoning can be applied with the second expression. This time, the uncertainty of $\tau_{1,slow}$ is

$$\begin{aligned} \sigma_{\tau_{1,slow}}^2 = & \sigma_{T_{c1}}^2 \left(\frac{\partial \tau_{1,slow}}{\partial T_{c1}} \right)^2 + \sigma_{S_2}^2 \left(\frac{\partial \tau_{1,slow}}{\partial S_2} \right)^2 + \sigma_{P_{c2}}^2 \left(\frac{\partial \tau_{1,slow}}{\partial P_{c2}} \right)^2 + \\ & \sigma_{Q_{2,leak}}^2 \left(\frac{\partial \tau_{1,slow}}{\partial Q_{2,leak}} \right)^2 + \sigma_{P_{c1}}^2 \left(\frac{\partial \tau_{1,slow}}{\partial P_{c1}} \right)^2 + \sigma_{T_{c2}}^2 \left(\frac{\partial \tau_{1,slow}}{\partial T_{c2}} \right)^2. \end{aligned}$$

Again the corresponding partial derivatives are listed in Appendix B.1.

For the other transmission uncertainty, the second expression of 6.8 allows to find

$$\sigma_{\tau_{2,slow}}^2 = \sigma_{\tau_{1,slow}}^2 \left(\frac{\partial \tau_{2,slow}}{\partial \tau_{1,slow}} \right)^2 = \sigma_{\tau_{1,slow}}^2 \left(\frac{A_1}{A_2} \right)^2$$

Results

The $\tau_{1,slow}$ uncertainties are $\sigma_{\tau_{1,slow}} = 0.0169$ and $\sigma_{\tau_{1,slow}} = 0.0176$ for the first and the second case. It would seem that the two assumptions provide very similar uncertainties. And although the high pumping speed uncertainties, these results remain acceptable. Their impacts on the uncertainties of $\tau_{1,fast}$ are studied in the next section. On the other hand, the second hypothesis allows to get $\sigma_{\tau_{2,slow}} = 0.1257$. This result is greater than $\sigma_{\tau_{1,slow}}$ because the inlet section A_1 is always larger than the outlet section A_2 .

6.2.6 Fast flux transmissivity

In the previous Chapter 5, it was shown that

$$\tau_{1,fast} = \frac{1}{Q_{1,fast}} \left(P_{c2} 1000 A_2 \tau_{2,slow} \sqrt{\frac{k T_{c2}}{2\pi m}} + S_2 P_{c2} - P_{c1} 1000 A_1 \tau_{1,slow} \sqrt{\frac{k T_{c1}}{2\pi m}} - Q_{2,leak} \right).$$

Expression 6.4 provide the corresponding uncertainty which is

$$\begin{aligned} \sigma_{\tau_{1,fast}}^2 = & \sigma_{Q_{1,fast}}^2 \left(\frac{\partial \tau_{1,fast}}{\partial Q_{1,fast}} \right)^2 + \sigma_{P_{c2}}^2 \left(\frac{\partial \tau_{1,fast}}{\partial P_{c2}} \right)^2 + \sigma_{\tau_{2,slow}}^2 \left(\frac{\partial \tau_{1,fast}}{\partial \tau_{2,slow}} \right)^2 + \sigma_{T_{c2}}^2 \left(\frac{\partial \tau_{1,fast}}{\partial T_{c2}} \right)^2 + \\ & \sigma_{S_2}^2 \left(\frac{\partial \tau_{1,fast}}{\partial S_2} \right)^2 + \sigma_{P_{c1}}^2 \left(\frac{\partial \tau_{1,fast}}{\partial P_{c1}} \right)^2 + \sigma_{\tau_{1,slow}}^2 \left(\frac{\partial \tau_{1,fast}}{\partial \tau_{1,slow}} \right)^2 + \\ & \sigma_{T_{c1}}^2 \left(\frac{\partial \tau_{1,fast}}{\partial T_{c1}} \right)^2 + \sigma_{Q_{2,leak}}^2 \left(\frac{\partial \tau_{1,fast}}{\partial Q_{2,leak}} \right)^2 \end{aligned}$$

Thanks to the devised testing procedure and the previous reasoning, all the parameters, and uncertainties of this expression are known. The partial derivatives are calculated in Appendix B.2.

Considering the values and the uncertainties provided by the two hypotheses (for $\tau_{1,slow}$ and $\tau_{2,slow}$) The first assumption provides $\sigma_{\tau_{1,fast}} = 0.3329$. And the second hypothesis allows to get $\sigma_{\tau_{1,fast}} = 0.3412$. Finally, it is the first hypothesis that has the lowest uncertainty. These values prove that the first assumption is more suited

to the chosen nominal condition. Indeed, as shown in Appendix B.1 and B.2, the partial derivative expressions depend on the slow flux transmission probabilities. It means that depending on the device transmissivities placed between both chambers, the best assumption is not always the first one. Nevertheless, the uncertainties obtained are quite large. There are three reasons for explaining these values. First, the two tests determining the pumping speed provide great uncertainties. They therefore favor error propagation for the estimation of $\tau_{1,fast}$.

Then, some instruments such as pressure probes have high measurement uncertainties and degrade the accuracy of the results.

Finally, the configuration chosen also impacts the quality of these results. As shown by Appendix B.2, some parameters can decrease the values of the partial derivatives of $\sigma_{\tau_{1,fast}}$. The fast flow $Q_{1,fast}$ belongs to the denominator of each derivative. So the larger this flow, the lower the uncertainty of $\tau_{1,fast}$. This observation is very interesting because it implies that some user-controllable parameters can improve the quality of the estimate. These are all parameters increasing the value of $Q_{1,fast}$. Therefore to improve the estimation of the probability of transmission of the rapid flow to the secondary chamber, the user can increase the PFG flow, the mass utilization, and the speed ratio. He can also decrease the PFG-duct distance d_{PFG} to increase the ion fraction reaching the intake.

6.3 Conclusion

The measuring devices used in testing all have measurement uncertainties. Consequently, an error propagation analysis is of paramount importance to determine the reliability and accuracy of the test results.

Based on the values provided by the model, it appears that the tests determining the leak rates have low uncertainties and provide precise estimates. On the other hand, the tests determining the pumping speed have high uncertainties. The estimates obtained belong to a large confidence interval, and their uncertainties influence the ensuing results. Finally, the uncertainties of the three transmission probabilities are calculated based on the two hypotheses introduced in Chapter 5.

Surprisingly, it is the first hypothesis that provides the lower uncertainty of the fast-flux transmissivity being the most suitable hypothesis for the chosen nominal conditions. However, this observation changes depending on the configuration. Indeed, the uncertainty depends on the values of the transmission probabilities. As indicated in Table 6.2, it appears that the values of the uncertainties of this transmissivity are high for the two hypotheses and further improvement of either the facility diagnostics accuracy or the testing scenarios has to be achieved in order for fast flux transmissivities to be measured.

Three explanations allow these values to be justified. First, the pumping speeds determination tests are not sufficiently precise and increase the uncertainty of the final results. Secondly, the used pressure probes have great uncertainty and decrease the reliability of the results. Finally, the expressions in Appendix B.2 prove that some configuration minimizes the uncertainty on the measurement of the probability of transmission. They prove that the higher the rapid flow directed towards the secondary chamber, the lower the uncertainty.

Test	Facility condition	Measures	Results	Theoretical values	Standard deviation
Test 1	Valve closed PFG flux null First pump stopped	ΔP_{c1} Δt_1	$Q_{1,leak} = 1.00 \times 10^{-4}$ mbar.L/s	$Q_{1,leak} = 1.00 \times 10^{-4}$ mbar.L/s	$\sigma_{Q_{1,leak}} = 1.5052 \times 10^{-8}$
Test 2	Valve closed PFG flux null Second pump stopped	ΔP_{c2} Δt_2	$Q_{2,leak} = 1.00 \times 10^{-4}$ mbar.L/s	$Q_{2,leak} = 1.00 \times 10^{-4}$ mbar.L/s	$\sigma_{Q_{2,leak}} = 1.5081 \times 10^{-8}$
Test 3	Valve closed PFG flux no null	Q_{PFG} P_{c1}	$S_1 = 2899.3$ L/s	$S_1 = 2900$ L/s	$\sigma_{S_1} = 478.7520$
Test 4	Valve open PFG flux no null First pump stopped	Q_{PFG} P_{c2}	$S_2 = 1992.9$ L/s	$S_2 = 2000$ L/s	$\sigma_{S_2} = 328.9765$
Test 5	Valve open PFG flux no null	$4 \times Q_{ion}$ $4 \times P_{c1}$	-	-	-
Test 6	Valve open PFG flux no null mass utilization null	P_{c1} P_{c2} T_{c1} T_{c2}	1 st assumption: $\tau_{1,slow} = 0.0582$ $\tau_{2,slow} = 0$ 2 nd assumption: $\tau_{1,slow} = 0.0597$ $\tau_{2,slow} = 0.4263$	$\tau_{1,slow} = 0.0602$ $\tau_{2,slow} = 0.5154$	$\sigma_{\tau_{1,slow}} = 0.0169$ - $\sigma_{\tau_{1,slow}} = 0.0176$ $\sigma_{\tau_{2,slow}} = 0.1257$
Test 7	Valve open PFG flux no null	P_{c1} P_{c2} T_{c1} T_{c2} $Q_{1,fast}$	1 st assumption: $\tau_{1,fast} = 0.2278$ 2 nd assumption: $\tau_{1,fast} = 0.2331$	$\tau_{1,fast} = 0.2350$	$\sigma_{\tau_{1,fast}} = 0.3329$ $\sigma_{\tau_{1,fast}} = 0.3412$

Table 6.2: Values and standard deviations of the results provided by the tests

Chapter 7

Conclusion

The objective of this work is to determine if there is a test set allowing to determine the an ABEP intake transmissivity in conditions similar to atmospheric VLEO conditions.

These tests will be realized inside the VKI 's vacuum installation. This facility consists of two vacuum chambers connected by a duct containing the equipment. The flows circulating between the two chambers must therefore pass through the intake. The High Vacuum medium is ensured by a pumping system composed of a backing pump and two turbopumps (one for each chamber). The backing pump is downstream of the two turbopumps and can reduce the installation pressure to a value of the order of 0.1 mbar. At sufficiently low pressure, the two turbopumps start and allow to reach pressures of the order of 10^{-8} mbar. A Particle Flow Generator placed in the main chamber in front of the inlet device simulates the atmospheric flow similar to VLEO conditions. It emits a fast particle flux with a certain proportion of fast particles (in the form of ions).

The pressure evolution within the installation is analyzed by a simple model based on the continuity equation. Based on a hypothesis set, this equation is applied to the two chambers. It allows following the pressure evolution as a function of a parameter series impacting the operation of the installation. This analytical model can also provide the theoretical steady-state pressure expressions according to these same parameters. Some parameters such as the transmission probabilities and the ion proportion reaching the tube entrance are obtained thanks to a VKI's tool based on the Test Particle Monte Carlo method.

This study then proposes a series of tests obtaining the transmission probability of a particle belonging to the rapid flow entering the duct between the two vessels. Based on parameters measured by probes and the analytical model equations, each test determines one variable or transmission probability which are not directly measurable. In the case of the test dedicated to the transmissivity of slow fluxes, the model equations are not sufficient. Two hypotheses can be used and make it possible to obtain results. The first considers that the pressure of the secondary chamber is much lower than that of the first chamber. The thermal flow going to the main vessel is therefore negligible compared to the other thermal flow. The other assumption assumes that the temperature difference between the two chambers is negligible. It thus makes it possible to use a model developed in [15]. By comparing the results with the theoretical values, it appears that the second hypothesis provides more accurate estimates of the transmission probabilities.

Finally, this work verifies the reliability of these tests through an error propagation study. Thanks to the model values, the uncertainties of the measurements are estimated and propagated to obtain the uncertainty of the measured fast flux transmission probability. The tests dedicated to pumping speeds have high uncertainties. Therefore provide results belonging to a large confidence interval. The fluctuation of the computed values can thus influence the estimation of the transmission probabilities. The two assumptions used to calculate $\tau_{1,slow}$ and $\tau_{2,slow}$ are studied. In the case of the nominal conditions chosen, this is the first assumption that provides the lowest uncertainties. Although the second assumption gives us better results, it is the first assumption that provides the most reliable results. It is therefore the first hypothesis that should be chosen. However, the calculation of the uncertainties depends on the values of the probability of transmission. Consequently, depending on the transmissivity values of the equipment placed in the duct, the best hypothesis is not always the first one. Finally it appears that the uncertainty of $\tau_{1,fast}$ is relatively high. Three reasons can justify this result. First, the tests discussed in this study are not all optimal (as the tests dedicated to pumping speed). Some of them provide high uncertainties and decrease the reliability of results. Then, some probes as pressure probe lack a little precision. Finally, the uncertainty was estimated for a specific configuration. As discussed before, the uncertainties are dependent on the facility configuration and can be reduced for other testing scenarios. To conclude, we have provided a framework within which intake performance parameters can be estimated. Moreover, We are now able to identified which configuration parameters are crucial for reliable performance intake testing and quantified the performance parameters uncertainty for relevant operating conditions.

7.1 Future work

Considering the three aspects mentioned above, some improvements could be envisaged. Future work would be to find a better test scenario providing more precise results. An alternative measurement of pumping speeds would be to inject an additional known mass flux. Then, the precision of the probes could be augmented through a calibration procedure, or by choosing more accurate devices. As further work, an optimization study of the geometrical configuration of the facility could be performed in order to further improve the measurement accuracy of $\tau_{1,fast}$.

Bibliography

- [1] N.H. Crisp et al. “The Benefits of Very Low Earth Orbit for Earth Observation Missions”. In: *Progress in Aerospace Sciences 117* (2020).
- [2] E. Ferrato V. Giannetti A. Piragino M. Andrenucci and T. Andreussi. “Development Roadmap of SITAEL’s RAM-EP System”. In: *International Electric Propulsion Conference* (2019).
- [3] G. A. Bird. *Molecular Gas Dynamics and the Direct Simulation of Gas Flows*. Clarendon Press, Oxford, 1994.
- [4] Bronkhorst. *Calibration Certificate*. 2012. URL: https://certificate.bronkhorst.com/calibration_certificate/index1.html.
- [5] Bronkhorst. *Digital Thermal Mass Flow Meters and Controllers for Gases*. 2021. URL: https://www.bronkhorst.com/getmedia/98668a82-8d1c-4b7f-af8e-995be25641b3/EL-FLOW-Select_en.pdf.
- [6] RS Components. *Platinum Resistance Thermometer (PRT) Selection Guide*. 2021. URL: <https://docs.rs-online.com/24d5/0900766b815e5304.pdf>.
- [7] Brown Walker Szabo Huang Foster. “Recommended Practice for Use of Faraday Probes in Electric Propulsion Testing”. In: *JOURNAL OF PROPULSION AND POWER* (2017). DOI: DOI:10.2514/1.B35696.
- [8] J. Gomez-Goni and P.J. Lobo. “Comparison between Monte Carlo and analytical calculation of the conductance of cylindrical and conical tubes”. In: *American Vacuum Society* (2003). DOI: DOI:10.1116/1.1568746.
- [9] C. Groll. *Development of a Plasma Diagnostic System*. Delft University of Technology, 2018.
- [10] G. Voss H. Rottländer W. Umrath. *Fundamentals of leak detection*. Cologne, Leybold GmbH, 2016.
- [11] T. E. Schwartzentruber I. D. Boyd. *Nonequilibrium Gas Dynamics and Molecular Simulation*. Cambridge university press, 2017.
- [12] JMS Southeast Incorporated. *General RTD Information*. 2021. URL: <https://www.jms-se.com>.
- [13] ISO. *Interprétation statistique de résultats d’essais — Estimation de la moyenne — Intervalle de confiance*. 2021. URL: <https://www.iso.org/fr/standard/7585.html>.
- [14] ISOTECH. *Reference Probes - Semi Standards Platinum Resistance Thermometers*. 2021. URL: <https://isotech.co.uk/wp-content/uploads/2020/09/NEW-Angled-Semi-Standards.pdf>.

- [15] Karl Jousten. *Handbook of vacuum Technology*. Berlin, Germany, 2016.
- [16] Dan Kernler. *Empirical Rule*. 2014. URL: <https://commons.wikimedia.org/w/index.php?curid=36506025%Ef%BB%BF>.
- [17] B. Giacomet L. Dobrowolski and N. Mendes. *NUMERICAL METHOD FOR CALCULATING VIEW FACTOR BETWEEN TWO SURFACES*. Pontifical University Catholic of the Paranas, 2007.
- [18] P. Parodi D. Le Quang F. Bariselli S. Boccelli Z. Alsalihi T. Magin. “STUDY OF A COLLECTOR-INTAKE SYSTEM FOR VLEO AIR-BREATHING PLATFORMS”. In: *von Karman Institute for Fluid Dynamics and Politecnico di Milano* (2019).
- [19] Peyman Memari Namin. “Perméation des gaz dans les polymères semi-cristallins par modélisation moléculaire”. In: *Université Paris-Sud 11* (2011).
- [20] N. BRAITHWAITE P. CHABERT. *PHYSICS OF RADIO-FREQUENCY PLASMAS*. Cambridge university press, 2011.
- [21] D. K. Robinson P. R. Bevington. *Data Reduction and Error Analysis*. McGraw-Hill Companies, 2003.
- [22] Pietro Parodi. *Analysis and Simulation of an Intake for Air-Breathing Electric Propulsion Systems*. Università di Pisa, Italy, 2018/2019.
- [23] O. Raisanen. *Electrostatic ion thruster*. 2012. URL: https://commons.wikimedia.org/wiki/File:Electrostatic_ion_thruster-en.svg.
- [24] S. Mazouffre T. Hallouin. “Far-Field Plume Characterization of a 100-W Class Hall Thruster”. In: *Aerospace* (2020). DOI: 10.3390/aerospace7050058.
- [25] ThrustMe. *LOW TEMPERATURE ARGON (LTA) Ion-Electron Source*. Verrieres-le-Buisson, France, 2019.
- [26] Pfeiffer Vacuum. *ATH 2303 M, DN 250 ISO-F, with external drive electronics, watercooled, non-heated*. Asslar, Germany, 2021.
- [27] Pfeiffer Vacuum. *ATH 3204 M, DN 320 ISO-F, watercooled, non-heated, with integrated drive electronics*. Asslar, Germany, 2021.
- [28] Pfeiffer Vacuum. *Introduction to high and ultra high vacuum production*. Asslar, Germany, 2021.
- [29] Pfeiffer Vacuum. *PKR 360, low current, DN 25 ISOKF*. Asslar, Germany, 2021.

Appendix A

Expression Analytic used for the slow flux transmissivities

Thanks to various tests, it is possible to determine the parameters not measured by a probe. It is the case of the slow flux transmission probabilities. They are computed thanks to different measurements: the pressures, the PFG flow, and the temperatures, and thanks to the values estimated during previous tests: leak rates and pumping speeds. Unlike all other tests, the model equations are not sufficient, and further simplification is required. If the temperatures of the two chambers are considered equal, then it is possible to use the model from the book [15].

If two vacuum chambers are linked by a succession of N components The model considers that the transmission probabilities of this connection respects

$$\frac{1}{A_{in}} \left(\frac{1}{\tau_{1N}} - 1 \right) = \sum_{k=1}^N \frac{1}{A_k} \left(\frac{1}{\tau_k} - 1 \right) + \sum_{k=1}^{N-1} \left(\frac{1}{\bar{A}_{k+1}} - \frac{1}{A_k} \right) \delta_{k,k+1} \quad (\text{A.1})$$

where k denotes the component number, A_{in} is the cross section of intake to the component series, A_k is the cross-section of component k , τ_{1N} is the total transmission probability of the connection, τ_k is the transmission probability for component k , and $\delta_{k,k+1}$ is a factor depending on the cross section dimensions. If the next component has a smaller cross-section ($A_{k+1} < A_k$), then $\delta_{k,k+1} = 1$. But if the next component has an equal or larger section ($A_{k+1} \geq A_k$), then $\delta_{k,k+1} = 0$. To apply this model, the system connecting the two chambers has three components. Starting from the main chamber, it is composed of a valve with the known section A_1 , the intake, and a duct of section A_2 . This latter is also known and lower than A_1 . Although the model also allows considering more complex geometry as the intake, the reasoning presented here only uses the average cross-section of each piece of equipment. As shown by the drawing A.1, there are three possible scenarios. Either the section of the intake \bar{A}_{intake} is greater than or equal to A_1 , or $A_1 > \bar{A}_{intake} \geq A_2$, or is strictly less than A_2 .

By considering Equation A.1, the two transmission probabilities of the slow flows

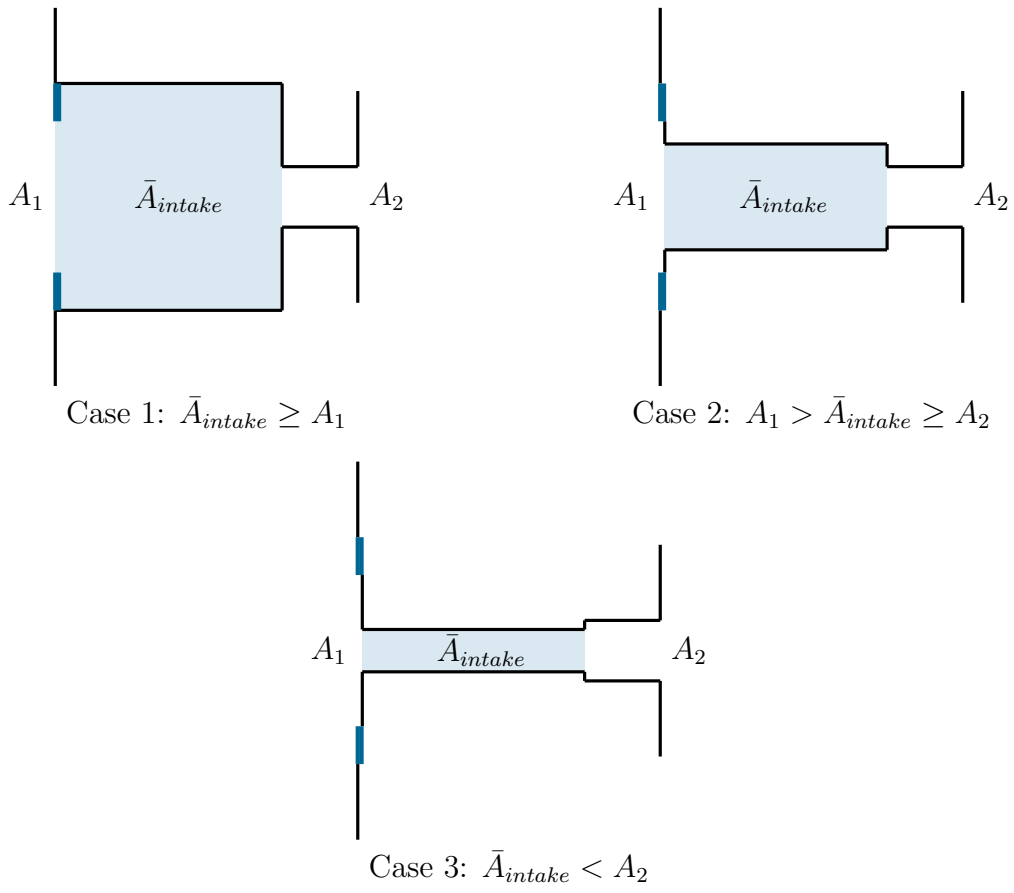


Figure A.1: Analytical model used to model the connection between both chambers

belong to the relations

$$\begin{aligned}
\frac{1}{A_1} \left(\frac{1}{\tau_{1,slow}} - 1 \right) &= \frac{1}{A_1} \left(\frac{1}{\tau_1} - 1 \right) + \frac{1}{\bar{A}_{intake}} \left(\frac{1}{\tau_{intake}} - 1 \right) + \frac{1}{A_2} \left(\frac{1}{\tau_2} - 1 \right) \\
&\quad + \left(\frac{1}{\bar{A}_{intake}} - \frac{1}{A_1} \right) \delta_{1,intake} + \left(\frac{1}{A_2} - \frac{1}{\bar{A}_{intake}} \right) \delta_{intake,2} \\
&= \frac{1}{A_1} \left(\frac{1}{\tau_1} - 1 - \delta_{1,intake} \right) + \frac{1}{\bar{A}_{intake}} \left(\frac{1}{\tau_{intake}} - 1 + \delta_{1,intake} - \delta_{intake,2} \right) \\
&\quad + \frac{1}{A_2} \left(\frac{1}{\tau_2} - 1 + \delta_{intake,2} \right), \tag{A.2}
\end{aligned}$$

$$\begin{aligned}
\frac{1}{A_2} \left(\frac{1}{\tau_{2,slow}} - 1 \right) &= \frac{1}{A_2} \left(\frac{1}{\tau_2} - 1 \right) + \frac{1}{\bar{A}_{intake}} \left(\frac{1}{\tau_{intake}} - 1 \right) + \frac{1}{A_1} \left(\frac{1}{\tau_1} - 1 \right) \\
&\quad + \left(\frac{1}{\bar{A}_{intake}} - \frac{1}{A_2} \right) \delta_{2,intake} + \left(\frac{1}{A_1} - \frac{1}{\bar{A}_{intake}} \right) \delta_{intake,1} \\
&= \frac{1}{A_2} \left(\frac{1}{\tau_2} - 1 - \delta_{2,intake} \right) + \frac{1}{\bar{A}_{intake}} \left(\frac{1}{\tau_{intake}} - 1 + \delta_{2,intake} - \delta_{intake,1} \right) \\
&\quad + \frac{1}{A_1} \left(\frac{1}{\tau_1} - 1 + \delta_{intake,1} \right), \tag{A.3}
\end{aligned}$$

where A_1 and A_2 are the cross section of the valve (in dark blue) and the duct linked to the second chamber, \bar{A}_{intake} is the intake mean section (in light blue), τ_1 , τ_{intake} , and τ_2 are the transmission probabilities of the valve, the intake and the duct respectively.

A.1 Case 1: $\bar{A}_{intake} \geq A_1$

In the first case, the section of the intake is larger than A_1 and A_2 . The terms depending on the geometry are

$$\delta_{1,intake} = 0 \quad \delta_{2,intake} = 0 \quad \delta_{intake,1} = 1 \quad \delta_{intake,2} = 1.$$

And the relation A.2 and A.3 become:

$$\begin{aligned}
\frac{1}{A_1} \left(\frac{1}{\tau_{1,slow}} - 1 \right) &= \frac{1}{A_1} \left(\frac{1}{\tau_1} - 1 - 0 \right) + \frac{1}{\bar{A}_{intake}} \left(\frac{1}{\tau_{intake}} - 1 + 0 - 1 \right) \\
&\quad + \frac{1}{A_2} \left(\frac{1}{\tau_2} - 1 + 1 \right) \\
&= \frac{1}{A_1} \left(\frac{1}{\tau_1} - 1 \right) + \frac{1}{\bar{A}_{intake}} \left(\frac{1}{\tau_{intake}} - 2 \right) + \frac{1}{A_2} \frac{1}{\tau_2}, \\
\frac{1}{A_2} \left(\frac{1}{\tau_{2,slow}} - 1 \right) &= \frac{1}{A_2} \left(\frac{1}{\tau_2} - 1 - 0 \right) + \frac{1}{\bar{A}_{intake}} \left(\frac{1}{\tau_{intake}} - 1 + 0 - 1 \right) \\
&\quad + \frac{1}{A_1} \left(\frac{1}{\tau_1} - 1 + 1 \right) \\
&= \frac{1}{A_2} \left(\frac{1}{\tau_2} - 1 \right) + \frac{1}{\bar{A}_{intake}} \left(\frac{1}{\tau_{intake}} - 2 \right) + \frac{1}{A_1} \frac{1}{\tau_1}.
\end{aligned}$$

By isolating the terms $\frac{1}{\bar{A}_{intake}} \left(\frac{1}{\tau_{intake}} - 2 \right)$, these two expression provide

$$\begin{aligned} \frac{1}{A_1} \left(\frac{1}{\tau_{1,slow}} - 1 \right) - \frac{1}{A_1} \left(\frac{1}{\tau_1} - 1 \right) - \frac{1}{A_2} \frac{1}{\tau_2} &= \frac{1}{A_2} \left(\frac{1}{\tau_{2,slow}} - 1 \right) - \frac{1}{A_2} \left(\frac{1}{\tau_2} - 1 \right) - \frac{1}{A_1} \frac{1}{\tau_1} \\ \frac{1}{A_1} \left(\frac{1}{\tau_{1,slow}} - 1 - \frac{1}{\tau_1} + 1 + \frac{1}{\tau_1} \right) &= \frac{1}{A_2} \left(\frac{1}{\tau_{2,slow}} - 1 - \frac{1}{\tau_2} + 1 + \frac{1}{\tau_2} \right) \\ \frac{1}{A_1} \frac{1}{\tau_{1,slow}} &= \frac{1}{A_2} \frac{1}{\tau_{2,slow}}. \end{aligned}$$

It yields to the relation

$$A_1 \tau_{1,slow} = A_2 \tau_{2,slow}. \quad (\text{A.4})$$

In reality this expression is general for any case. As the source does not provide a demonstration for the most general situation, the same reasoning for the other two cases is done in this annex.

A.2 Case 2: $A_1 > \bar{A}_{intake} \geq A_2$

For the second case, the factors take values

$$\delta_{1,intake} = 1 \quad \delta_{2,intake} = 0 \quad \delta_{intake,1} = 0 \quad \delta_{intake,2} = 1.$$

With these values, the equations A.2 and A.3 are

$$\begin{aligned} \frac{1}{A_1} \left(\frac{1}{\tau_{1,slow}} - 1 \right) &= \frac{1}{A_1} \left(\frac{1}{\tau_1} - 1 - 1 \right) + \frac{1}{\bar{A}_{intake}} \left(\frac{1}{\tau_{intake}} - 1 + 1 - 1 \right) \\ &\quad + \frac{1}{A_2} \left(\frac{1}{\tau_2} - 1 + 1 \right) \\ &= \frac{1}{A_1} \frac{1}{\tau_1} + \frac{1}{\bar{A}_{intake}} \left(\frac{1}{\tau_{intake}} - 1 \right) + \frac{1}{A_2} \frac{1}{\tau_2}, \\ \frac{1}{A_2} \left(\frac{1}{\tau_{2,slow}} - 1 \right) &= \frac{1}{A_2} \left(\frac{1}{\tau_2} - 1 - 0 \right) + \frac{1}{\bar{A}_{intake}} \left(\frac{1}{\tau_{intake}} - 1 + 0 - 0 \right) \\ &\quad + \frac{1}{A_1} \left(\frac{1}{\tau_1} - 1 + 0 \right) \\ &= \frac{1}{A_2} \left(\frac{1}{\tau_2} - 1 \right) + \frac{1}{\bar{A}_{intake}} \left(\frac{1}{\tau_{intake}} - 1 \right) + \frac{1}{A_1} \left(\frac{1}{\tau_1} - 1 \right). \end{aligned}$$

Again, the terms $\frac{1}{\bar{A}_{intake}} \left(\frac{1}{\tau_{intake}} - 1 \right)$ can be isolated from the rest in both formulas. They can be combined to obtain

$$\begin{aligned} \frac{1}{A_1} \left(\frac{1}{\tau_{1,slow}} - 1 \right) - \frac{1}{A_1} \frac{1}{\tau_1} - \frac{1}{A_2} \frac{1}{\tau_2} &= \frac{1}{A_2} \left(\frac{1}{\tau_{2,slow}} - 1 \right) - \frac{1}{A_2} \left(\frac{1}{\tau_2} - 1 \right) - \frac{1}{A_1} \left(\frac{1}{\tau_1} - 1 \right) \\ \frac{1}{A_1} \left(\frac{1}{\tau_{1,slow}} - 1 - \frac{1}{\tau_1} + \frac{1}{\tau_1} - 1 \right) &= \frac{1}{A_2} \left(\frac{1}{\tau_{2,slow}} - 1 - \frac{1}{\tau_2} + 1 + \frac{1}{\tau_2} \right) \\ \frac{1}{A_1} \frac{1}{\tau_{1,slow}} &= \frac{1}{A_2} \frac{1}{\tau_{2,slow}}. \end{aligned}$$

This case, like the previous one, leads to the same final relation

$$A_1 \tau_{1,slow} = A_2 \tau_{2,slow}.$$

A.3 Case 3: $\bar{A}_{intake} < A_2$

Finally when the intake cross-section \bar{A}_{intake} is lower than A_2 and A_1 . The δ coefficients become

$$\delta_{1,intake} = 1 \quad \delta_{2,intake} = 1 \quad \delta_{intake,1} = 0 \quad \delta_{intake,2} = 0.$$

And the transmission probabilities respect the relation

$$\begin{aligned} \frac{1}{A_1} \left(\frac{1}{\tau_{1,slow}} - 1 \right) &= \frac{1}{A_1} \left(\frac{1}{\tau_1} - 1 - 1 \right) + \frac{1}{\bar{A}_{intake}} \left(\frac{1}{\tau_{intake}} - 1 + 1 - 0 \right) \\ &\quad + \frac{1}{A_2} \left(\frac{1}{\tau_2} - 1 + 0 \right) \\ &= \frac{1}{A_1} \left(\frac{1}{\tau_1} - 2 \right) + \frac{1}{\bar{A}_{intake}} \frac{1}{\tau_{intake}} + \frac{1}{A_2} \left(\frac{1}{\tau_2} - 1 \right), \end{aligned}$$

$$\begin{aligned} \frac{1}{A_2} \left(\frac{1}{\tau_{2,slow}} - 1 \right) &= \frac{1}{A_2} \left(\frac{1}{\tau_2} - 1 - 1 \right) + \frac{1}{\bar{A}_{intake}} \left(\frac{1}{\tau_{intake}} - 1 + 1 - 0 \right) + \frac{1}{A_1} \left(\frac{1}{\tau_1} - 1 + 0 \right) \\ &= \frac{1}{A_2} \left(\frac{1}{\tau_2} - 2 \right) + \frac{1}{\bar{A}_{intake}} \frac{1}{\tau_{intake}} + \frac{1}{A_1} \left(\frac{1}{\tau_1} - 1 \right). \end{aligned}$$

As previously the terms $\frac{1}{\bar{A}_{intake}} \frac{1}{\tau_{intake}}$ are separated from the rest these equations can be assembled to give

$$\begin{aligned} \frac{1}{A_1} \left(\frac{1}{\tau_{1,slow}} + 1 - \frac{1}{\tau_1} \right) - \frac{1}{A_2} \left(\frac{1}{\tau_2} - 1 \right) &= \frac{1}{A_2} \left(\frac{1}{\tau_{2,slow}} + 1 - \frac{1}{\tau_2} \right) - \frac{1}{A_1} \left(\frac{1}{\tau_1} - 1 \right) \\ \frac{1}{A_1} \left(\frac{1}{\tau_{1,slow}} - 1 - \frac{1}{\tau_1} + 2 + \frac{1}{\tau_1} - 1 \right) &= \frac{1}{A_2} \left(\frac{1}{\tau_{2,slow}} - 1 - \frac{1}{\tau_2} + 2 + \frac{1}{\tau_2} - 1 \right) \\ \frac{1}{A_1} \frac{1}{\tau_{1,slow}} &= \frac{1}{A_2} \frac{1}{\tau_{2,slow}} \\ A_1 \tau_{1,slow} &= A_2 \tau_{2,slow}. \end{aligned}$$

In this case also the same relation is obtained. This confirms that it remains valid for the installation, independent of the intake dimension.

Appendix B

Partial derivatives of the Error Propagation Analysis

B.1 Slow flux transmission probabilities

This appendix lists all the partial derivatives used for the two transmission probability uncertainties of $\tau_{1,slow}$.

B.1.1 First hypothesis

In the case of the first hypothesis, $\tau_{1,slow}$ is given by

$$\tau_{1,slow} = \sqrt{\frac{2\pi m}{kT_{c1}}} \frac{S_2 P_{c2} - Q_{2,leak}}{P_{c1} 1000 A_1}.$$

And the corresponding partial derivatives are

$$\begin{aligned} \frac{\partial \tau_{1,slow}}{\partial T_{c1}} &= -\sqrt{\frac{2\pi m}{kT_{c1}^3}} \frac{S_2 P_{c2} - Q_{2,leak}}{P_{c1} 2000 A_1} \\ \frac{\partial \tau_{1,slow}}{\partial S_2} &= \sqrt{\frac{2\pi m}{kT_{c1}}} \frac{P_{c2}}{P_{c1} 1000 A_1} \\ \frac{\partial \tau_{1,slow}}{\partial P_{c2}} &= \sqrt{\frac{2\pi m}{kT_{c1}}} \frac{S_2}{P_{c1} 1000 A_1} \\ \frac{\partial \tau_{1,slow}}{\partial Q_{2,leak}} &= \sqrt{\frac{2\pi m}{kT_{c1}}} \frac{-1}{P_{c1} 1000 A_1} \\ \frac{\partial \tau_{1,slow}}{\partial P_{c1}} &= -\sqrt{\frac{2\pi m}{kT_{c1}}} \frac{S_2 P_{c2} - Q_{2,leak}}{P_{c1}^2 1000 A_1} \end{aligned}$$

B.1.2 Second hypothesis hypothesis

The second hypothesis yields to the expression

$$\tau_{1,slow} = \frac{\sqrt{2\pi m}}{1000 A_1 \sqrt{k}} \left(\frac{S_2 P_{c2} - Q_{2,leak}}{P_{c1} \sqrt{T_{c1}} - P_{c2} \sqrt{T_{c2}}} \right),$$

with the partial derivatives

$$\begin{aligned}
 \frac{\partial \tau_{1,slow}}{\partial T_{c1}} &= \frac{\sqrt{2\pi m}}{1000A_1\sqrt{k}} \left(\frac{-P_{c1}(S_2P_{c2} - Q_{2,leak})}{2\sqrt{T_{c1}}(P_{c1}\sqrt{T_{c1}} - P_{c2}\sqrt{T_{c2}})^2} \right) \\
 \frac{\partial \tau_{1,slow}}{\partial S_2} &= \frac{\sqrt{2\pi m}}{1000A_1\sqrt{k}} \left(\frac{P_{c2}}{P_{c1}\sqrt{T_{c1}} - P_{c2}\sqrt{T_{c2}}} \right) \\
 \frac{\partial \tau_{1,slow}}{\partial P_{c2}} &= \frac{\sqrt{2\pi m}}{1000A_1\sqrt{k}} \left(\frac{S_2(P_{c1}\sqrt{T_{c1}} - P_{c2}\sqrt{T_{c2}}) + (S_2P_{c2} - Q_{2,leak})\sqrt{T_{c2}}}{(P_{c1}\sqrt{T_{c1}} - P_{c2}\sqrt{T_{c2}})^2} \right) \\
 \frac{\partial \tau_{1,slow}}{\partial Q_{2,leak}} &= \frac{\sqrt{2\pi m}}{1000A_1\sqrt{k}} \left(\frac{-1}{P_{c1}\sqrt{T_{c1}} - P_{c2}\sqrt{T_{c2}}} \right) \\
 \frac{\partial \tau_{1,slow}}{\partial P_{c1}} &= \frac{\sqrt{2\pi m}}{1000A_1\sqrt{k}} \left(\frac{-\sqrt{T_{c1}}(S_2P_{c2} - Q_{2,leak})}{(P_{c1}\sqrt{T_{c1}} - P_{c2}\sqrt{T_{c2}})^2} \right) \\
 \frac{\partial \tau_{1,slow}}{\partial T_{c2}} &= \frac{\sqrt{2\pi m}}{1000A_1\sqrt{k}} \left(\frac{P_{c2}(S_2P_{c2} - Q_{2,leak})}{2\sqrt{T_{c2}}(P_{c1}\sqrt{T_{c1}} - P_{c2}\sqrt{T_{c2}})^2} \right)
 \end{aligned}$$

B.2 Fast flux transmission probability

The expression of the probability $\tau_{1,fast}$ is

$$\tau_{1,fast} = \frac{1}{Q_{1,fast}} \left(P_{c2}1000A_2\tau_{2,slow}\sqrt{\frac{kT_{c2}}{2\pi m}} + S_2P_{c2} - P_{c1}1000A_1\tau_{1,slow}\sqrt{\frac{kT_{c1}}{2\pi m}} - Q_{2,leak} \right).$$

The partial derivative of this expression are

$$\begin{aligned}
 \frac{\partial \tau_{1,fast}}{\partial Q_{1,fast}} &= \frac{-1}{Q_{1,fast}^2} \left(P_{c2} 1000 A_2 \tau_{2,slow} \sqrt{\frac{k T_{c2}}{2\pi m}} + S_2 P_{c2} - P_{c1} 1000 A_1 \tau_{1,slow} \sqrt{\frac{k T_{c1}}{2\pi m}} - Q_{2,leak} \right) \\
 \frac{\partial \tau_{1,fast}}{\partial P_{c2}} &= \frac{1}{Q_{1,fast}} \left(1000 A_2 \tau_{2,slow} \sqrt{\frac{k T_{c2}}{2\pi m}} + S_2 \right) \\
 \frac{\partial \tau_{1,fast}}{\partial \tau_{2,slow}} &= \frac{1}{Q_{1,fast}} \left(P_{c2} 1000 A_2 \sqrt{\frac{k T_{c2}}{2\pi m}} \right) \\
 \frac{\partial \tau_{1,fast}}{\partial T_{c2}} &= \frac{1}{2 Q_{1,fast}} \left(P_{c2} 1000 A_2 \tau_{2,slow} \sqrt{\frac{k}{2\pi m T_{c2}}} \right) \\
 \frac{\partial \tau_{1,fast}}{\partial S_2} &= \frac{P_{c2}}{Q_{1,fast}} \\
 \frac{\partial \tau_{1,fast}}{\partial P_{c1}} &= \frac{-1}{Q_{1,fast}} \left(1000 A_1 \tau_{1,slow} \sqrt{\frac{k T_{c1}}{2\pi m}} \right) \\
 \frac{\partial \tau_{1,fast}}{\partial \tau_{1,slow}} &= \frac{-1}{Q_{1,fast}} \left(P_{c1} 1000 A_1 \sqrt{\frac{k T_{c1}}{2\pi m}} \right) \\
 \frac{\partial \tau_{1,fast}}{\partial T_{c1}} &= \frac{-1}{2 Q_{1,fast}} \left(P_{c1} 1000 A_1 \tau_{1,slow} \sqrt{\frac{k}{2\pi m T_{c1}}} \right) \\
 \frac{\partial \tau_{1,fast}}{\partial Q_{2,leak}} &= \frac{-1}{Q_{1,fast}}
 \end{aligned}$$